Azerbaijan Journal of Physics

Fizika

www.physics.gov.az

Azerbaijan Journal of Physics

Fizika

PHOTOLUMINESCENCE OF POROUS SILICON
WITH LIQUID CRYSTALLINE FILLERS

T.D.IBRAGIMOV, O.B.TAGIYEV, S.A.ABUSHEV, E.A.ALLAHVERDIYEV
G.M.Abdullayev Institute of Physics of Azerbaijan National Academy of Sciences
AZ1143 H.Javid Avenue, 33, Baku, Azerbaijan

G.M.BAYRAMOV, N.H.DARVISHOV
Baku State University
AZ1148 Z.Khalilov street, 23, Baku, Azerbaijan

Luminescence spectra of both pure porous silicon and filled with liquid crystals 5CB and HI09 which emit radiation in violet spectral region are investigated. It is shown that there are bands of both porous silicon and a liquid crystal in the at luminescence spectrum of porous silicon with liquid crystal filler. Thus the intensity of the band corresponding to porous silicon increases several times in comparison with a luminescence of pure porous silicon without filler. Experimental results are explained by internal no radiating swapping of energy from a liquid crystal to porous silicon.

INTRODUCTION

The discovery of visible luminescence from porous silicon [1] has stimulated a large interest in this material. Numerous studies have demonstrated that it is possible to achieve efficient visible luminescence from porous silicon layers [2]. This material system has significant economic potential as efficient visible emitters could be fabricated on silicon wafers and incorporated with current microelectronic devices using existing silicon processing technologies.

Modeling conceptions about the mechanism of pore formation have started to be formed with the middle of 1960, but the uniform point of view has not developed. Generalizing various models, it is possible to note the following. The silicon surface at contact with water solutions of HF is sated with hydrogen and becomes chemically inert in relation to electrolyte. If potential difference supplies on electrodes, holes in silicon start to migrate to an interface silicon-electrolyte. Thus atoms of silicon are released from hydrogen blocking them, start to co-operate with ions and molecules of electrolyte and pass in a solution. If electrolysis is carried out at high density of a current then a considerable quantity of holes arrives to an electrode surface. They are in motion with continuous front to intersection and provide reactionary ability practically to each silicon atom. As micro ledges have larger surface than plain areas, they are dissolved faster. Thus, the surface of the silicon anode is gradually leveled. It also is a regime of electrochemical polishing. If electrolysis is carried out at low density of a current, the quantity of holes does not suffice for organization of continuous front and consequently there is a local dissolution of silicon surface. Pore nucleation can begin on microdeepenings, structural defects, mechanically strained areas or local indignations of a potential field of a surface. Eventually, the appeared pores continue the growth in depth of an electrode at the expense of drift of holes to pore tips, where intensity of electric field over.

It is obvious, that quantity of holes is different and consequently processes of pore formation have the features in silicon n - and p-types. Holes are the basic charge carriers and their concentration equal to 10^{14}-10^{18} cm^{-3} for p-Si. In this case, as a rule, pores with nanometer sizes are formed. Changing anodizing conditions, porous silicon with various morphology may be obtained a current density of anodizing, time, additional illumination, electrolyte structure, level and type of doping influence on the pore cross-section size R. Porous silicon is classified by the pore size on microporous (R <2 nm), mesoporous (2 nm <R <50 nm) and macroporous (R> 50 nm). Key parameter of a porous material is the porosity factor. It defines a part of volume of a material occupied by pores. Value of porosity changes between 5 and 95 % for porous silicon.

The shift of the bandgap into the visible is due to quantum confinement for porous silicon. The quantum structure also results in the formation of a pseudo-direct gap increasing the efficiency of the radiative recombination by over 10^4 from bulk silicon which has an indirect bandgap [3]. One of methods of improvement of operated properties of porous silicon is inclusion various materials in pores. Time-resolved photoluminescence from porous silicon coated with a diamond like carbon film is investigated [4]. The intensity of the photoluminescence from the carbon film is observed to increase after deposition, and there is an accompanying change in the intensity and a short-wavelength shift of the photoluminescence band of porous silicon that depends on the porosity of its original layers. These changes are explained by the formation of carbon nanoclusters on the surface of the silicon filaments. The influence of rapid thermal annealing on the photoluminescence properties of porous- silicon/diamond like-carbon-film structures is investigated in [5]. Redistribution of the radiation from the long-wavelength to the short-wavelength region is discovered. Models of the processes observed are presented. The photoluminescence of porous silicon with and without carbon deposition fabricated by plasma-enhanced chemical vapor deposition technique has been investigated in [6]. It was found that after the carbon deposition a new intense blue emission appeared, which changes with dependence from thermal treatment. Finally,

the mechanism for the effect of carbon deposition and rapid thermal processes on photoluminescence properties of porous silicon was discussed [7]. Photoluminescence of erbium-implanted porous silicon is investigated [8]. Room temperature 1.54 mm Er luminescence is observed after annealing. The luminescence spectrum, annealing luminescence is mediated by photocarriers in the amorphous silicon matrix in porous silicon, and not related to the presence of the crystal nanograins.

The fluorescence of the nematic liquid crystal n-butyl-n'-methoxyazoxybenzene (BMAOB) in the form of a layer and in porous glasses with pores of different diameter is investigated [8].The spectra of BMAOB in a layer and in small- diameter pores differ significantly from each other. A band peaked at 475 nm is observed in the stationary spectrum of a fluorescence BMAOB layer, whereas the spectrum of BMAOB in pores smaller than 4 nm in diameter contains a band peaked at 550 nm. When the pore diameter decreases to 1 nm, the band at 475 nm is almost completely suppressed and only the band at 550 nm manifests itself. Tunable emission in the near infrared is demonstrated in the work [9]. The building blocks for tunable light sources consist of porous silicon microcavities infiltrated with erbium doped nematic liquid crystals. Erbium ions are luminescence source, porous silicon microcavities narrow the emission band and LCs enable tuning of the peak wavelength.

In this work the influence of fluorescent liquid crystal included into pores of porous silicon on its photoluminescence (FL) is studied.
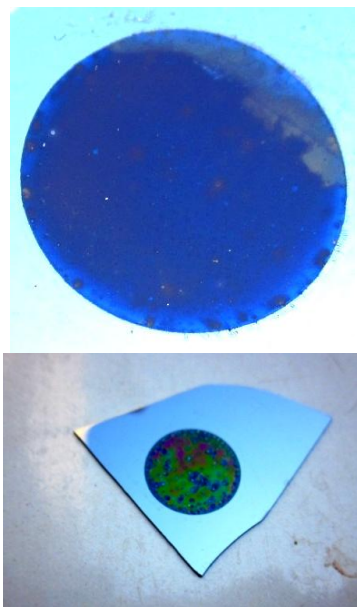
EXPERIMENTAL

Fig.1. The image of the silicon sample with a porous layer.

Samples of porous silicon have been obtained by a method of anode electrochemical etching in galvanostatic mode in a vertical cell on the monocrystal silicon substrate polished from both sides p-Si with orientation (111), specific resistance of 10 Ohm · cm alloyed by boron and having a thickness of 380 μm. A layer of an aluminum film was put by thermal evaporation on the

back side of silicon plate with the subsequent intrusion it at temperature 450°C within 40 minutes for carrying out of electrochemical anodization. The area of layers made about 1 cm^2. The wire from alloy Pt-Rh served as a counterelectrode, removed from a substrate on 4 cm. The electrolyte on the basis of the fluoric acid diluted in isopropyl alcohol has been chosen as an etching. Etching time was 1-30 minutes, and anodization current density was 20 μA/cm^2. The layer of microporous silicon is formed on the surface at small times of etching (1-3 minutes). Increasing an etching time both its thickness and its porosity grow. Macroporous silicon starts to arise chaotically under a layer of microporous silicon at some thickness. Upper layer of microporous silicon strongly bursts usually at drying of such samples because of high porosity. At large times of etching the part of microporous silicon exfoliates also macroporous silicon is visible at the pure state. At the further increase in etching time the thickness of macroporous silicon increases. The layer of porous silicon differs from the basic substrate iridescent coloring (Fig. 1).

The liquid crystal 5CB with temperature interval of nematic phase 22.5 -35.5 °C was used as filler. Moreover, the liquid crystalline mixture H109 was also used. It has temperature interval of nematic phase 5 -56 °C and following components: 4-n-butyl benzoic acid- 4-n-hexyloxyphenyl ester (**H-21**)

$$C_4H_9 - \langle O \rangle - COO - \langle O \rangle - OC_6H_{13}$$

4-n-pentanoyloxy-benzoic acid-4-n-hexyloxyphenyl ester (**H-22**)

$$C_4H_9O\text{-}COO - \langle O \rangle \text{-} COO - \langle O \rangle - OC_6H_{13}$$

4-n-hexyloxy-benzoic acid-4-n-butylphenyl ester (**H-44)**

$$C_6H_{13}O\text{-}\langle O \rangle\text{-}COO - \langle O \rangle - C_4H_9$$

4-n- methoxy-benzoic acid-4-n-pentylphenyl ester (**H-86)**

$$CH_3O\text{-}\langle O \rangle - COO - \langle O \rangle - C_5H_{11}$$

For excitation and registration of luminescent spectra, following experimental set ups are used. One of them is based on luminescent excitation by the nitric laser, and the set up block is shown in a Fig. 2. The luminescence is excited by xenon lamp in another set up (Fig. 3).
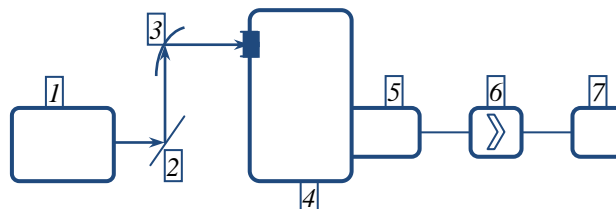

Fig.2. The block - scheme of set up for registration of photoluminescence spectra at excitation by laser radiation. 1 - the nitric laser, 2 - the holder with the sample, 3 - a parabolic mirror, 4 - double monochromator SDL - 1, 5 - the block of photoelectronic multipliers, 6 - the block of the amplifier with the synchronous detector, 7 - recording potentiometer KSP - 4.

The nitric laser is pulsed with generation wavelength of 337.1 nm, with duration of an impulse of 8 nanoseconds, frequency of impulse sequence - 1000 Hz, average capacity - 270 mWt. The photo multipliers FEU - 39A and FEU . – 62 are used as a detector
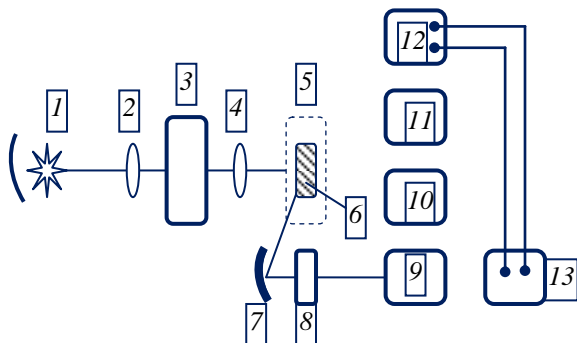

Fig.3. The diagram of set-up for registration of luminescence spectra at excitation by a xenon lamp: 1 -light source (xenon lamp), a 2-quartz lens, 3 – monochromator SPM-2, 4- quartz lens, 5-kriostat, 6 - the sample, 7 - a spherical mirror, 8 - the modulator, 9 – monochromator IKS-12, 10 - photo multiplier FEU - 79, 11 - amplifier U2-6, 12 - the synchronous detector K3-2, two-co-ordinate recorder ENDIM – 620.

RESULTS AND DISCUSSION

The FL spectra of porous silicon samples are presented in Fig.4. These samples are typical ones obtained different technological groups. From Fig.4, one can see that FL is practically absent in the short –wave region. The FL in this region mainly corresponds to SiO_x layers formed on the pores walls due to oxidation. The weak FL in the short-wave region determined mainly by the oxidized surface layers suggests that SiO_x layers are very thin, and so Si probes are poorly oxidized.

In the long-wave spectral region, one can see a wide structureless band for each sample. The spectral position and intensity of this band is determined by the sample morphology. For samples 1 and 2, the maxima of the band are 582 nm and 661nm. Measuring FL of samples from the same party, one can see that the band maximum changes only within 578-585 nm and 650-665 nm, correspondently. Such a character of the FL of porous Si is due to quantum dimensional effects in Si nano-crystallites of a variable profile. The smaller diameter of Si crystallites formed in the etching process, the shorter is the spectral maximum of the FL band.

The FL spectra of samples from the party 1 without a filler (a), only liquid crystals 5CB and H109 (b), and at inclusion of liquid crystals into pores of porous silicon are shown in Fig. 5 and Fig. 6. Apparently, inclusion of a liquid crystal into silicon enhances the FL intensity of porous silicon. Thus the FL maximum of the band of porous silicon is slightly displaced to long waves, and the intensity of the band corresponding to a liquid crystal easily decreases. Similar results are observed for samples of porous silicon from party 2 (Fig. 7 and Fig. 8). But in this case, the effect of increase in band intensity of porous silicon is less accurate.

It is well-known that the major energy carriers in porous silicon are excitons, whose properties depend on the state of pore walls, because of the small diameters of Si threads.
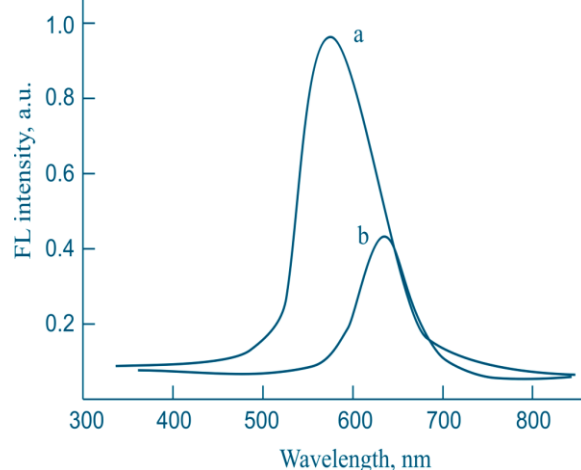

Fig.4. Luminescent spectra of porous silicon samples from different parties: 1(a) и 2 (b).

Fig.5. Luminescent spectra: a- porous silicon sample from party 1 without a filler, b- liquid crystal 5CB, c-porous silicon with the 5CB filler.

Fig.6. Luminescent spectra: a- porous silicon sample from party 1 without a filler, b- liquid crystal H109, porous silicon with the H109 filler.
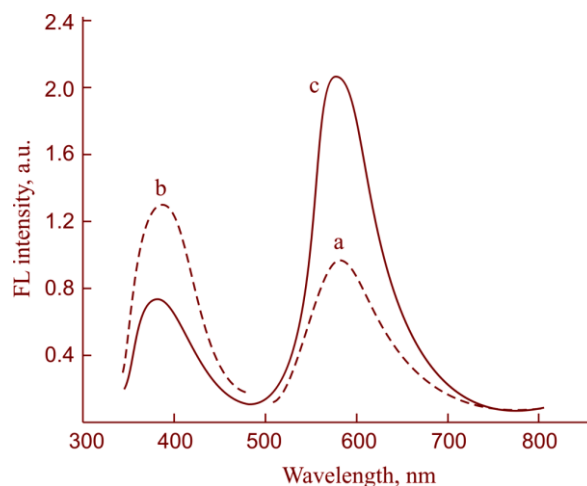
Fig.7. Luminescent spectra: a- porous silicon sample from party 2 without a filler, b- liquid crystal 5CB, porous silicon with the 5CB filler.
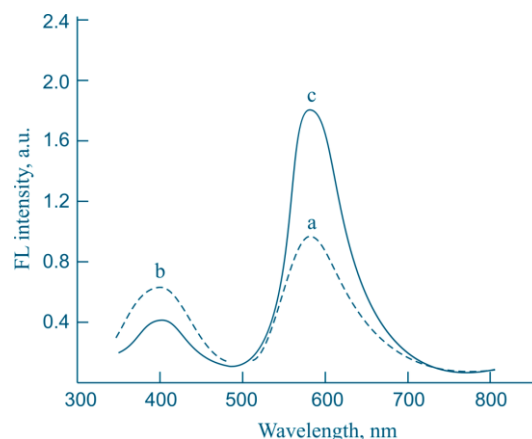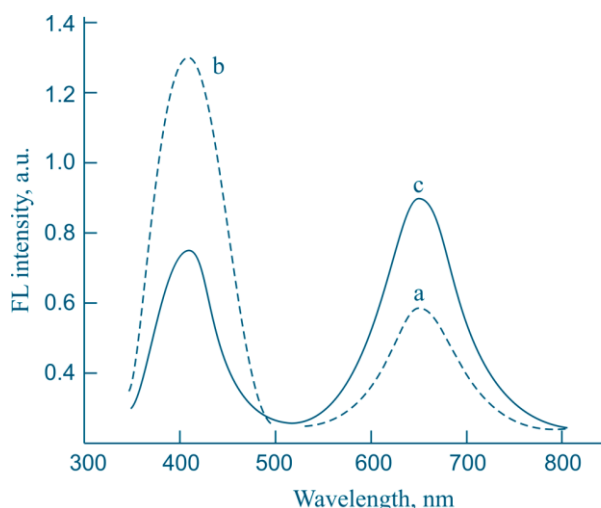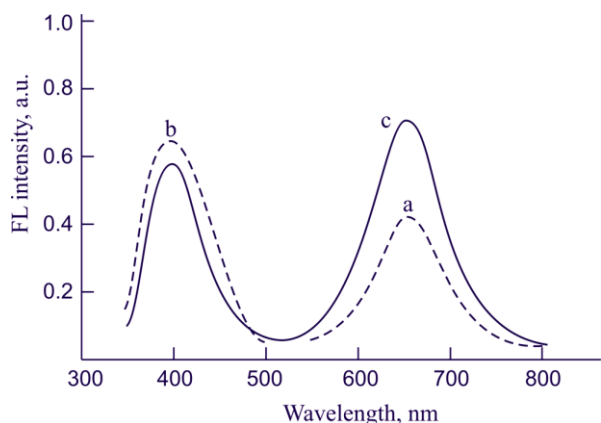

Fig.8. Luminescent spectra: a- porous silicon sample from party 2 without a filler, b- liquid crystal H109, porous silicon with the H109 filler.

Energy transfer from a liquid crystal to porous silicon can be radiating or nonradiating. To model of radiating process, the pure porous silicon and porous silicon with LC filler was pumped with radiation of xenon lamp passed through monochromator. Thus the wavelength of an exciting line changes over a wide range. The FL intensity (maximum height) of the band for samples of porous silicon from different parties is shown at filling with liquid crystals. Apparently, the intensity of porous silicon decreases at approach of wavelength of an exciting line to the FL band of a liquid crystal (Fig.9). It specifies, basically, on nonradiating character of the transfer channel from a liquid crystal to porous silicon.
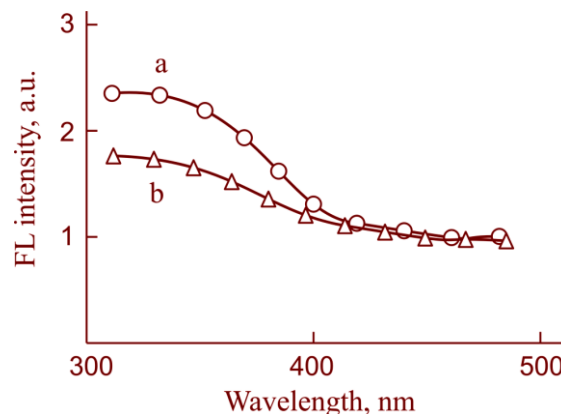

Fig.9. The intensity of luminescent band from the sample of porous silicon from party 1 with the liquid crystal filler versus wavelength of excitation: a- filler 5CB, b- filler H109.

The properties of excitons near the surface of a semiconductor are strongly influenced by the environment. In the case where the permittivity of the environment is much higher than that of a semiconductor, the binding energy of excitons is small, and excitons dissociate without luminescence. In the opposite case, when the permittivity of a semiconductor is considerably higher that of the environment, a rise of exciton energy is possible. These reasons influence on the luminescent intensity of porous silicon.

CONCLUSION

Luminescence spectra of both pure porous silicon and filled with liquid crystals 5CB and HI09 which emit radiation in violet spectral region are investigated. It is shown that there are bands of both porous silicon and a liquid crystal in the at luminescence spectrum of porous silicon with liquid crystal filler. Thus the intensity of the band corresponding to porous silicon increases several times in comparison with a luminescence of pure porous silicon without filler. Experimental results are explained by internal no radiating swapping of energy from a liquid crystal to porous silicon.

―――――――――――――――――

[1]   *L.T.Canham.* "Silicon quantum wire array fabrication by electrochemical and chemical dissolution of wafers." Appl. Phys.Lett., **57** (1990) 1046 - 1048. For a recent review of the work in porous silicon see: Thin Solid Films, 1995, **225** and "Porous Silicon", edited by Z. Chuan and R Tsu, World Scientific, Singapore, 1995.

[2]   *K.J.Nash, P.D.J.Calcott, L.T.Canham, M.J.Kane and D.Brumhead.* "The origin of efficient luminescence in highly porous silicon." J. Luminescence, **60/61** (1994) 297 - 301.

[3]   *F. Buda, J. Kohanoff and M. Parrinello.* "Optical properties of porous silicon : A first principles study." Phys. Rev. Lett., **69** (1992)1272 - 1275.

[4]   *Yu.P.Piryatinskii, V.A.Semenovich.* Distinescence features of time-resolved photoluminescence of porous silicon coated with a layer of diamondlike carbon. Technical Physics. **43**, No 4 (1998) 423.

[5]   *N.I.Kluyi, A.G.Rozhin, Yu.P.Piryatinskii, V.A.Semenovich.* Photoluminescence of porous-silicon/diamondlike – carbon - film structures subjected to rapid thermal annealing. Technical Physics Letters. **25**, No 4 (1999) 304.

[6]   *Jung H. Shin, G. N. van den Hoven, and A. Polman.* Origin of the 1.54 mm luminescence of erbium-implanted porous silicon. Appl. Phys. Lett. **66** (1995) 18.

[7]   *Yu.P.Piryatinskii, O.V.Yaroshchuk, L.A.Dolgov, T.V.Bindna,D. Enke.* Photoluminescence of liquid-crystal azo derivatives in nanopores. Optics and Spectroscopy, **97**, No. 4 (2004) 537-542.

[8]   *S.M. Weiss, J. Zhang, P.M. Fauchet, V.V. Seregin, J.L. Coffer.* Tunable silicon-based light sources using erbium doped liquid crystals. Applied Physics Letters, **90** (2007) 031112-1-03112-3.

RESONANT MAGNETOPOLARONS IN SEMICONDUCTOR NANOTUBE

S. M. SEYID-RZAYEVA

Institute of Physics, National Academy of Sciences of Azerbaijan,
AZ 1143 Baku, Azerbaijan
E -mail: s-nisa@rambler.ru

We present the results of the theoretical study of the magnetopolaron effect for nanotubes (NTs) of the finite length. It was established the possibility of the resonant coupling between the discrete energy levels of the electrons with the different numbers of the size quantization, which correspond to the movement of electrons around the circumference of NT in a longitudinal magnetic field. As an interaction that creates a resonant electron-phonon coupling are used the interaction of the electrons with the bulk longitudinal optical (LO) phonons. By using the perturbation theory for degenerate states, we calculated the energy of usual double and triple magnetopolarons. Numerical calculations of the energy splitting of the double magnetopolaron depending on the length and diameter of the NT were fulfilled for GaAs. It was found that the energy splitting is inversely to the square root of the NT length and decreases slightly with increasing diameter of the NT.

1. INTRODUCTION

The formation of the polaron states in a magnetic field was first discovered by Johnson and Larsen in a bulk semiconductor InSb under the study of the interband magneto-optical absorption of light[1]. The observed effect is also called magnetopolaron resonance and the resonance states formed by the electron excitations - magnetopolaron.

Resonant interaction of electrons with LO-phonons is of particular interest because it allows us directly determine the Frohlich coupling constant by means of magnetooptical experiments. Polaron states also play an important role in generating of the frequency dependence of magneto-optical effects [1].

In the past 20 years, intensive research of the magnetopolaron effect due to the emergence of new low-dimensional semiconductor structures in which the effect is amplified because of the size quantization of the electron spectrum [2]. The theory of magnetopolaron effect in quasi-two-dimensional semiconductor quantum well was developed in a number of theoretical studies [3-7]. A similar problem was studied in the disk-shaped quantum dot [8]. Magnetopolaron state is theoretically investigated for the elliptic quantum dot InAs / GaAs in [9]. There are also a number of papers devoted to theoretical and experimental investigation magnetopolaron effect in the two-dimensional systems [10-13].

Currently one of the most promising low-dimensional systems are cylindrical NTs. To our knowledge in such systems magnetopolaron effect were not theoretically investigated. It is interesting to consider this problem for a two-dimensional (2D) electron gas at the NT surface, which can be regarded as the plane rolled into a tube.

Usually, the resonance conditions in the quasi 2D systems are created by applying a magnetic field perpendicular to the plane of the two-dimensional electron gas [7], which leads to the discrete energy levels. The distance between these levels may be close to the energy of LO-phonon. Such a situation would create the conditions for resonant polaron interaction between the corresponding energy levels. The resonance condition for certain values of the magnetic field leads to the intersection of discrete energy levels. The electron-phonon interaction at the intersection points of energy levels leads to removing degeneracy.

The aim of this work is to determine the energies of the usual double and triple magnetopolaron, which are formed at the intersection of two or three discrete energy levels with common quantum numbers of the size quantization along axes of the NT, respectively. By analogy with the definition of [7] we call the usual magnetopolaron that arises from the intersection of energy levels with different magnetic quantum numbers, but with the same quantum numbers of size-quantization.

We investigate the magnetopolaron effect arising from the interaction the bulk LO- phonons with 2D electron gas located on the cylindrical surface of the semiconductor NT of finite length, in an uniform magnetic field directed along the axis of the NT.

2. THE MODEL AND BASIC RELATIONS

The energy spectrum of the electrons located on the surface of NT in the magnetic field B, directed along its axis, is considered in [14]. In paper [15] was added constraint on the electron motion along the axis of the NT. As the confining potential in the direction of the z-axis was used a parabolic potential of the form $(m_e \Omega^2 z^2)/2$, which allows to obtain analytical expressions for the spectrum and wave functions of the electron. It was assumed that the electrons do not interact with each other.

The expressions for the spectrum and wave functions of electrons on the surface of the NT are:

$$\psi_{m,n}(z,\varphi) = \frac{1}{\sqrt{2\pi}} e^{im\varphi} \chi_n(z). \quad (2)$$

Here $\chi_n(z)$ is defined by expression:

$$\chi(z) = \left(\frac{1}{2^n n! R_z \sqrt{\pi}}\right)^{1/2} e^{-\left(\frac{z}{R_z\sqrt{2}}\right)^2} H_n\left(\frac{z}{R_z}\right), \quad (3)$$

where m_e – effective mass of an electron, r_0 – radius of NT, $R = \sqrt{\hbar/(m_e \omega_c)}$ - magnetic length, $\omega_c = eB/(m_e c)$ - cyclotron frequency, m and n – quantum numbers, characterize the size quantization along the circumference and length of NT, with values $m = 0, \pm 1, \pm 2, \pm 3, \ldots$; $n = 0, 1, 2, \ldots$, respectively; $\chi_n(z)$ - eigenfunction of a one-dimensional oscillator, $R_z = \sqrt{\hbar/(m_e \Omega)}$ - oscillator length, Ω - oscillator frequency, $H_n(x)$ – Hermitian polynomial.

Taking into account the expression for Fourier component of the scalar potential $\Phi_{\vec{q}}$ [16]

$$\Phi_{\vec{q}} = i \sqrt{\frac{2\pi\hbar\omega_L}{\in^* V}} \frac{1}{\sqrt{q_\perp^2 + q_z^2}} e^{-i\left(q_\perp r_0 \cos\varphi + q_z z\right)}$$

the matrix element $M_{|m-m'|; n, n'}(q_\perp, q_z)$ for the energy $\left(-e\sum_{\vec{q}} \Phi_{\vec{q}}\right)$ of electron-phonon interaction on the functions (2) with the quantum number n = 0 has the form:

$$M_{|m-m'|; 0,0}(q_\perp, q_z) = i^{(m-m'+1)} \hbar\omega_L \sqrt{\frac{4\pi\alpha r_p}{V}} \frac{J_{|m-m'|}(q_\perp r_0)}{\sqrt{q_\perp^2 + q_z^2}} \exp(-(q_z R_z)^2/4), \qquad (4)$$

where: $J_{|m-m'|}(y)$ is the Bessel function of the index $|m-m'|$, $r_p = \sqrt{\hbar/(2m_e \omega_L)}$ is the polaron radius, α is the Frohlich coupling constant, $q_\perp$ and q_z are transverse and longitudinal components of phonon wave vectors, ω_L is the limiting *LO-* phonon frequency. Here it is supposed that electron interacts with bulk *LO* - phonons which are considered in the continuum approximation; the dispersion of the phonon spectrum is neglected.

As can be seen from (1), the magnetic field lifts the degeneracy between states with positive and negative values of the quantum number m. But there are so-called "accidental degeneracy" due magnetopolaron effect, since the energy levels of the system as a function of magnetic fields can interfere. The multiplicity of this degeneracy is determined by the number of intersecting energy levels.

3. THE ENERGIES OF DOUBLE AND TRIPLE MAGNETOPOLARON

Consider the problem of the usual double-polaron. The resonance condition in the general case of two levels with quantum numbers n, m, N and n, m', N' takes the following form:

$$\left(\frac{r_p}{r_0}\right)^2 \left(m + \frac{1}{2}\left(\frac{r_0}{R}\right)^2\right)^2 + N =$$
$$= \left(\frac{r_p}{r_0}\right)^2 \left(m' + \frac{1}{2}\left(\frac{r_0}{R}\right)^2\right)^2 + N' \qquad , \quad (5)$$

where N - number of phonons. In the particular case, if you choose $m = 0, N = 0$ and $m' = -1, N' = 1$, the relation (5) for an arbitrary $(r_0/r_p)^2$ can be rewritten as:

$$(r_0/R)^2 = 1 + (r_0/r_p)^2 .$$

There is the intersection of these two above mentioned levels at magnetic fields, corresponding to the condition of resonance relation (6).

The energy spectrum of the double magnetopolaron can be determine by means of perturbation theory for degenerate states [7]. In this case the Schrödinger equation, in the first order perturbation theory, reduces to a system of two linear homogeneous equations. The condition of compatibility of these equations yields the following equation for the energies of the polaron states:

$$(\varepsilon - \varepsilon_{0,0})(\varepsilon - \varepsilon_{-1,0} - \hbar\omega_L) =$$
$$= \sum_{\vec{q}} \left|M_{1;0,0}(q_\perp, q_z)\right|^2 \qquad . \quad (7)$$

The right-hand side of this expression according to (4) is:

$$\sum_{\vec{q}} \left|M_{1;0,0}(q_\perp, q_z)\right|^2 = \alpha(\hbar\omega_L)^2 \frac{r_p}{R_z} \frac{G_1}{\sqrt{2}\pi^{3/2}}, \quad (8)$$

where:

$$G_1 = G_{2,3}^{2,2}\left(2\left(\frac{r_0}{R_z}\right)^2 \middle| \begin{array}{c} \frac{1}{2}, \frac{1}{2} \\ 0, 1, -1 \end{array}\right) \qquad (9)$$

is Meijer function [17]**.** Taking into account (8), the solution of the quadratic equation (7) is:

$$\varepsilon_{1, 2} = \frac{1}{2}(\varepsilon_{0,0} + \varepsilon_{-1,0} + \hbar\omega_L) \pm \sqrt{\frac{1}{4}(\varepsilon_{0,0} - \varepsilon_{-1,0} - \hbar\omega_L)^2 + \frac{\alpha(\hbar\omega_L)^2}{(2\pi^3)^{1/2}} \frac{r_p}{R_z} G_1} . \quad (10)$$

Upon receipt of the equation (7), we restrict ourselves to considering only the interaction of two closely spaced energy levels. Far from resonance should also take into account the contribution from the other levels. The results of numerical calculations of dependence of the dimensionless energy on the dimensionless magnetic field are shown in Figure 1 with the following values of the parameters for GaAs:

$$r_0/r_p = 2, \ R_z/r_p = 4, \ r_p = 4\,\text{nm}, \ \alpha = 0.071,$$

$$\hbar\omega_L = 421\,\text{K}, \ m_e = 0.067\,m_0.$$

In Fig. 1 energy calculated from $\hbar\Omega/2$ - the zero level of size quantization along the axis of NT. At the resonance point, where $(r_p/R)^2 = 1.25$, the magnetopolaron splitting energy $\Delta\varepsilon$ in GaAs NT is about $0.16\,\hbar\omega_L \approx 5.8\,meV$.

The value of magnetopolaron splitting depends not only on the radius, but on the NT length. Figure 2 shows the results of numerical calculations magnetopolaron splitting at the resonance point on the dimensionless

radius and dimensionless length of the NT. In Fig. 2 energy also calculated from the zero level of size quantization along the axis of NT. From this figure it is clear that at the resonance point, energy splitting between levels with m = 0, N = 0 and m = -1, N = 1 decreases with increasing both the diameter and the length of the NT, the last one is characterized by the parameter R_z.

By expanding the expression (9) in a series on small parameter r_0/R_z, limiting zero-order approximation, we find for the splitting of the energy in resonance point the following approximate formula:

$$2\sqrt{\frac{\alpha}{(2\pi)^{1/2}} \frac{r_p}{R_z}}\,\hbar\omega_L \qquad (11)$$

This shows that for thin, long NT splitting at the resonance point depends only weakly on the NT radius and inversely proportional to the square root of the length of NT.

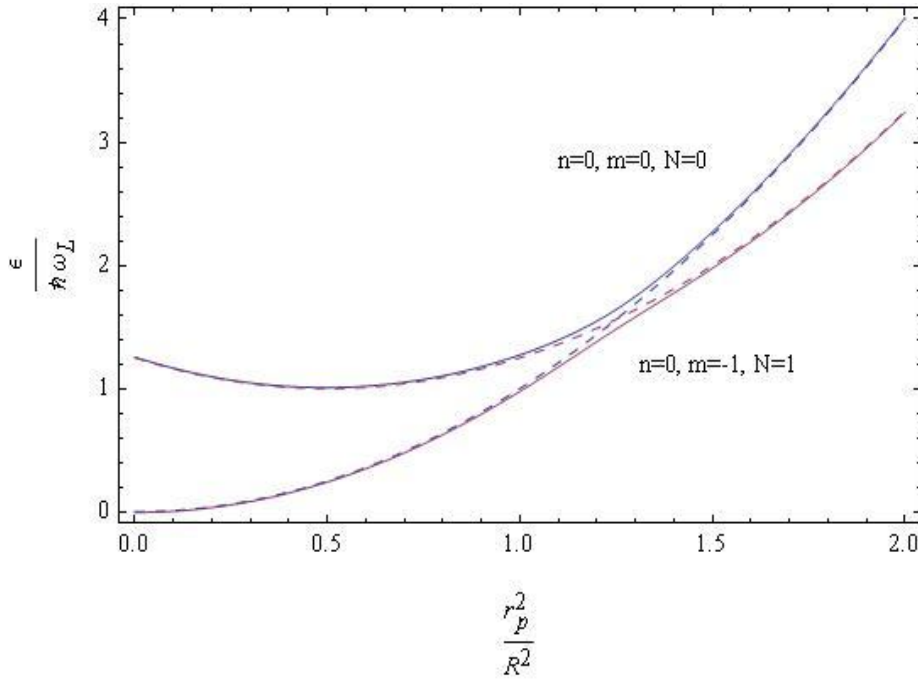*Fig.1.* The energy levels of double magnetopolaron with quantum numbers m = 0, n = 0, N = 0 and m = -1, n = 0, N = 1, depending on the magnetic field. Here $r_0/r_p = 2, \ R_z/r_p = 4$, where *m, n* -levels numbers, *N*-number of phonons; dashed curves correspond to the resonance curves, solid curves - to the splitted magnetopolaron states.
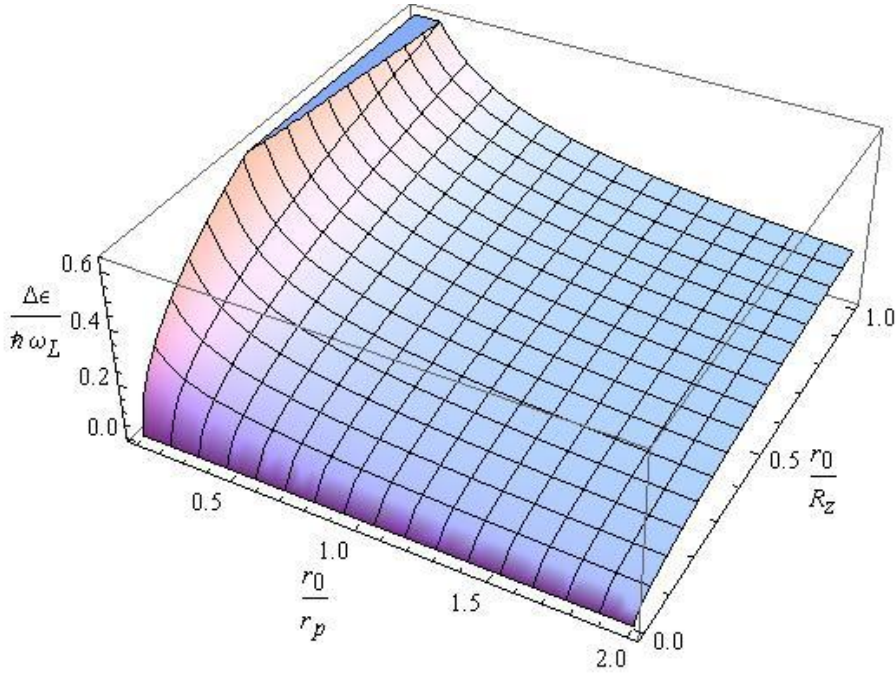
Fig. 2. The dependence of the energy splitting between levels with $m=0$, $n=0$, $N=0$ и $m=-1$, $n=0$, $N=1$ of electron-phonon system on the dimensionless values r_0/r_p, r_0/R_z at the resonance point $(r_p/R)^2 = 1.25$.

Now consider the problem of the usual triple polaron. Solutions are possible only at fixed values $(r_0/r_p)^2$. At the intersection of three discrete levels with a common quantum number $n = 0$, we obtain a triple polaron. In general case for three levels with quantum numbers m_1, N_1, m_2, N_2 and m_3, N_3 the resonance condition takes the following form:

$$\left(\frac{r_p}{r_0}\right)^2\left(m_1 + \frac{1}{2}\left(\frac{r_0}{R}\right)^2\right)^2 + N_1 =$$

$$= \left(\frac{r_p}{r_0}\right)^2\left(m_2 + \frac{1}{2}\left(\frac{r_0}{R}\right)^2\right)^2 + N_2,$$

$$\left(\frac{r_p}{r_0}\right)^2\left(m_1 + \frac{1}{2}\left(\frac{r_0}{R}\right)^2\right)^2 + N_1 =$$

$$= \left(\frac{r_p}{r_0}\right)^2\left(m_3 + \frac{1}{2}\left(\frac{r_0}{R}\right)^2\right)^2 + N_3$$

(12)

One of the solutions of equations (11) for the parameter values $(r_0/r_p)^2 = 6$ and $(r_0/R)^2 = 1$ is defined by the following set of quantum numbers:

$$(m_1 = 0, \ N_1 = 1),$$
$$(m_2 = -1, \ N_2 = 1),$$
$$(m_3 = 2, N_3 = 0).$$

(13)

Under the scheme similar to the calculation of the spectrum of the double polaron, one can obtained the energy spectrum for the triple polaron. We shall consider only the interaction between the three closely spaced energy levels. The Schrodinger equation for three selected levels (13), in first order perturbation theory reduces to a system of three equations. Equating the determinant of the system to zero, to calculate the energies of polaron states is obtained the following cubic equation:

$$(\varepsilon - \varepsilon_{0,0} - \hbar\omega_L)(\varepsilon - \varepsilon_{-1,0} - \hbar\omega_L)(\varepsilon - \varepsilon_{2,0}) =$$

$$= (\varepsilon - \varepsilon_{-1,0} - \hbar\omega_L)\frac{\alpha(\hbar\omega_L)^2}{\sqrt{2}\pi^{3/2}}\frac{r_p}{R_z}G_2 + (\varepsilon - \varepsilon_{0,0} - \hbar\omega_L)\frac{\alpha(\hbar\omega_L)^2}{\sqrt{2}\pi^{3/2}}\frac{r_p}{R_z}G_3, \quad (14)$$

where:

$$G_2 = G_{2,3}^{2,2}\left(2\left(\frac{r_0}{R_z}\right)^2 \left|\begin{array}{cc} \frac{1}{2}, & \frac{1}{2} \\ 0, & 2, -2 \end{array}\right.\right) \quad G_3 = G_{2,3}^{2,2}\left(2\left(\frac{r_0}{R_z}\right)^2 \left|\begin{array}{cc} \frac{1}{2}, & \frac{1}{2} \\ 0, & 3, -3 \end{array}\right.\right), \qquad (15)$$

are Meijer function [17].

The results of numerical calculations of the dimensionless energy depending on the dimensionless magnetic field are shown in Fig.3 for GaAs at the parameter values: $r_0/r_p = \sqrt{6}$, $R_z/r_p = 2\sqrt{6}$, $r_p = 4\,nm$, $\alpha = 0.071$, $\hbar\omega_L = 421K$, $m_e = 0.067\,m_0$. In Fig. 3 energy is also calculated from the zero level of size quantization along the NT.axis.

At the resonance point, where $(r_p/R)^2 = 1/6$, value of the magnetic field at resonance is $B = (\hbar c)/(6er_p^2) \approx 6.84\,Tl$.

Splitting energy of magnetopolaron $\Delta\varepsilon$ between the lower and upper levels is about $0.137\hbar\omega_L \approx 5\,meV$. The splitting between the upper and the middle levels is exactly half the reported value.
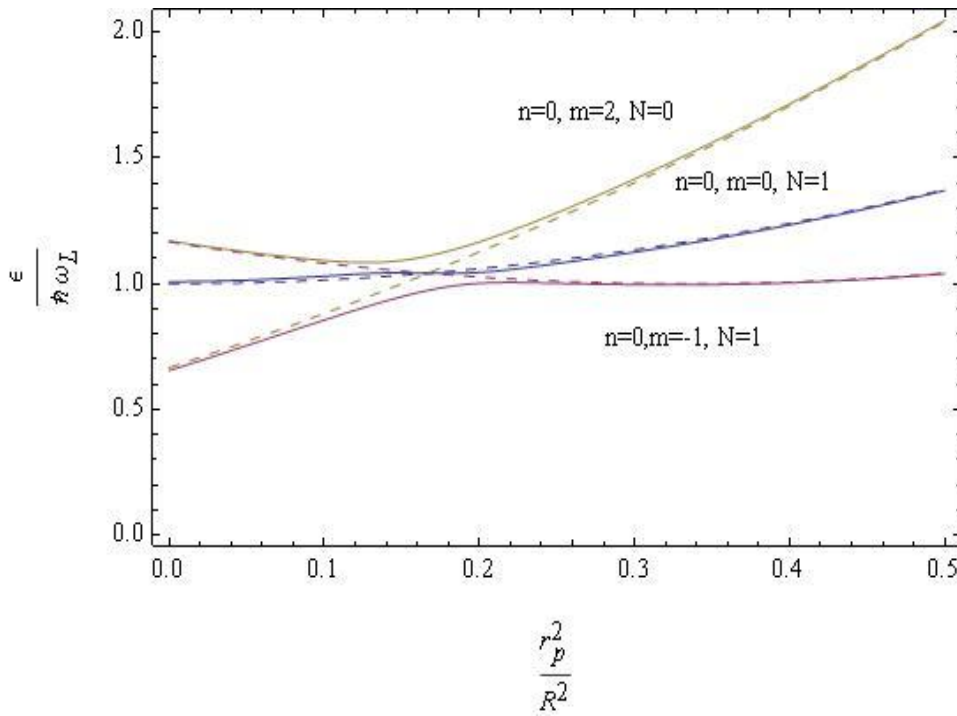
Fig.3. The energy levels of triple magnetopolaron with quantum numbers *n=0, m=1, N=1; n=0, m= -1, N=1* and *n=0, m=2, N=0* depending of the magnetic field. Here $r_0/r_p = \sqrt{6}$, $R_z/r_p = 2\sqrt{6}$, where *m, n* - levels number, *N*-number of phonons; dashed curves correspond to the resonance curves, solid curves - to the splitted magnetopolaron states.

CONCLUSION

Using of perturbation theory the energy splitting for the usual double and triple magnetopolaron near resonance were obtained . Here it was taken into account the usual magnetopolaron that arises from the intersection of energy levels with different magnetic quantum numbers, but with the same quantum numbers of size-quantization. Electron- phonon interaction leads to the repulsion of energy levels at the points of intersection. The energy splitting is inversely proportional to the square root of the length of NT and decreases slightly with increasing diameter of the NT. Energy splitting at resonance point is about 6 MeV for GaAs nanotube with length 32 nm.

The effect of the repulsion of the levels will be manifested itself in the magnetic fields corresponding to the resonance point in the experiments on interband absorption and Raman scattering.

_____

[1] *E.J. Johnson and D.M Larsen.* 1966 Phys. Rev. Lett. **16** 655-9

[2] *L.I. Korovin, S.T. Pavlov, B.E. Eshpulatov.* 1993 Phys.Solid State **35** 1178-84

[3] *L.I. Korovin, S.T. Pavlov, B.E. Eshpulatov.* 1993 Phys.Solid State **35** 788-94

[4] *L.I. Korovin, I.G. Lang and S.T. Pavlov.* 1997 JETP Lett. 65 532-6

[5] *L.I. Korovin, I.G. Lang and S.T. Pavlov.* S T 1999 JETP **89** 764-74

[6] *I.G. Lang, V.I. Belitsky, A. Cantarero, L.I. Korovin, S.T. Pavlov and M. Cardona.* 1997 Phys. Rev. B **56** 16880-88

[7] *I.G. Lang, L.I. Korovin and S.T. Pavlov.* 2005 Phys.Solid State **47** 1771-78

[8] *O.Z. Alekperov, N.M. Guseinov.* 2003 Mod. Phys. Lett. B **17** 1167 -74

[9] *L. Jacak, J. Krasnyj, D. Jacak and P. Machnikowski.* 2003 Phys. Rev. B **67** 035303 (13)

[10] *S. Das Sarma*. 1984 Phys. Rev. Lett. **52** 859-62

[11] *F.M. Peeters, J.T. Devreese.* 1985 Phys. Rev. B **31** 3689- 95

[12] *I.N. Kotelnikov, V.A. Kokin, Yu.V. Fedorov, A.V. Guk, D.T. Talbayev.* 2000 JETP Lett. **71** 387-90

[13] I.*G. Lang, V.I. Belitsky and A. Cantarero, L.I. Korovin, S.T. Pavlov, M. Cardona*. 1996 Phys. Rev. B 54, 17768-78

[14] *V.A.Geiler, V.A.Margulis and A.V. Shorokhov.* 1999 JETP **88** 800-6

[15] *V.A. Margulis, A.V. Shorokhov, M.P. Trushin.* 2000 Phys. Lett. A **276** 180- 8

[16] *N.M.Guseinov, O.Z.Alekperov, S.S. Guseinova.* 2006 Mod. Phys. Lett. B, 20 1771-6.

[17] *I.S. Gradshteyn, I.M. Ryzhik , Alan Jeffrey and Daniel Zwillinger.* (Eds.) 2007 Table of Integrals, Series and Products,7th edn, Academic press 1200 pages

DIELECTRIC PROPERTIES OF TlGaTe₂ CRYSTALS IRRADIATED BY γ – QUANTUMS

R.M. SARDARLI, O.A. SAMEDOV, A.P. ABDULLAYEV, F.T. SALMANOV, S.F. SAMEDOV, N.A. ALIYEVA

Institute of Radiation Problems of Azerbaijan NAS
370143, B.Vahabzade ave.,9, Baku

Research of temperature dependence of dielectric constant of crystals TlGaTe₂ irradiated by γ - quantum are shown that along tetragonal axis *c*, the maximum value of the dielectric permeability, irradiated with dose *D*=100Mrad, in 6 times exceeds a reference value. Energy of activation ($E^a_{//}$ =0.66 eV and $E^a_{\perp}$ = 0.38eV), its frequency "try" vibration ($v_{//}$ =2.5·10^{13} Hz and $v_{\perp}$ = 6.3·10^{12} Hz) which get to frequency area phonon mode of a vibration spectrum of this crystal is defined.

INTRODUCTION

In previous publications [1-4] it is shown that in TlGaTe₂ crystals the conductivity has the ion (superion) character higher temperature 300K. It is established that Tl$^+$ ions diffusing on vacancies in thallium sublattice between nanorods (Ga^{3+}Te^{2-}₂) are responsible for superion conductivity. The relaxation character of dielectric anomalies that supposes the existence of electric charges weakly connected with crystal lattice is established. The dipoles of Tl$^+$-rods (Ga^{3+}Te^{2-}₂)$^-$ appearing as a result of melting of thallium sublattice and jumps of Tl$^+$ ions from one localized state to another one, are relaxators in TlGaTe₂ crystals at transition into superion state. The effect of TlGaTe₂ crystal transition induced by the field into superion state is revealed. The temperature dependences (90÷300K) of *σ(T)* electric conduction measured in both experiment geometries (parallel and perpendicular to rods) and volt-ampere characteristics (VAC) of TlGaTe₂ single crystals are investigated in [5]. It is shown that *σ(T)* dependence measured in VAC ohmic region has hopping character and is described in Mott approximation. VACs of TlGaTe₂ crystals in the region of more strong current growth subjected to different doses of γ-radiation are investigated.

It is shown that this VAC region is described within the framework of Pul-Frenkel thermo-field effect. The concentration values of N$_f$ ionized centers, *λ* the free path, *β* Frenkel coefficient value, potential well form in initial and irradiated TlGaTe₂ crystals are defined. It is shown that conduction anisotropy changes under the radiation influence leading to translation order of nanorods.

The behavior peculiarities of temperature dependences of dielectric constant (*ε(T)*) and loss tangent (*tgδ(T)*) of TlGaTe₂ crystal subjected to different doses of γ -radiation are investigated in the given work.

EXPERIMENT TECHNIQUE

The samples of TlGaTe₂ compound are synthesized by alloying of initial components (the purity not less 99,99) in vacuum quartz ampoules and their single crystals are grown by modified Bridgman method. The freshly cleaved samples in which crystal axis "c" is oriented in chip plane have the rectangular form. For measurement of temperature dependences of TlGaTe₂ crystal electric conductions the condensers in which the investigated material planes serve in the capacity of dielectric. The condenser coatings are obtained by the application of silver conductive paste on plate surfaces. The investigations of electric conduction are carried out by immittance digital measuring device E7-20 in temperature interval 100÷450K. The amplitude of measurement filed doesn't exceed 1V·cm^{-1}. After preliminary measurements of *tgδ(T)* and *ε(T)* the samples are irradiated by γ-rays from standard radiation source Co^{60}. The radiation dose is accumulated gradually in each of investigated samples by the means of consistent expositions of γ – influence up to value 250Mrad.

EXPERIMENTAL RESULTS AND DISCUSSION

As it is known [5] in superion conductors at temperature increase the exponential increase of dielectric constant (*ε*) which at high temperatures can achieve enough big values, is observed besides the exponential growth of electric conduction.

The frequency dependences of loss tangent maximum value (*lgf$_{max}$*) on temperature for TlGaTe₂ crystal are presented on fig.1.
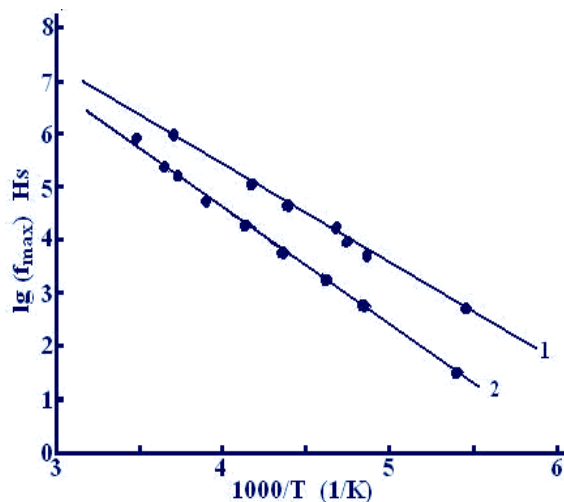

Fig.1. The frequency of relaxation maximum of dielectric loss tangent in function of its reversal temperature for TlGaTe₂ (1 is perpendicular of tetragonal "c" crystal axis, 2 is parallel to it).

The frequency dependences of dielectric constant and dielectric loss tangent of TlGaTe₂ compound have been investigated earlier in work [2]. It is established that the maximum values $\varepsilon(v,T)$ and $tg\delta(T)$ shift to more high temperatures and the value in maximum $\varepsilon(v,T)$ and $tg\delta$ decreases with increase of measurement field frequency. The temperature-frequency characteristics $\varepsilon(v,T)$ and dielectric loss tangent $tg\delta(v,T)$ have evidently expressed peculiarities for relaxation processes of Debye type with participation of minimum two relaxors in whole investigated temperature region. The temperature dependence of maximum T_ε, which is character for low-temperature anomaly on measurement field frequency, shows the anomaly relaxation character. The last one proposes the existence of electric charges in crystal lattice weakly bond with it. One can use the oscillator model with big damping [6] for description of dielectric constant relaxation peak. The model considers the displacement of particles n with charge e in potential wells with the distance between their minimums a and barrier height W. The eigenfrequency of particle oscillation in well v is "try" one in respect to less frequency of particle jumps between minimums ($2ve^{-W/kT}$).

The theoretic consideration shows [6] that maximum $tg\delta$ precedes to relaxation maximum ε on temperature. This maximum is revealed in в TlGaTe₂ (see [2]) and it is experimentally easy studied as it reveals in comfortable frequency intervals (500Hz - 1мHz) and not high temperature (100-450K). Neglecting the through electric conductivity which is more insignificant one in temperature interval we can use for description of tangent anomaly the following expression [7]:

$$tg\delta(T) = \frac{\omega n e^2 a^2 / \varepsilon_\infty}{kT\left(\dfrac{\varepsilon_S}{\varepsilon_\infty} + \dfrac{\omega^2}{4v^2}e^{2W/kT}\right)} \cdot \frac{e^{W/kT}}{2v} \quad (1)$$

where ε_∞ is dielectric constant on infinitely big frequency; ε_s is statistic dielectric constant. The extremum search on temperature for $tg\delta$ is easily carried out under following condition $\dfrac{\omega}{2v} << 1$, $\dfrac{2W}{kT} >> 1$ and leads to equation for maximum temperature:

$$\ln \frac{2v}{\omega_{max}} = \frac{W}{kT} \text{ или } \omega_{max} = 2v\ e^{-W/kT} \quad (2)$$

The obtained data allows us to find the jump activation energy, its (try) oscillation frequency at which the jumps through potential barrier are possible. This frequency is easily found by the construction of lgf_{max} dependence in function $1/T$ for TlGaTe₂ (fig.1).

The line extrapolation to $1/T \rightarrow 0$ defines the try oscillation frequency and gets to frequency region $v_{//}= 2.5 \cdot 10^{13}$ Hz and $v\perp = 6.3 \cdot 10^{12}$ Hz that corresponds to long-haul part of IR-spectrum which gets to frequency region of phonon modes of this crystal oscillation spectrum. The line inclination gives the one act energy of charge transfer through barrier $E^a_{//} = 0.66$eV and $E^a\perp=0.38$eV. The

obtained frequency for electron processes is too low one. The compound TlGaTe₂ structure can be expressed as the system consisting of two subsystems: rigid subsystem in the form of negatively charged chains (GaTe₂) lying in plane (001) and more mobile system of thallium ions [8]. Earlier, it was mentioned by us that from crystal-chemical point of view, TlGaTe₂ structure in largest degree favors to Tl⁺ cation mobility. The temperature dependence $lg\ f_{max}$ at line extrapolation to $1/T \rightarrow 0$ is in oscillation region of low-frequency phonons in phonon spectrum of TlGaTe₂ crystal [9]. The symmetries of these phonons are A₂ᵤ and Eᵤ [9] and correspond to oscillations of heavy atoms Tl¹⁺. Thus, especially heat oscillations of thallium subsystem, phonons with symmetries A₂ᵤ and Eᵤ where the atom oscillations are presented, lead to the fact that try oscillation energy is higher than potential barrier after which thallium subsystem melts and crystal transition in superion state takes place. The oscillation spectrum investigations of TlGaTe₂ crystal in terahertz region [3] reveal the oscillation at measurement E//C which is lower by frequency than symmetry low-frequency phonon mode a₂ᵤ. This oscillation is related to chain libration one $(Ga^{3+}Te^-_2)^-$ as especially at this temperature the sublattice Tl⁺ begins to melt, the bond between chains and Tl⁺ weakens that is the reason of chain libration oscillations. Note that these low-frequency oscillations are observed only in E//C geometry.

Above it is discussed the ion disorder in the dependence on TlGaTe₂ crystal temperature. Towards with the fact the disorder degree can change under the influence of γ-radiation.

The temperature dependences of dielectric constant $\varepsilon_{//}(T)$ and $\varepsilon\perp(T)$ of initial samples and radiated crystals TlGaTe₂ are given on figures 2 and 3.

It is known that γ - radiation of the crystals leads to formation of radiated defects in the form of vacancies, internodal atoms and also defect complexes of different type interacting between it and with chemical impurities.

As it is seen from fig.2, the maximum value of dielectric constant increases (fig.2 curve 2) at the increase of radiation doze up to 100 Mrad. The dominated role in these processes play the defects of ionization type (charged defects) which appear in result of radiation by γ-quantums, i.e. The radiation-stimulated healing of structural defects leading to increase of crystal dielectric constant.
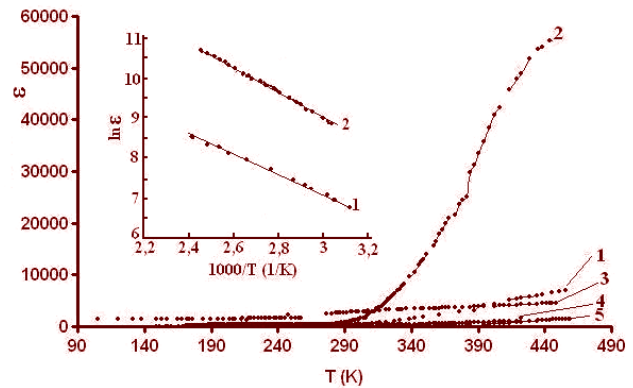

Fig.2. The temperature dependence of dielectric constant ε(T) for TlGaTe₂ crystal treated by γ-radiation (curves 1-5: 0; 100; 150; 200; 250 Mrad).

The further increase of radiation dose leads to decrease of dielectric constant that connects with increase of crystal structure deficiency under the influence of γ-quantums. The dose power 100 Mrad is the critical one at which the dielectric constant TlGaTe$_2$ begins to decrease. At further increase of dose of γ - radiation the quantity of radiation defects increasing leads to mobility decrease and consequently to decrease of dielectric constant. As it is seen from the figures 2 and 3, the experimental points of ln(ε) dependence well lay on direct line [10,11]:

$$E^c(T)= \varepsilon_0 \exp(-\Delta E^a/kt) \qquad (3)$$

The activation energy calculated by formula (3) at both measurements parallel to tetragonal axis of "*c*" crystal and perpendicular to it

The measurements are carried out parallel to tetragonal axis "c", lnσ(T) dependences on 1000/T on frequency 1mhz are given on insertion.

Fig.3. The temperature dependence of dielectric constant ε(T) for TlGaTe$_2$ crystal treated by γ-radiation (curves 1-5: 0; 100; 150; 200; 250 Mrad).

The measurements are carried out parallel to tetragonal axis "c", lnσ(T) dependences on 1000/T on frequency 1mhz are given on insertion.
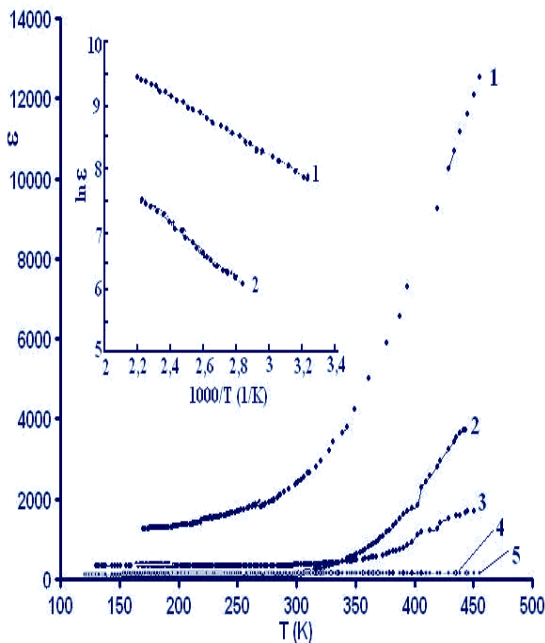
TlGaTe$_2$ crystal for nonradiated samples are equal: $\Delta E_\parallel$=0,22ev and $\Delta E_\perp$=0,14ev for samples treated by radiation by dose in 100 Mrad: $\Delta E_\parallel$=0,27ev and $\Delta E_\perp$ =0,19ev).

CONCLUSION

Thus, the obtained data allows us to find the jumping activation energy, its frequency of (try) oscillations at which the jumping through potential barrier is possible. This frequency is defined by the way of construction of dependence lgf$_{max}$ in function1/T for TlGaTe$_2$. The obtained frequency of try oscillations is equal to $\nu_\parallel$= $2.5 \cdot 10^{13}$ Hz and $\nu_\perp$= $6.3 \cdot 10^{12}$ Hz that corresponds to further terahertz part of IR-spectrum and overlaps the region of low-frequency oscillation spectrum of TlGaTe$_2$ crystal. It is supposed that Tl$^+$ sublattice begins to melt at transition of system into superion state, the bond between chains and Tl$^+$ weakens and the libration chain oscillations (Ga^{3+}Te$^{2-}_2$) are possible. Such oscillations are observed in work [9] in E//C experiment geometry and are connected with chain libration oscillations (Ga^{3+}Te$^{2-}_2$) .

It is shown that along tetragonal axis "c" of TlGaTe$_2$ crystal, the maximum value of dielectric constant is observed at dose D=100 Mrad that in 6 times exceeds the initial values of dielectric constant of TlGaTe$_2$ crystal and transition temperature in superion state shifts to the side of low temperatures.

The investigations of dose dependence of dielectric constant of TlGaTe$_2$ crystal show on appearance possibility (at definition of dose critic value) of jumping disorder of Tl$^+$ ion sublattice which is accompanied with jumping change of dielectric constant.

It is mentioned that the described effect gives the possibility to realize the superion state in TlGaTe$_2$ crystal at enough comfortable temperatures from applied point of view. This opens the wide possibilities of practice application of superion state of TlGaTe$_2$ crystal.

[1]. *R.M. Sardarli, O.A. Samedov, A.P. Abdullayev, F.T.Salmanov.* Qiqantskaya dielektricheskaya relaksachiya v kristallax TlGaTe$_2$. FTT, 2011, t.53, v.8, str.1488-1492. (in Russian).

[2]. *R.M. Sardarli, O.A. Samedov, A.P. Abdullayev, E.K.Quseynov, E.M. Qodjaev, F.T. Salmanov.* Superionnaya provoimost v kristallax TlGaTe$_2$. FTP, 2011, t.45, v.8. Str.1009-1013. (in Russian).

[3]. *P.M. Sardarly, O.A. Samedov, A.P. Abdullaev, F.T.Salmanov, A. Urbanovic, F. Gare., J-L. Coutaz.* Superion Conductivity in One-Dimensional Nanofibrous TlGaTe$_2$ Crystals. Jpn. J. Appl. Phys., 2011, 50, 05FCO9-1-2.

[4]. *R.M. Sardarli, O.A. Samedov, A.P. Abdullayev, E.K.Quseynov, F.T. Salmanov, O.Z. Alekperov, E.K. Quseynov, N.A. Alieva.* Superionnaya provodimost, effekti perekllyuceniya I pamyati v kristallax TlInSe$_2$ I TlGaTe$_2$. FTP, 2011, t.45, v.11, str.1441-1445.(in Russian).

[5]. *R.M. Sardarli, O.A. Samedov, A.P. Abdullayev, E.K.Quseynov, F.T. Salmanov, Q.R. Safarova.* Osobennosti provodimosti γ-oblucennix kristallov TlGaTe$_2$ s nanocepocecnoy strukturoy. FTP, 2010, t.44, v.5, str.610-614.(in Russian).

[6]. *A. Lidyard.* Ionnaya provodimost kristallov. Izd-vo IL, M:. 1962, 222s. (in Russian).

[7]. *S.Yu. Stefanvic, L.A. Ivanova, A.V. Astafev.* Ionnaya I superionnaya provodimost v seqnetoeletrikax. M.: NIITEXIM, 1989, 80 str.(in Russian).

[8]. *V.D. Muller, H. Hahn.* Zur structur des tlgase₂. Z. Anorg. Und allgem. Chem. 1978, №1, v.438, p.258-272.

[9]. *A.M. Panich and R.M. Sardarly:* Physical properties of the low dimensional A^3B^6 and $A^3B^3C^6_2$ compounds. (Nova Science Publishers. Inc. New York, 2010, p.287.

[10]. *L.S. Parfeneva, A.I. Shelix, A.I. Smirnov, A.V. Prokofev, V. Assmus.* Elektroprovodnost I dielektricheskaya pronichaemost odnomernoqo superionnoqo provodnika LiCuVO₄. FTT, 2004, t.46, v.6, str.998-1000. (in Russian).

[11]. *L.S. Parfeneva, A.I. Shelix, A.I. Smirnov, A.B. Prokofev, V. Assmus, X. Misiorek, Ya. Muxa, A. Ejovskiy, I.Q. Vasileva.* Perenos tepla po nemaqnitnim litievim chepochkam v novom odnomernom superionike LiCuVO₄. FTT, 2003, t.45, v.11, str.1991-1996. (in Russian).

PERFORMANCE OF SILICON MICROPIXEL AVALANCHE PHOTODIODES AFTER IRRADIATION BY 150 MeV PROTON BEAM

Z.Y. SADYGOV[1,3], F.I. AHMADOV[2,3], N.V. ANFIMOV[3], X.I. ABDULLAEV[4], A. A. DOVLATOV[1], Z.V. KRUMSHTEIN[3], R.S. MADATOV[2], A.G. MOLOKANOV[3], A.A. NOZDRIN[3], A.G. OLSHEVSKI[3], N.A. SAFAROV[1], V.N. SHVETSOV[3]

[1]*Institute of Physics ANAS, AZ-1143, Baku, Azerbaijan,*
[2] *Institute of Radiation Problems ANAS , AZ-1143, Baku, Azerbaijan ,*
[3]*Joint Institute for Nuclear Research, 141980, Dubna, Russia,*
[4]*Azerbaijan National Academy of Aviation, AZ-1045, Baku, Bina, Azerbaijan*

The effects of radiation damage in micropixel avalanche photodiodes have been studied. The devices have been irradiated by 150 MeV protons to $5 \cdot 10^{10}$ proton/cm^2 dose. Particular attention was given to investigate behavior of dark current and noise of micropixel avalanche photodiodes after irradiation.

Micropixel avalanche photodiodes (MAPD) are used widely in a large number of fields of science and technology: physics, medicine, environmental sciences, elementary particle physics et al. MAPD which are known as an ultra high pixels density diode has been showed as one of the best candidate for calorimeters in high energy physics. The device is supposed to operate in a high radiation environment in many applications. Therefore, the radiation damage is a critical issue for photo detectors for these practical applications [1, 2].

This paper is dedicated to investigation of influence of 150MeV energy protons on the MAPD performance. Design and operation principles of the MAPD are described in [3, 4]. Tested devises named as MAPD-3N1P and MAPD-3B have 3×3 mm^2 active area and pixel density 15000 and 40000 pixels/mm^2, respectively. The both type devices had been produced in collaboration with Company Zecotek Photonics Inc.

A proton beam with energy of 150 MeV from the PHAZOTRON accelerator in Laboratory of Nuclear Problems of Joint Institute for Nuclear Research was used for the irradiation. The beam had a rectangular shape with an area of 50 cm^2, which was larger than the active area of holder (the holder's area was 25 cm^2). The homogeneity of the beam intensity within the 25 cm^2 region was better than 7%. The proton intensity was 1×10^8 p/cm^{2}sec. MAPD devices were irradiated at room temperature. Reverse voltage ($\sim$ 9V) was applied to each diode during the irradiation.

Keithley 6487 device was used as an ammeter and a voltage source in the experiments. The light emitting diode with 100 ns light pulse duration, 450 nm wave length and 1kHs frequency has been used for calculation of gain and noise. The signals were read out from 1kΩ load resistor through the coupling capacitor and a line amplifier (K=37). Delayed signal was fed into ADCM16-LCT ADC. CAEN N-48 shaping discriminator was used to form a gate signal for the ADC. Digitized signal was read out by a personal computer. Peak positions and their dispersion were obtained from Gaussian fit. The formula

$RMS = \sqrt{\sigma_A^2 - \sigma_0^2}$ was used to calculation noise, where σ_A -dispersion of signal, σ_0 - dispersion of amplifier.

Six MAPD diodes were used in experiments. Three of them were MAPD-3B (#B1, #B2, #B3) and the rest was MAPD-3N1P (#P1, #P2, #P3). The diodes were tested and found to display nearly similar volt-ampere and gain-voltage characteristics prior to irradiation. It was found optimal working voltages 70.5V for MAPD-3B and 93.9V for MAPD-3N1P. Gain of MAPD-3B and MAPD-3N1P were 1.25×10^4 and 5.8×10^4 under optimal biases respectively. It was reasonable to assume that the irradiated diodes were one diode with different doses. One of the each type of MAPD (#B1 and #P1) has been used as reference for MAPD diodes after irradiation. The diodes #B2 and #P2 were irradiated to 1×10^{10} p/cm^2 dose, while the diodes #B3 and #P3 were irradiated to 5×10^{10} p/cm^2.

Fig. 1 illustrates dependence of dark currents of MAPD-3B (1a) and MAPD-3N1P (1b) photodiodes on bias voltage before and after irradiation. After irradiation the diodes had been kept for two days at room temperature and then its characteristics were measured.

It can see that dark current of MAPD-3B is increased 12.4 and 54 times after irradiation at operation voltage. Dark current of MAPD-3N1P is increased 18 and 81.5 times after irradiation at operation voltage.

Noise-voltage dependences of MAPD-3B (2a) and MAPD-3N1P (2b) samples before and after irradiation are shown in Fig.2. After dose 1×10^{10} proton/cm^2 the noise of MAPD-3B and MAPD-3N1P are increased 2.75 and 4.37 times. As the dose reach 5×10^{10} proton/cm^2 noise of MAPD-3B and MAPD-3N1P increase up to 5.82 and 9.19 times, respectively.

The measurements has shown that the dose of $5 \cdot 10^{10}$ p/cm^2 is not very critical for the MAPD devices. Despite the changes in the dark current and nose after irradiation the device still can be operated after such a dose. In order to have the same signal gain working voltages should be increased about 0.2V.
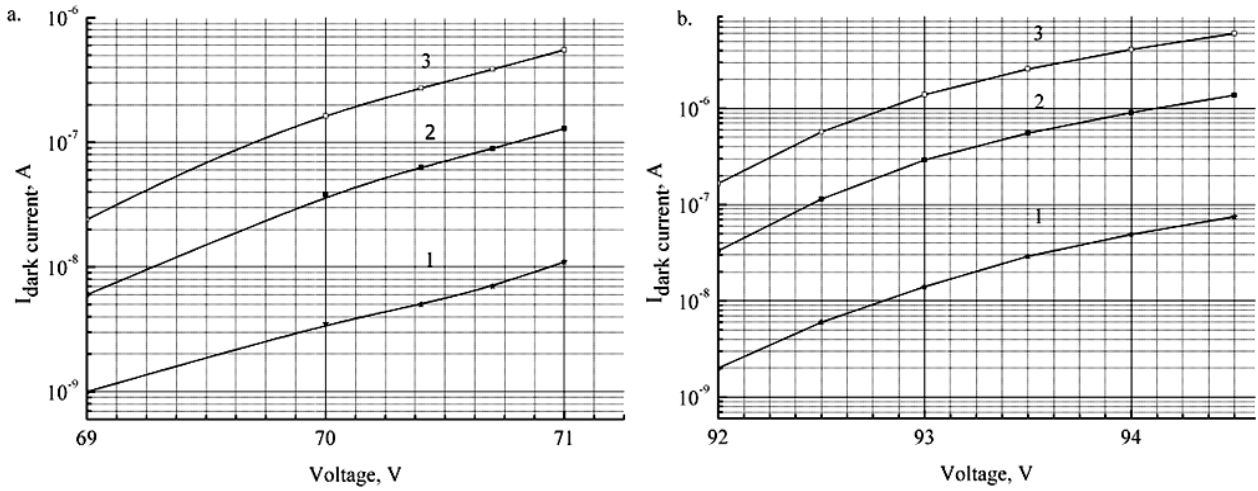
Fig. 1. Volt-ampere characteristics of dark currents of MAPD-3B (a) and MAPD-3N1P (b) diodes. 1 − before irradiation, 2 − after dose $1×10^{10}$proton/cm^2, 3 − after dose $5×10^{10}$proton/cm^2.
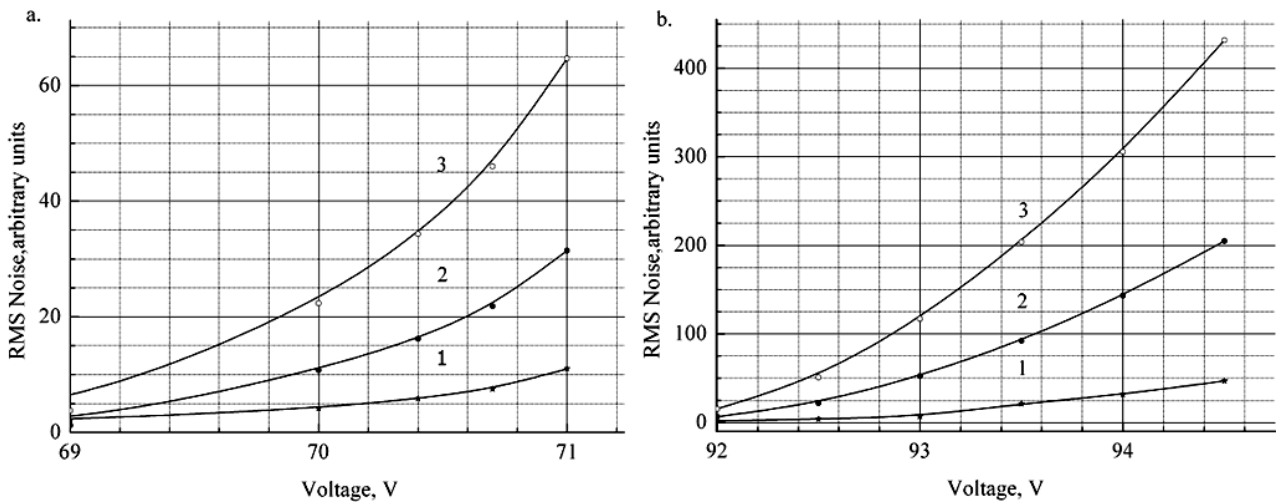
Fig. 2. RMS noise-voltage characteristics of MAPD-3B (a) and MAPD-3N1P (b) diodes . 1 − before irradiation, 2 − after dose $1×10^{10}$proton/cm^2, 3 − after dose $5×10^{10}$proton/cm^2 .

_____

[1] *N. Anfimov, I. Chirikov-Zorin, A. Dovlatov, et al.,* Nucl. Instr. and Meth. A 617 (2010) 78–80.

[2] *Y.V. Musienk, D. D.Renker, U.K. Deiters.* Nuclear Instruments and Methods in Physics Research A (NIM-A) 610 (2009) 87–92.

[3] *Z. Sadygov, A.F.Zerrouk, A.Ariffin, S.Khorev, J.Sasam, T.Bokova, A.Olshevski , N.Anfimov , V.Chalishev,* Nuclear Instruments and Methods in Physics Research A 610 (2009) 390–392

[4] *Z. Sadygov.* Russian Patent № 2316848, priority from 01.06.2006.

STRUCTURE AND ELECTRICAL ACTIVITY OF STRUCTURE DEFECTS OF $Cu(In_xGa_{1-x})(S_{1-y}Se_y)_2$ THIN FILMS

E.P. ZARETSKAYA[1], V.F. GREMENOK[1], A.P. ODRINSKY[2], N.N. MURSAKULOV[3], N.N.ABDULZADE[3], CH.E. SABZALIYEVA[3]

[1] *Scientific-Practical Materials Research Centre NAS of Belarus, P. Brovka 19, 220072 Minsk, Belarus Tel: +375 17 284 12 49, E-mail: ezaret@iftp.bas-net.by,*
[2] *Institute Technical Acoustics NAS of Belarus, Lyudnikova av. 13, 210017 Vitebsk, Belarus Tel:+375-29-6338467, Email:odra@mail333.com*
[3]*Institute of Physics, National Academy of Azerbaijan, H. Cavid ave., 33, Baky, Az-1143,e-mail: nmursakulov@physics.ab.az*

To develop technology of preparation of thin film CIGS solar cells the structure and electrical activity of structural defects of $Cu(In_{1-x}Ga_x)(S_ySe_{1-y})_2$ thin films was investigated. For studying the electrically active defects the photo-induced current transient spectroscopy (PICTS) was used in which light excitation of a sample is employed. The peculiarities of PICTS registration of defect recharging have been established. The peculiarities can be explained in the frame of Lany-Zunger model of the native metastable defect of CIGS. The experimental evidence of such explanation is presented.

1. INTRODUCTION

$CuInSe_2$ (CIS) is one of the most attractive materials for the development of second generation, high-efficient and low-cost thin film solar cells [1,2]. Replacement of the CIS by its multinary analog $Cu(In_{1-x}Ga_x)(S_ySe_{1-y})_2$ (CIGSS) has been demonstrated to shift the band gap of the absorber material toward a better alignment with the solar light spectrum, allowing the device fabrication with advanced performance.

Electrically active defects in CIGSS layers play an important role in the photovoltaic conversion efficiencies. Then, investigation and control of defects is one of the most important issues for highly efficient solar cells based on CIS and its solid solutions. A complete solar cell structure contains more than four layers, which makes precise attribution of the observed defects a very complicated task. Numerous investigations of defects in CIGS materials mainly deal with the completed structure of a solar cell. The studies performed on individual layers (partial structure) are lacking [3].

The use of the conventional techniques for the defects detection at intermediate stages of solar cells fabrication requires the formation of electrical contacts anyhow changing the properties of the material in the contact region, because the DLTS techniques deal with depletion region of Schottky barrier (or heterojunction in case of a completed solar cell). On the other hand the Photo-Induced Current Transient Spectroscopy (PICTS) method that is based on analysis of temperature dependencies of a transient photoresponse signal is effectively used to investigate deep level defects in high resistivity semiconductors [4,5]. However, this method is practically unused for studies of CIGSS solid solutions forming absorber layers.

The aim of this work is to study deep level defects in $Cu(In_xGa_{1-x})(Se_{1-y}S_y)_2$ (CIGSS) thin films obtained by two-step annealing. As far as we know it is a first attempt to apply PICTS for defects investigation in a thin film of CIGSS absorbers [6].

2. EXPERIMENTAL

Single-phase thin films of $Cu(In_xGa_{1-x})(Se_{1-y}S_y)_2$ solid solutions were synthesized by two-step annealing of Cu-In-Ga metallic alloys in S/Se ambient [7]. Reaction time, temperature and S/Se weight ratio were used to control the reaction kinetics. The metallic precursors Cu-In-Ga with a total thickness of about 1.0 μm were deposited onto Corning glass substrate by ion-beam plasma evaporation in vacuum $5 \cdot 10^{-6}$ Torr at a substrate temperature of 100 ^{0}C. At the first stage of the annealing, the precursors were reacted to Se/S under N_2 flow for a period between 20-30 min at $T_1 = 260$ ^{0}C. Then the temperature T_2 (high-stage recrystallization temperature) was raised to 400÷540 ^{0}C at 9 ^{0}C min^{-1} and thereafter held for 20 min. The bulk composition and surface morphology of the films were investigated by energy dispersive X-ray (EDX) analysis using a CAMECA SX-100 and JEOL 6400 SEM apparatus. The depth profiling was done by Auger electron spectroscopy (AES) using a Perkin Elmer Physical Electronics model 590. An Ar ion beam was used for sputter etching. The crystal structure of the materials was studied by X-ray diffraction (XRD) using a Siemens D-5000 diffractometer (having CuK_α ($\lambda = 1.5418$ Å radiation purified by graphite monochromator and operated at 30 kV and 20 mA).

The optical parameters of the reference CIGSS thin films on Corning glass substrates were determined from transmittance (T) and reflection (R) measurements in the spectral range of 200 – 3000 nm at room temperature using a Carry 500 Scan UV-Vis-NIR spectrophotometer (Varian, USA). The investigation of deep level defects was performed by PICT Spectroscopy in the temperature range from 77 to 330 K with a temperature step of 1 K and the sample heating rate of 2 K/min. The analysis of the experimental data was made according to the conventional DLTS technique with registration of the characteristic relaxation time that ranged from 0.2 to 20 ms. The details of the PICTS technique measurements were described in [6,10].

Table 1.

Composition and properties of single-phase Cu(In$_x$Ga$_{1-x}$)(Se$_{1-y}$S$_y$)$_2$ thin films
obtained by annealing in S/Se atmosphere

Sample №	Cu, at.%	In, at.%	Ga, at.%	S, at.%	Se, at.%	S /(S+Se)	E_g, eV	ρ, Ω·cm	Thermopower ζ, μB/K
A1	18,34	29,44	2,19	19,89	30,21	0,39	1.27	1.5×10^2	96
A2	20,50	30,46	0,95	32,27	15,83	0,67	1.29	8.8×10^1	15
A3	20,15	30,29	1,57	42,05	5,94	0,88	1.41	9.9×10^1	9
A4	21,18	29,71	2,16	36,25	10,71	0,77	1.31	9.2×10^{11}	16
A5	19,68	30,53	0,54	41,55	7,70	0,84	1.38	5.4×10^{-1}	28

3. RESULTS AND DISCUSSION

3.1. Structural analysis.

The XRD studies were carried out in order to identify the crystallinity and various phases present in CIGSS thin films. JCPDF data cards 80-2189, 82-1531, 81-0903 and 36-1311 were used to index the peaks were found to be strongly dependent on their composition as well as processing regimes. All the major diffraction peaks associated with the chalcopyrite structure (CH) are already detected for CIGSS films grown under relatively low temperature 400-450 ^{0}C. A higher recrystallization temperature (500 ^{0}C) resulted in a high intermixing of the material.

The characteristic reflections of the CH, such as (101), (103) peaks and splitting of the doublets (116/312), (008/400), (228/424) were clearly observed. The diffraction peaks of CIGSS solid solutions shift to a higher angle with an increase of sulfur and gallium content.

Single-phase CIGSS thin films of the CH structure with [112] preferred orientation were formed under optimized conditions (T_2 of 500 ^{0}C). The characteristic reflections of the CH, such as (101) peaks at $2\theta = 17.42°$ and (211) at $2\theta = 36.08°$ were clearly observed for these films.

When increasing the high-stage temperature to 520-540^{0}C, an obvious improvement in the crystal structure of these films was noticed. The improvement of long-range ordering in the lattice was evidenced from the increase of the degree of preferred orientation I$_{112}$/I$_{220/204}$ from 2 to 4. Careful XRD measurements revealed symmetric (112) reflection (Fig. 1, insert) with no evidence of compositional broadening.

Table 1 presents composition, optical band gap values E$_g$ as well electrical characteristics for single-phase homogeneous Cu(In$_x$Ga$_{1-x}$)(Se$_{1-y}$S$_y$)$_2$ thin films that were synthesized according to the method described above.

The AES measurement for CIGSS thin films (see Table 1) showed the uniform distribution of elements Cu, In, Ga, S and Se through the depth of the layers withought the formation additional phases in material that agrees with the XRD data (Fig. 2).

Typical surface SEM micrograph of CIGSS layer obtained at optimal conditions is shown in Fig.3. SEM image showed large, well-faceted dense grain structure for recrystallization temperature $T_2\sim 520$ °C and grain size

to be about ~ 1-2.5 μm, i.e. comparable to the film thickness.

The optical properties of CIGSS thin films on glass substrate were studied by measuring both transmittance (T) and reflection (R) spectra. The optical band gap values E$_g$ were determined by extrapolating of the linear part of the spectral dependence $\alpha^2 \sim f (h\nu)$ to the photon energy axis according [8,9]. The E$_g$ value varied from 1.27 eV to 1.41eV depending on S/(S+Se) ratio in the CIGSS films (Table 1). Taking into account law Ga content (~ 2. at.%), it is obvious that the band gap value changing is mainly due to the ratio S/(S+Se) in the films.
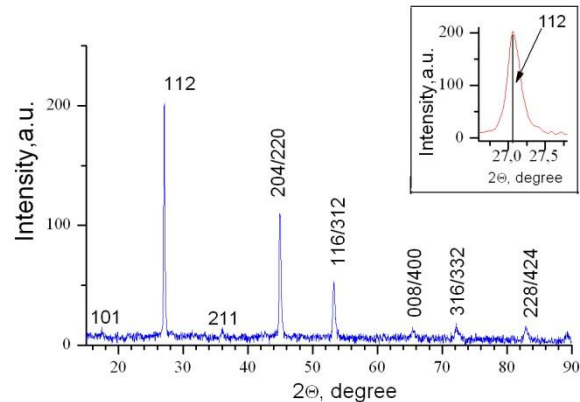
Fig. 1. XRD pattern of Cu$_{0,73}$In$_{1,18}$Ga$_{0,09}$S$_{0,87}$Se$_{1,13}$ thin film grown under 520 ^{0}C

3.2. The analysis of structure defects electrically activity.

For defects investigation were chosen the samples with more pronounced variation of S/(S+Se) ratio 0.39 (sample A1), 0.67 for sample A2 and 0.88 for A3. The area of the samples prepared for the studying was about 10×10 mm^2 and their thickness was approximately 2μm.

The ohmic contacts were deposited on the film surface with the use of silver paste. The distance between contacts was 5 mm. Quasi-monochromatic light excitation was chosen in compliance with the condition of maximal photosensitivity of the sample.

In the set of PICTS-spectrums there are two maximums which can correspond to emission from defects. The first one labeled as N_2 is observed in the temperature range of 260 − 300 K, whereas the second maximum labeled as N_1 is registered for temperatures

ranging from 160 to 220 K. The presence of these two maxima in the spectra is in a good agreement with the results obtained by admittance-spectroscopy and DLTS methods in the CIGS based solar cells [11-14]. The Arrhenius plots for the N_1 and N_2 maximums are presented in Fig. 4 and Fig. 5 correspondingly.
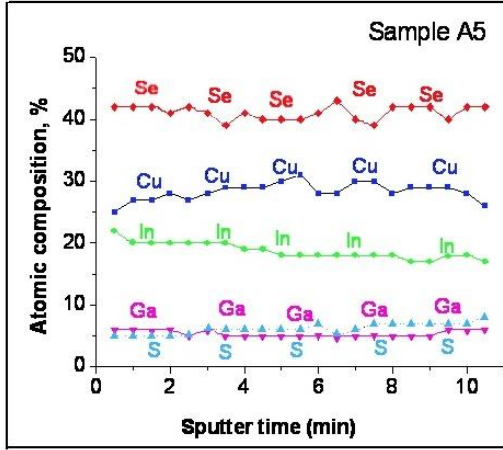
Fig. 2. AES profiles of CIGSS layer grown under 520 0C ((sample A5).
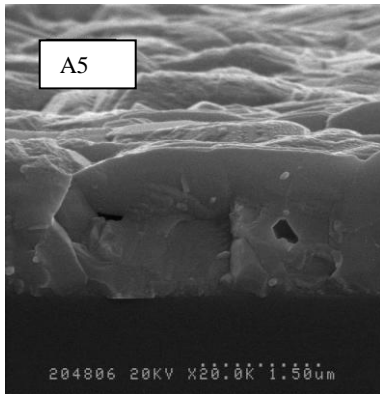
Fig. 3. SEM image of CIGSS thin film grown under 520 ^{0}C (sample A5).
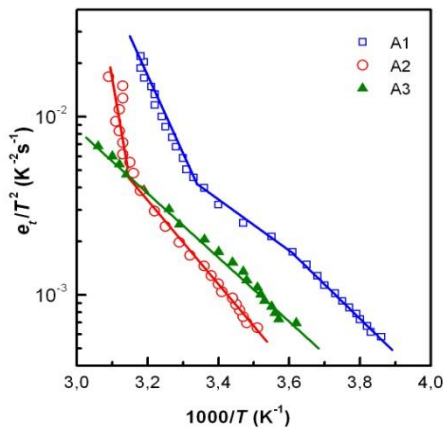
Fig. 4. Arrhenius plot of emission rates for the N_1 for set of samples.

Some distortion was demonstrated in the Arrhenius plot. This is the observation of the inflection points of a straight line. These peculiarities are more pronounced for A1 sample with less resistivity and presuppose the presence of several mechanisms of photocurrent decay with different temperature dependences of the characteristic relaxation times.

The observed peculiarities of the Arrhenius plot for A1 sample (Fig. 5) is in a good agreement with thermal dependencies of photoconductivity relaxation that was predicted by the theory offered for photoconductivity in silicon with presences of metastable thermal donors [15]. The peculiarities can also correspond to Lany-Zunger (LZ) model of intrinsic metastable defects of $Cu(In,Ga)Se_2$ (CIGS) which is derived from first principles calculations [16]. LZ model can explain the main features of CIGS including the persistent photoconductivity of CIGS films and the observed reversible changes of electrical characteristics of a solar cell under light soaking that is reported for CIGSS cell too [17].
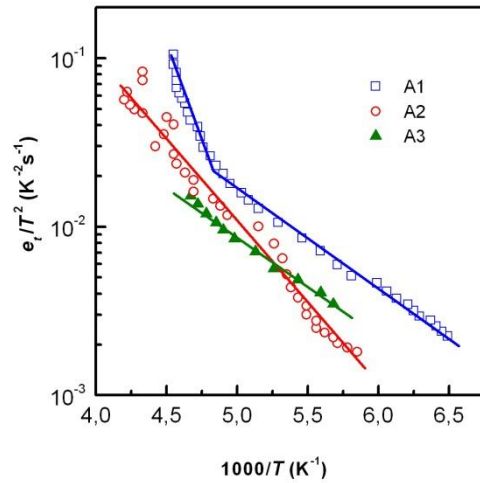
Fig. 5. Arrhenius plot of emission rates for the N_2 for set of samples.

Taking into account isovalent substitution Se→S in $Cu(In_xGa_{1-x})(Se_{1-y}S_y)_2$ solid solution thin films and their structural ordering, confirmed by XRD analysis, LZ model can be fully applied to our CIGSS films.

Moreover, were not observed any additional electrically active defects with variation of S/(S+Se) ratio in samples that is good agreements with the isovalent Se→S substitution behaviour. Thus the observed peculiarities of the defect recharging in $Cu(In_xGa_{1-x})(Se_{1-y}S_y)_2$ solid solution thin films probably is connected with the metastable nature of intrinsic defect as offered in LZ model.

The persistent photoconductivity reported on CIGS films demonstrates a decrease in the temperature region of 200 - 330 K [18] that includes the temperatures of recharging N_1 and N_2.

For more details we have carried out measurements of the temperature dependence of the "stationary" photoresponse under the same experimental conditions as in PICTS investigation. As the "stationary" photoresponse we used the difference of a signal that was sampled just at the moments that preceded light excitation switching. The results of the measurements obtained under different
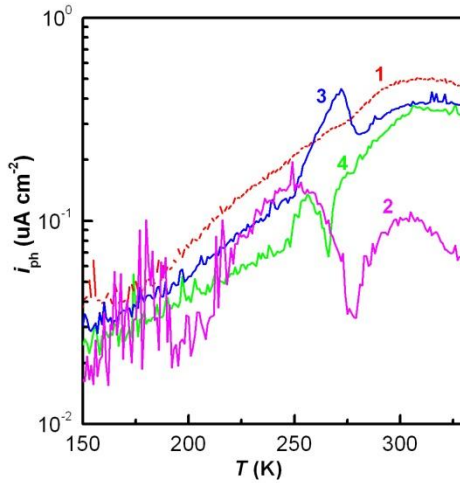
Fig. 6. The temperature dependence of photoresponse magnitude under repetitive excitation in the conditions of PICTS investigation.

initial conditions are presented in Fig. 6.

One can see from Fig.6 that a significant change of the temperature dependences trend with variation of the initial conditions of measurement was observed in a relatively narrow temperature region of 250 - 280K.

Curve 1 in Fg.6 corresponds initially to the relaxing state of A1 sample. Curve 2 was obtained after preliminary light soaking during one hour. Curves 3 and 4 are the result of measurement repetition without intermediate sample heating and with application of preliminary light soaking with duration t_1, t_2. Curve 3 corresponds to decrea of light soaking time (t_1 =50 min,

t_2 = 20 min). Curve 4 corresponds to an increase of light soaking time (t_1 =10 min, t_2 = 50 min).

It is only a part of temperature range T = 255 - 317 K where the recharging N_2 was registered by the PICTS.

4. CONCLUSION

Single-phase CIGSS thin films with [112] preferred orientation and uniform elements distribution through the depth of the film were grown by two-step annealing in S/Se ambient of sequentially deposited Cu, Ga and In precursors. The E_g value varied in CIGSS films from 1.27 eV to 1.41eV depending on S/(S+Se) ratio.

The defects recharge in the temperature region of 150-220K and 260 - 320K was found by PICTS technique, which is comparable with DLTS investigation of completed structures of a CIGS solar cell.

The change of activation energy of the defect recharging, depending on temperature indicates the involvement of several mechanisms in the process of charge and can be attributed to the metastable character of the defect

Comparability of temperatures of defect recharging and changes of photosensitivity of the film, and the presence of inflection points at the temperature dependences of recharging rate determines a metastable character of the defect, and can be interpreted in the framework of Lany-Zunger model of the native metastable defect of CIGS.

_____

[1] *K. Ramanathan, M.A. Contreras, C.L. Perkins, S. Asher, F.S. Hasoon, J. Keane, D.L. Young, M. Romero, W. Metzger, R. Noafi, J. Ward, A. Dauda,* Prog. Photovolt. Res. Appl. 11 (2003) 225.

[2] *M.A. Contreras, K. Ramanathan, J. AbuShama, F.S. Hasoon, D. L. Young, B. Egaas, R. Noafi*, Prog. Photovolt. Res. Appl. 13 (2005) 209.

[3] *M. Nouiri, Z. Ben Ayadi, K. Khirouni et all*, Materials Science and Engineering C 27 (2007) 1002.

[4] *Ch. Hurter, M. Boilou, A. Mitonneau, D. Bois*, Appl. Phys. Lett. 32 (1978) 821.

[5] *O. Yoshie, M. Kamihara.* Jpn. J. Appl. Phys. 22 (1983) 621.

[6] *Odrinski, V. Gremenok, E. Zaretskaya et all*, J. of Mat. Science: Materials in Electronics 19 (2008) 371.

[7] *E. Zaretskaya, V. Gremenok, V. Zalesski et all,* Phys. Status Solidi. (c) 6 (2009) 1278.

[8] *D.K. Schroder*, Semiconductor Material and Device Characterisation, Wiley, New York, 1990.

[9] *J.I. Pankove*, Optical Processes in Semiconductors, Prentice Hall, Englewood, New York, 1971.

[10] *I.A. Davydov, A.P. Odrinski.* Electronics (*in Russian*) 11 (1990) 4.

[11] *T. Walter, R. Herberholtz, C. Muler, H.- W. Schock.* J Appl. Phys. 80 (1996) 4411.

[12] *L.L. Kerr, Sheng S. Li, S.W. Johnston et all,* Solid-State Electronics 48 (2004) 1579.

[13] *M. Igalson, C. Platzer-Bjorkman.* Solar Energy Materials &Solar Cells 84 (2004) 93.

[14] *M. Turcu, I.M. Kötschau, U. Rau*. J. Appl. Phys. A 73 (2001) 769.

[15] *L.F. Makarenko, L.I. Murin*, Phys. Status Solidi B 145 (1988) 241.

[16] *S. Lany, A. Zunger*. J. Appl. Phys. 100, (2006) 113725.

[17] *C. Deibel, V. Dyakonov, and J. Parisi.* Zeitschrift für Naturforschung A Vol. 58a (2003) 691.

[18] *M. Cwil et all.*, J Appl. Phys. 103 (2008) 063701.

SPACE CONSTRUCTION AND MOLECULAR DYNAMICS OF BLAST 1 MOLECULE OF ALLOSTATIN FAMILY IN AQUEOUS MEDIUM

L.I. VELIYEVA, I.N. ALIYEVA, E.Z. ALIYEV

Baku State University
Lala_Veliyeva@rambler.ru

The space construction, conformation properties and molecule mobility in mediums modeling the water surroundings, have been studied on the base of investigation of intramolecular interactions and quantitative estimation of change limit of two-faced angles in main and side chains of amino acid residues forming the structure of neuropeptide BLAST 1 of allatostatin family. It is seen that fragments Leu1-Phe4 and Phe4-Leu6 stabilized by non-valent and electrostatic atom interactions, save their structure in the molecular dynamic process at the presence of given water molecules.

INTRODUCTION

The neuropeptides of allatostatin family having the unique ability to regular the synthesis processes and juvenile hormones of insect different types are related to number of objects of intensive investigation of last decade [1-4]. The structure and conformation properties of the one of the given family representatives is BLAST 1containing six amino acid residues in its primary structure: Leu1-Tyr2-Asp3-Phe4-Gly5-Leu6-NH2 have been investigated in detail in this work by theoretic modeling methods.

CALCULATION METHOD

The low-energy conformation states of BLAST 1 are established by the way of minimization of total conformation energy in force field of atom-atom potential functions. At energy calculation the non-valent (E_{nv}) and electrostatic (E_{es}) atom interactions, hydrogen bonds (E_{hyd}) and torsion contributions (E_{tors}) for descriptions of which the semiempirical potential functions proposed in works [5,6] are used. The calculations are carried out in the limits of hard valent scheme, i.e. at fixed values of valent bond lengths and valent angles of amino acid residues being in chemical structure of BLAST 1. The applied system of applied functions and calculated program are approbated on big number peptides and proteins by given work authors and other investigators [7-10].

For water surrounding modeling the parameterization proposed in works [5,6,11] is used. The hydrogen bond energy is estimated with the help of Morse potential at value of hydrogen bond dissociation energy equal to 1,5 kcal/mol corresponding to bond distance NH…OC r=1.8Å for water solutions. The dielectric constant value is equal to 10 [11]. At discussion of calculation results the generally accepted peptide structure classification is used [5]. The choice of structural variants at calculation of separate peptide conformation is used on the base of known values of two-faced angles (φ and ψ) corresponding to low-energy regions of conformation map R, B, L and P for each single peptide. The calculation of two-faced angles is carried out according to international nomenclature [12].

For study of conformation mobility of BLAST the molecular dynamics method described in works [13-15] is used. The classic atom paths of motion of macromolecule are calculated in method using the force field of atom-atom potential, i.e. the detail microscopic picture of molecule internal thermal mobility in sub-nano-second time intervals. At calculation carrying out the demonstration version of Hyper.chem program which is accessible on Hypercube site (http://www.hyper.com/) [16]. For calculation acceleration of Van-der-Waals, hydrogen and electrostatic interactions the cutting radius 12 Å is used. In order to escape the undesirable edge effects the peptide chain is added by acetyl residues in the chain beginning and by N-methylamine in the end of it. The search of low-energy conformations of molecular system is carried out with the help of numerical search methods of many variables of function extrema. Moreover, it is supposed that molecule native conformation is in global minimum region of potential energy.

RESULTS AND DISCUSSION
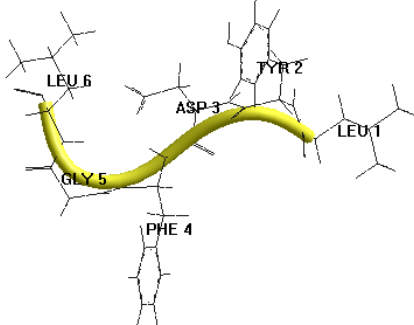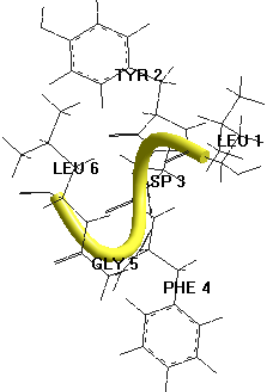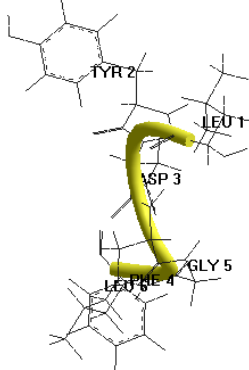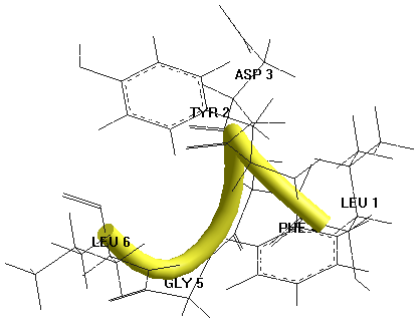
The six amino acid residues Leu1-Tyr2-Asp3-Phe4-Gly5-Leu6-NH2 (LYDFGL) are in chemical structure of neuropeptide BLAST 1. The molecule conformation investigation is carried out on the base of fragmentary approach used in conformation analysis method [5]. The beginning structural variants for stable conformation calculation of separate fragments are formed with taking under consideration the different positions of side chains of amino acid residues thus that to consider the maximal quantity of inter-residual interactions stabilizing the structure. The data obtained for C-edge fragment Phe-Gly-Leu are also used in previous investigations by authors [8,9]. In molecular dynamics method molecule BLAST 1 surrounded by 117 water molecules with taking under consideration the periodic boundary conditions, is put in hypothetic box with sizes 17.09Åx10.64x19.47Å [15].

The calculation of low-energy conformation states of separate fragments and their overlapping regions allow us to reveal the neuropeptide stable states which are given in table 1. According to investigation results, 59 conformations the total energy of which varies in the limit of values from 5,85 up to 13,99 kcal /mol are in interval with relative energy 0-10 kcal/mol. The conformation state with energy minimal value equal to 13,99 kcal /mol

is the most preferable both interactions the non-valent and torsion ones by contribution (table 1). The conformation states of most 4 stable structures constructed on the base of calculated values of two-faced angles are also given in table 1. All them are stabilized by both non-valent and electrostatic atom interactions in the limit of two regions.

Table 1

The low-energy conformation states of BLAST 1 molecule of allatostatin family

Conformation	Energy contributions Kcal/mol				
	E_{nonv}	E_{el}	E_{tors}	E_{tot}	E_{rel}
	-23.00	5.95	3.06	-13.99	0.00
	-21.87	5.25	3.14	-13.48	0.51
	-21.95	5.63	3.17	-13.15	0.84
	-20.83	5.42	3.48	-11.93	2.06

With the aim of study of water molecule influence on neuropeptide conformation mobility, the molecular dynamics of allatostatin BLAST1 is investigated. The molecular-dynamic modeling for conformation with minimal value of total energy is carried out under periodic boundary conditions in hypothetic cubic volume with sizes 17.09Åx10.64x19.47Å containing 117 water molecules (fig.1). In the calculation beginning the molecule relaxation with use of force field AM1 during 30ps is carried out. The found energy minimum allows us

to put the molecule in the volume containing 117 water molecules. Further the molecule relaxation with taking under consideration the real water surrounding of molecules is carried out. For imitation of water surrounding the atom collision rate with water molecules is 50ps^{-1}.

According to calculation results the fragments Leu1-Phe4 and Phe4-Leu6 save the folded character of peptide chain before and up to optimization. The distance between между C$^\alpha$-atoms of residues of first and fifth residues in the given orders varies in limit 4.8-6.3 Å, and hydrogen bond between CO and NH-groups of peptide chain doesn't destroy in molecular dynamics process, in spite of the changes in neuropeptide intramolecular energy on 5-20 kcal/mol.
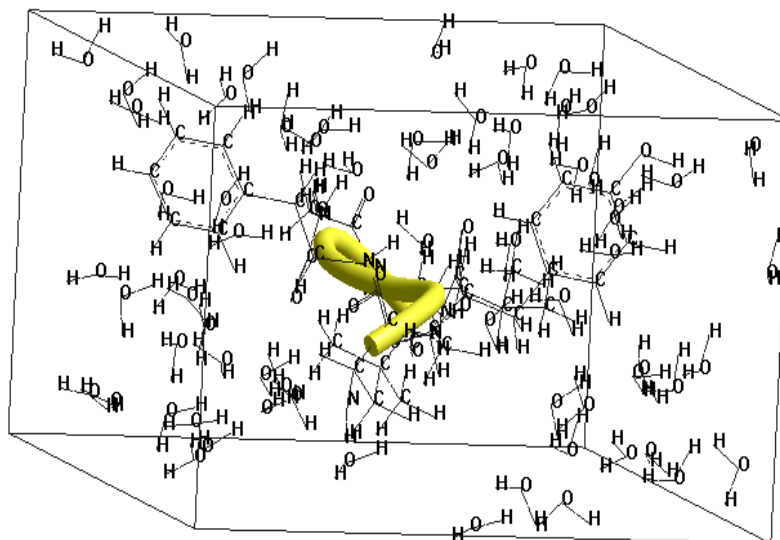
Fig.1. The optimized structure of allatostatin molecule Dippu AST2 in conditions of obviously given water surrounding

The structure stability of separate fragments also proves the two-faced angle values in molecule main chain the change limits of which are given in table 2.

Table 2

The change limit of two-faced angles of main chain in the molecular dynamics process (MD) of BLAST1 molecule

Residue	Angle, degree	E$_{rel}$=0.0 kcal/mol			Residue	Angle	E$_{rel}$=0.51kcal/mol		
		Before optimization	After optimization	MD			Before optimization	After optimization	MD
Ala1	φ	-98	-87		Ala1	φ	-103	-100	-99
	ψ	-53	-64	-72		ψ	-53	-45	-42
	ω	180	181	179		ω	181	-171	-177
Tyr2	φ	-85	-89	-88	Tyr2	φ	-86	-91	-102
	ψ	64	75	67		ψ	65	75	60
	ω	175	174	181		ω	-185	178	184
Asp3	φ	-95	-87	-90	Asp3	φ	-87	-79	-89
	ψ	61	-57	-51		ψ	54	36	60
	ω	176	-178	179		ω	186	179	183
Phe4	φ	-141	-136	-150	Phe4	φ	-100	-93	-81
	ψ	-61	-78	-65		ψ	181	177	183
	ω	172	173	179		ω	180	-172	-186
Gly5	φ	-98	-80	-85	Gly5	φ	80	67	56
	ψ	44	56	60		ψ	-59	-57	-63
	ω	177	182	179		ω	184	186	179
Leu6	φ	-122	-125	-119	Leu6	φ	-94	-81	-89
	ψ	-55	-42	-50		ψ	-53	-64	-58
	ω	181	180	179		ω	173	172	175

The obtained data allows us to conclude that neuropeptide BLAST1 contains the stable elements of space structure which can be responsible for conformation formations which are necessary for connecting with allatostatin receptors. The results can be useful at investigation of allatostatin action mechanism and formation of new, more effective analogues of neuropeptides of this family.

_____

[1] *X. Belles, J.L. Maestro et al.* Allatostatic neuropeptide from the Cockroach Blatella-Germanica (L) (Dictyoptera, Blatellidae) – Identification, Immunolocalization and activity // Regul.Peptides.,1994, v.53(3), p.237-247

[2] *G. Gäde, J.G. Graham.* Insect peptide hormones: a selective review of their physiology and potential application for pest control // Pest. Mang.Sci., 2003, v.59, p.1063-1075

[3] *G. Gäde , H.G. Marco, D. Richter , R.J. Weaver.* Structure-activity studies with endogenous allatostatins from Periplaneta americana: expressed receptor compared with functional bioassay // J Insect. Physiol., 2008, v.54(6), p.988-996

[4] *Z.P. Kai, J. Huang, Y. Xie, S.S. Tobe, Y. Ling, L. Zhang, Y.C. Zhao, X.L. Yang.* Synthesis, biological activity, and hologram quantitative structure-activity relationships of novel allatostatin analogues // J.Agric.Food Chem., 2010, v.58(5), p.2652-2658

[5] *E.M. Popov.* Quantitative approach to conformations of proteins Int.J.Quant.Chem., 1979, v. 16, p. 707-737

[6] *F.A. Momany, R. McGuire, A.W. Burgess, H.A. Scheraga.* Energy parameters in polypeptides: geometric parameters, partial atomic charges, nonbonded interaction for naturally occurring amino acid // J.Phys.Chem., 1975, v.79, p. 2361-2381

[7] *I.N. Alieva, L.I. Veliyeva, M.A. Musayev, N.M. Gojayev*. Conformational features of the allatostatin III neuropeptide from the cockroach *Diploptera Punctata* // Protein and Peptide Letters, 2006, v.13, p.1007-1015

[8] *M.A. Musaev, M.A. Velieva, L.I. Alieva, N.M. Qodjaev.* Prostranstvennaya struktura neyropeptida allastatina-4 // Vestnik Bakinskoqo Universiteta, seriya fiz-mat. nauk, 2005, №2, s.167-178. (in Russian)

[9] *L.I. Velieva, M.A. Musaev, I.N. Alieva, N.M. Qodjaev.* Molekulyarnaya dinamika neyropeptidov semeystva allatostatinov // Vestnik Bakinskoqo Universiteta, seriya fiz-mat. nauk,2006, №1, c.120-131. (in Russian)

[10] *I.N. Alieva, N.N. Mustafaeva, N.M. Gojayev.* Conformational analysis of the N-terminal sequence Met1-Val60 of the tyrosine hydroxylase //Journal of Molecular Structure ("Elsevier Science" UK), 2006, v.785, iss. 1-3, p.76-84

[11] *Q.M. Lipkind, S.F. Arxipova, E.M. Popov.* Teoreticeskoe issledovanie konformatsii N-achetil L-alanina v razlichnikh sredakh // Jurnal struk.khimii, 1970, t.11, s.121-126. (in Russian)

[12] IUPAC-IUB Quantity, Units and Symbols in Physical Chemistry, Blackwell Scientific Publications, Oxford, 1988, p.39

[13] *E.E. Shnol, A.Q. Qrivchov u ∂p.* Method molekularnoi dinamiki v fizicheskoi khimii, M. Nauka, 1996, 334 c. (in Russian)

[14] *K.V. Shaytan.* Enerqeticheskaya poverxnost I konformachionnaya dinamika molekul // Elektrokhimiya, 2003, t.39(2), s.212-219. (in Russian)

[15] *K.V. Shaytan, S.S. Saraykin.* Metod molekulyarnoy dinamiki, 1999, http://www.moldyn.ru/library/md/default.htm www.hyper.com (in Russian)

Resevied:02.02.2012

DFT STUDY ON VIBRATIONAL SPECTRA OF 4-CYCLOHEXYLPIPERIDINE

GÜRKAN KEŞAN [1], METIN BILGE [2], CEMAL PARLAK [3] AND ÖZGÜR ALVER [4]

[1] *Faculty of Science, Institute of Physical Biology, University of South Bohemia, Branišovská 31,*
370 05 České Budějovice, Czech Republic
[2] *Department of Physics, Science Faculty, Ege University, İzmir, 35100, Turkey*
[3] *Department of Physics, Dumlupınar University, Kütahya, 43100, Turkey*
[4] *Department of Physics, Science Faculty, Anadolu University, Eskişehir, 26470, Turkey*
E-mail: cparlak20@gmail.com, Tel.: +90 (274) 265 20 51 / 3116, Fax: +90 (274) 265 20 56

The optimized structural parameters (bond lengths, bond and dihedral angles), conformational equilibrium and vibrational spectra together with assignments of 4-cyclohexylpiperidine (4-cypp) have been examined by means of B3LYP hybrid density functional theory (DFT) method with 6-31G(d) basis set. Furthermore, reliable vibrational assignments have made on the basis of potential energy distribution (PED) calculated. Calculations are employed for different conformations of 4-cypp ($C_{11}H_{21}N$), both in gas phase and in solution. Solvent effects are investigated using chloroform and dimethylsulfoxide. Results from the theoretical values are showed that the structural parameters, mole fractions of stable conformers, vibrational frequencies and assignments, IR intensities and Raman activities of 4-cypp are solvent dependent.

1. INTRODUCTION

Theoretical investigations of vibrational spectra are generally conducted with an isolated molecule in the gas phase; however, the experimental studies most often involve molecules in solution, so there is a need to account for solvent effects in theoretical approaches. Vibrational spectroscopy has been widely used as a standard tool for structural characterization of molecular systems by DFT calculations [1, 2] which exhibit excellent performance on electron affinities, bond energies, vibrational frequencies and geometries of the system [1-5]. The effects of solvent on the vibrational spectra can be successfully explained by the environmental factors that affect the vibrational frequency, intensity and band shape [6].

The 4-cyclohexylpiperidine molecule consists of piperidine ($C_5H_{11}N$), which is a heterocyclic amine and a six-membered ring containing five methylene units and one nitrogen atom, attached to the carbon of cyclohexane (C_6H_{12}), which is a cycloalkane and six membered single bonded carbon rings. Piperidine has two distinguishable chair conformations; one with N–H bond in the axial position, and the other in the equatorial position. After much controversy during the 1950s–1970s, the equatorial conformation was found to be more stable by 0.72 kcal/mol in the gas phase [7, 8]. In non-polar solvents, the same situation has been estimated with a range between 0.2 and 0.6 kcal/mol, but in polar solvents the axial conformer may be more stable [7-10]. Substituents on a piperidine ring have been found in the equatorial position [7]. Cyclohexane can exist in the chair, half-chair or envelope, twist or twist-boat and boat conformers, but it is found in the chair form 99.99 %. If cyclohexane is mono-substituted with a large substituent, then the substituent will most likely be found attached in the equatorial position [11]. According to the above explanations, many possible conformers could be proposed for 4-cypp, but here the discussion has confined for e-e, e-a, a-a and a-e conformers of 4-cypp (Figure 1). In these presentations, the former represents cyclohexane while the latter stands for NH group. They are considered in axial and equatorial positions according to plane formed by C19, C20, C22 and C25 carbon atoms of 4-cypp.
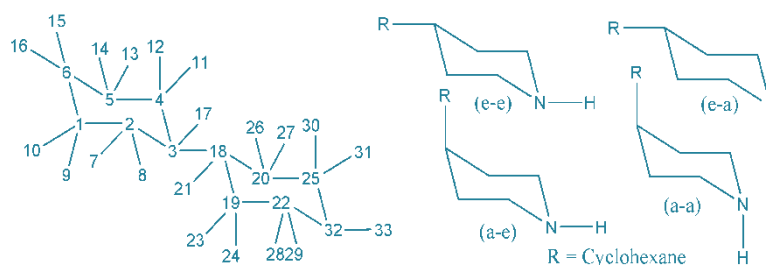
Fig. 1. Conformations of 4-cypp showing atomic numbering.

This molecule is a piperidine derivative and very important intermediate compound for drug design in the pharmaceutical industry [12-14]. Even though, 4-cypp has wide applications in drug science, to the best of our knowledge, there is no detailed information present in the literature about its molecular structure and spectroscopic properties. The essence of this study is briefly to report theoretical vibrational features of 4-cypp and then to investigate solvent effects on vibrational spectra of 4-cypp using chloroform and dimethylsulfoxide. Solvent

effects are a pivotal tool for drug design in the pharmaceutical industry because they affect the release, transport and degree of absorption of the drug in the organism, which is important for future development and formulation efforts of the drug. Furthermore, the presented data as theoretically may be helpful in context of the further studies of 4-cypp. For the above goals, we have examined the optimized parameters, conformational equilibria and vibrational spectra together with PED calculations for the most stable two conformers of 4-cypp in solution and gas phase by means of B3LYP/6-31G(d) level.

2. CALCULATION

All calculations were carried out with Gaussian 09.A1 software package [15] on a personal computer having linux operating system. All four forms of 4-cypp were first optimized in the gas phase and with different solvents (chloroform and dimethylsulfoxide) at B3LYP level of theory using 6-31G(d) basis set. e-e and e-a conformations were found more stable than the other two forms. Therefore, the vibrational frequencies for e-e and e-a forms of 4-cypp were calculated at the same method and basis set and then scaled by 0.955 (above 1800 cm^{-1}) and 0.967 (under 1800 cm^{-1}) [3, 4]. The polarizable continuum model (PCM), which is the default in Gaussian 09.A1, was used for the geometries, free energies and vibrational frequencies. The absence of imaginary frequencies confirmed that the optimized structure is a local minimum. GaussSum 2.2.5 [16] program was used for visualization of the structure and simulated vibrational spectra.

PED calculations; which show the relative contributions of the redundant internal coordinates to each normal vibrational mode of the molecule and thus make it possible to describe the character of each mode numerically; were carried out by the Gar2ped program
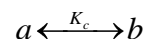
[17] using the output files (as arch and log) created at the end of the frequencies calculations.

The mole fractions of individual conformers were calculated with the following equations:

$$a \xleftarrow{\;\;K_c\;\;} b$$

According to equilibrium given above,

$$K_c = N_a/N_b \;\; \text{and} \;\; N_a + N_b = 1$$

can be written, where K_c is conformational equilibrium constant between a and b forms, N_a and N_b are mole fractions of conformers a and b. $N_a = 1/1+K_c$, $N_b = K_c/1+K_c$, $K_c = e^{-\delta\Delta G/RT}$, $R = 1.987 \times 10^{-3} \, kcal/mol \, ^oK$, $T = 298 \, ^oK$ and $\delta\Delta G = \Delta G_b - \Delta G_a$.

3. RESULTS AND DISCUSSION

The results of the calculations on the molecular conformations and geometrical parameters of 4-cypp are discussed first. A brief discussion of the vibrational frequencies, infrared intensities and Raman activities together with the solvent effect is then presented.

3.1. GEOMETRICAL STRUCTURES

To study the vibrational frequencies, it is essential to examine the geometry of any compound as small changes in geometry can potentially cause substantial changes in frequencies. Although the solute-solvent interactions are less crucial than the intramolecular forces, the geometry of the solute undergoes important changes in going from gas phase to solution.

Table 1.

Some features in various medium of different conformations of 4-cypp.

Medium / Feature	B3LYP/6-31G(d)	
	e-e	e-a
Gas Phase		
Molar volume (cm^3/mol)	141.780	159.435
Recommend a$_0$ (Å)	4.72	4.88
ΔG (Hartree)	-486.305543	-486.305136
Relative stability (δΔG;kcal/mol)	0.000	0.255
Equilibrium constant (K$_c$)	0.65	
Mole fractions (%)	61	39
Chloroform (ε=4.9)		
ΔG (Hartree)	-486.310451	-486.310411
Relative stability (δΔG;kcal/mol)	0.000	0.025
Equilibrium constant (K$_c$)	0.96	
Mole fractions (%)	51	49
Dimethylsulfoxide (ε=46.7)		
ΔG (Hartree)	-486.312668	-486.312924
Relative stability (δΔG;kcal/mol)	0.161	0.000
Equilibrium constant (K$_c$)	0.76	
Mole fractions (%)	43	57

Gibbs free energies, relative stabilities, equilibrium constants and mole fractions of the optimized geometries in the three different environments of two conformations of 4-cypp calculated with B3LYP/6-31G(d) are given in Table 1. Regarding all the calculated free energies, the a-e and a-a forms could be neglected for calculation of equilibrium constant since their energy differences are larger than 2 kcal/mol. For gas phase, e-e form is more stable than other forms and the structure prefers e-e and e-a forms with preference of 61 % and 39 %, respectively.

Similarly, the calculated free energies in chloroform as a non-polar solvent show that e-e form is more stable than other forms and 4-cypp prefers e-e and e-a forms with preference of 51 % and 49 %, respectively. However, the calculated free energies in dimethylsulfoxide as polar solvent show that the e-a form is more stable than the other forms and 4-cypp prefers e-a and e-e forms with approximate preference of 57 % and 43 %, respectively.

Table 2.
Optimized bond lengths (Å) for two forms of 4-cypp in various medium.

Bond Lenghts (Å)	Gas Phase		Choloroform		Dmso	
	e − e	e − a	e − e	e − a	e − e	e − a
R (1,2)	1.537	1.537	1.538	1.538	1.538	1.538
R (1,6)	1.533	1.533	1.534	1.534	1.534	1.534
R (4,5)	1.537	1.537	1.538	1.538	1.538	1.538
R (5,6)	1.533	1.533	1.534	1.534	1.534	1.534
R (2,3)	1.545	1.545	1.545	1.545	1.545	1.545
R (3,4)	1.545	1.545	1.545	1.545	1.545	1.545
R (3,18)	1.553	1.554	1.553	1.554	1.553	1.554
R (C-H), cy	1.100	1.100	1.100	1.100	1.100	1.100
R (C-H), pp	1.100	1.100	1.100	1.100	1.100	1.100
R (18,19)	1.545	1.545	1.545	1.544	1.544	1.544
R (18,20)	1.545	1.545	1.545	1.544	1.545	1.544
R (20,25)	1.532	1.540	1.532	1.539	1.532	1.539
R (19,22)	1.532	1.540	1.532	1.539	1.532	1.539
R (25,32)	1.462	1.465	1.465	1.468	1.466	1.469
R (22,32)	1.462	1.465	1.465	1.468	1.466	1.469
R (32,33)	1.018	1.021	1.023	1.025	1.025	1.028

Table 3.
Optimized bond and dihedral angles (°) for two forms of 4-cypp in various medium.

Bond Angles (°)	Gas Phase		Choloroform		Dmso	
	e − e	e − a	e − e	e − a	e − e	e − a
A (22,32,25)	111.2	111.0	110.8	110.7	110.6	110.6
A (18,19,22)	112.1	112.1	112.1	112.2	112.1	112.2
A (18,20,25)	112.1	112.1	112.1	112.2	112.1	112.2
A (19,18,20)	108.7	108.7	108.6	108.6	108.6	108.5
A (19,22,32)	110.0	114.7	110.2	114.6	110.3	114.6
A (20,25,32)	110.0	114.7	110.2	114.6	110.3	114.6
< H–C–H, pp	107.0	107.0	107.0	107.0	107.0	107.0
A (25,32,33)	109.8	108.7	109.3	108.3	109.1	108.1
A (22,32,33)	109.8	108.7	109.3	108.3	109.1	108.1
A (3,18,19)	112.8	112.9	112.8	112.8	112.9	112.8
A (3,18,20)	112.8	112.9	112.8	112.9	112.7	112.8
A (2,3,18)	112.4	112.5	112.4	112.4	112.5	112.4
A (4,3,18)	112.4	112.5	112.4	112.5	112.2	112.4
A (2,3,4)	109.4	109.4	109.4	109.3	109.3	109.3
A (1,2,3)	112.9	112.9	112.9	112.9	112.9	112.9
A (3,4,5)	112.9	112.9	112.9	112.9	112.9	112.9
A (4,5,6)	111.8	111.8	111.8	111.8	111.8	111.8
A (2,1,6)	111.8	111.8	111.8	111.8	111.8	111.8
< H–C–H, cy	107.0	107.0	107.0	107.0	107.0	107.0
A (17,3,18)	107.3	107.2	107.3	107.3	107.4	107.3
A (4,3,17)	107.5	107.5	107.6	107.5	107.6	107.6
A (2,3,17)	107.5	107.5	107.6	107.5	107.5	107.6

A (3,18,21)	107.4	107.3	107.4	107.4	107.4	107.4
A (20,18,21)	107.4	107.4	107.4	107.5	107.5	107.5
A (19,18,21)	107.5	107.4	107.4	107.5	107.4	107.5
Dihedral Angles (^{o})	e − e	e − a	e − e	e − a	e − e	e − a
D (18,20,25,32)	57.0	53.9	57.2	54.1	57.2	54.3
D (18,19,22,32)	-57.0	-53.9	-57.2	-54.2	-57.2	-54.3
D (3,4,5,6)	55.3	55.3	55.3	55.4	55.3	55.4
D (6,1,2,3)	-55.3	-55.3	-55.3	-55.4	-55.4	-55.4
D (4,3,18,19)	-179.8	-179.8	-179.7	-179.6	178.5	-179.8
D (2,3,18,19)	56.2	56.1	56.4	56.4	54.6	56.3
D (19,22,32,33)	-176.4	-67.0	-177.7	-65.8	-178.3	-65.3
D (20,25,32,33)	176.4	67.0	177.7	65.9	178.3	65.3
D (4,3,18,20)	-56.2	-56.1	-56.1	-56.1	-57.9	-56.4
D (2,3,18,20)	179.9	179.8	180.0	180.0	176.2	176.7
D (18,3,4,5)	-179.0	-179.1	-178.9	-179.1	-179.1	-179.1
D (1,2,3,18)	179.0	179.1	179.0	179.1	178.9	179.1
D (3,18,20,25)	-177.2	-177.4	-177.3	-177.3	-177.3	-177.3
D (3,18,19,22)	177.2	177.4	177.3	177.4	177.1	177.3

To the best of our knowledge, experimental data on the geometric structure of 4-cypp is not available in the literature. The optimized geometric parameters (bond lengths, bond and dihedral angles) calculated by B3LYP/6-31G(d) are listed in Tables 2-3. As it can be seen from Tables 2-3, there is no considerable differences in bond lengths or angles and, if we compare these data, the correlation values of bond lengths for e-e form between the gas phase and solution are found to be 0.99995 for chloroform and 0.99990 for dmso. Similarly, the correlation values of bond angles for e-e form between the gas phase and solution are found to be 0.99386 for chloroform and 0.98707 for dmso. However, as it can be seen from Table 3, there are some changes in going from gas phase to solution in dihedral angles. The correlation values of dihedral angles for e-e form between the gas phase and solution are found to be 0.60244 for chloroform and 0.60455 for dmso. The magnitude of dihedral angles, D(19;22;32;33) and D(3;18;19;22), for the optimized 4-cypp in the e-e form are found to be as about -177° and 177° while these angles are found as about -66° and 177° for the e-a form of 4-cypp.

3.2. VIBRATIONAL STUDIES OF 4-CYPP

To the best of our knowledge, experimental study on the vibrational spectra of 4-cypp is not available in the literature. All calculated frequency values presented in this paper are obtained within the harmonic approximation which allows us to describe vibrational motion in terms of independent vibrational modes each of which is governed by a simple one dimensional harmonic potential. 4-cypp consists of 33 atoms, so it has 93 normal vibrational modes and it belongs to the point group C_1 with only identity (E) symmetry operation. According to the calculations, 11 normal vibrational modes of 4-cypp are below 400 cm^{-1} whereas 82 modes are between 4000 cm^{-1} and 400 cm^{-1}.

The theoretical vibrational frequencies and assignments of 4-cypp in gas phase together with their IR intensities and Raman activities are given in Table 4 and theoretical IR and Raman spectra of 4-cypp are shown in Figure 2. As the presence of dielectric medium has a strong influence on the vibrational frequencies, there are significant changes in presented theoretical vibrational values. Some important vibrational motions are described here, as following. The NH and CN bond lengths increase on going from the gas phase to the solvent phase. Hence, the NH and CN stretching frequencies should decrease. It is clearly observed that these requirements are fulfilled for 4-cypp. The v_1/NH stretching band of 4-cypp attributed to piperidine group has been calculated at 3336 cm^{-1} for e-e form in the gas phase. This mode are shifted to the lower frequencies as 91 cm^{-1} for e-e form in chloroform, 140 cm^{-1} for e-e form in dmso. These frequencies shifts are explained in terms of increased positive character on nitrogen in solvents of high dielectric constant. Similarly, the CN (v_{22}, v_{54}) stretching bands of 4-cypp decrease about 6 cm^{-1}. The CH and CH_2 asymmetric or symmetric stretching vibrations (v_2-v_{19}) arising from piperidine or cyclohexane groups of 4-cypp are also shifted to the lower frequencies when 4-cypp in solvated. The biggest difference between the calculated frequency values except for v_1 mode is 20 cm^{-1} for e-e form in going from gas phase to solution.

IR intensities are expected to dramatically change when the solute is solvated and this is indeed the case in our present study. The noticeable changes are shown in many modes and the calculated intensities in solutions are very high when compared to those in the gas phase. Like IR intensities, significant changes in Raman activities are seen when the molecule is solvated. For the IR intensities and Raman activities, the increases in dmso are larger than in chloroform.

4. CONCLUSION

The theoretical vibrational investigations of 4-cypp are successfully performed by using quantum chemical calculations. In conclusion, following results can be summarized: (1). For 4-cypp, e-e and e-a conformers are comparable in their energies. However, relative energies, of a-a and a-e forms are larger than 2.0 kcal/mol. Therefore, relative mole fractions of these forms could be neglected. (2). With less polar solvent such as CDCl$_3$, 4-cypp adopts mainly the e-e conformer. However, with increasing solvent polarity, the e-a conformer becomes more dominant. The conformational exchange is more

apparent with polar solvents which suggest that conformational energy barrier is solvent dependent. (3). Some significant changes are found in the dihedral angles but no noticeable changes appear in bond lengths or angles when 4-cypp in solvated. (4). There are very significant shifts in vibrational frequencies due to dielectric medium. In generally, the frequency differences increase when going from non-polar to polar solvents. (5). Solvent effects on infrared intensities and Raman scattering activities are quite considerable and they increase as one goes from lower to higher dielectric constant.
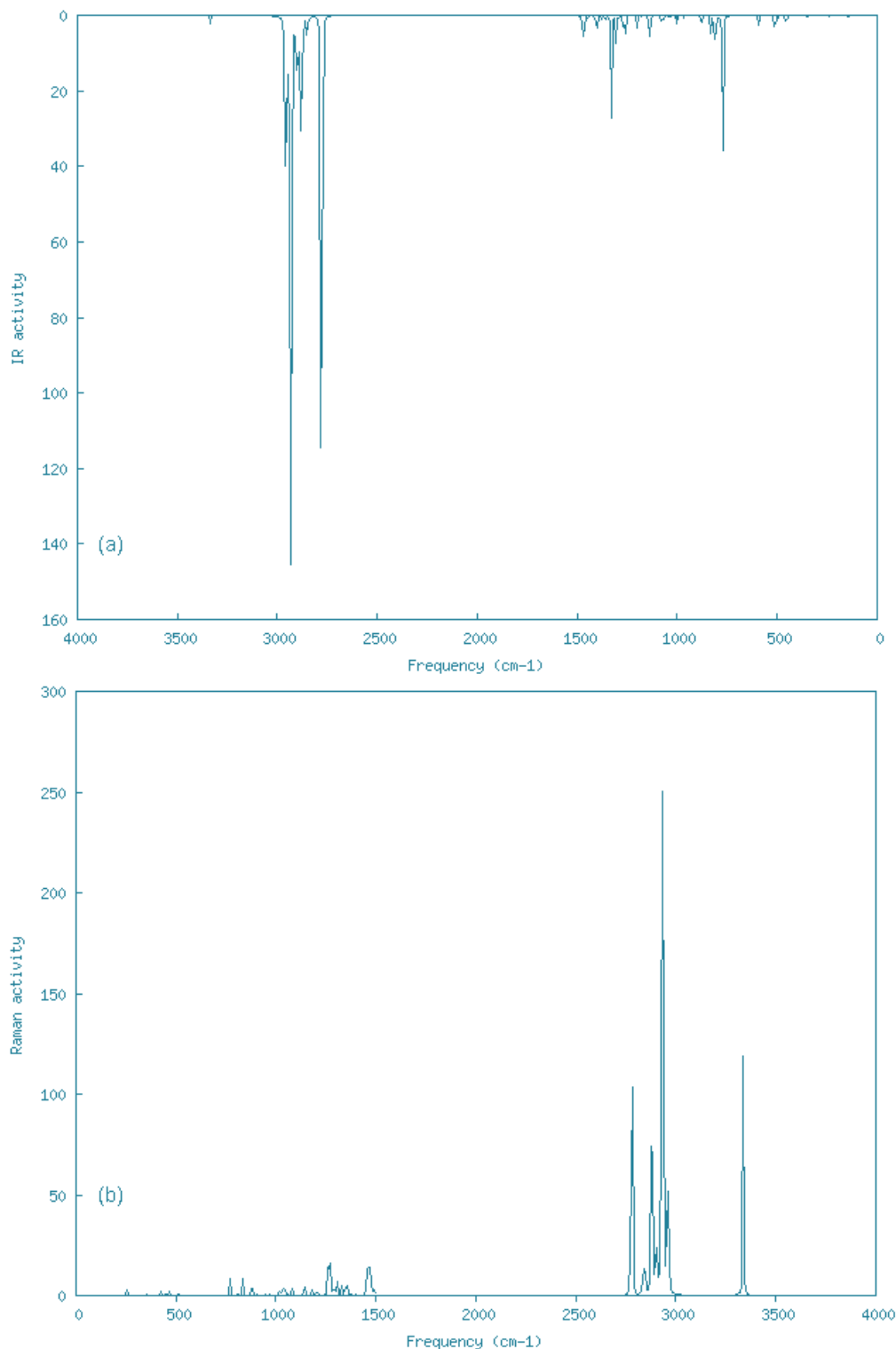

Fig. 2. Theoretical IR (a) and Raman (b) spectra for e-e form of 4-cypp in gas phase.

Table 4.

Calculated vibrational frequencies (cm^{-1}) for e-e form of 4-cypp in gas phase.

Mode	P.E.D ($\geq$ 5 %)	e-e form in gas phase–B3LYP/6-31G(d)			
		Unscaled Freq.	Scaled Freq. *	I_{IR}	A_R
ν_1	ν 32-33 (90)	3493	3336	3.56	188.73
ν_2	ν 20-27 (45) + ν 20-26 (22) + ν 4-12 (20) + ν 19-24 (9)	3100	2961	4.72	173.04
ν_3	ν 20-27 (46) + ν 4-12 (22) + ν 20-26 (19) + ν 19-24 (7)	3099	2960	82.29	2.99
ν_4	ν 4-12 (51) + ν 20-26 (22) + ν 20-27 (16)	3084	2945	103.70	28.70
ν_5	ν 4-12 (53) + ν 20-26 (19) + ν 20-27 (19)	3081	2942	7.70	81.44
ν_6	ν 25-30 (84) + ν 22-28 (6)	3074	2936	34.95	181.39
ν_7	ν 5-13 (89)	3073	2935	6.14	59.71
ν_8	ν 25-30 (87) + ν 22-28 (6)	3072	2934	69.14	97.60
ν_9	ν 5-13 (93) + ν 6-16 (6)	3067	2929	83.75	189.87
ν_{10}	ν 5-13 (98)	3066	2928	53.81	84.14
ν_{11}	ν 20-26 (78) + ν 20-27 (9) + ν 19-23 (6)	3041	2904	42.60	62.24
ν_{12}	ν 20-26 (81) + ν 20-27 (7) + ν 19-23 (6)	3036	2899	5.20	13.69
ν_{13}	ν 5-13 (85) + ν 1-9 (7)	3025	2889	64.65	22.67
ν_{14}	ν 5-13 (74) + ν 1-9 (20)	3021	2885	16.08	29.95
ν_{15}	ν 6-15 (44) + ν 1-9 (31) + ν 5-13 (9) + ν 5-14 (8)	3019	2883	25.36	120.86
ν_{16}	ν 4-11 (36) + ν 1-9 (35) + ν 4-12 (9) + ν 5-14 (9)	3015	2879	22.84	151.85
ν_{17}	ν 4-11 (54) + ν 1-9 (22) + ν 4-12 (11) + ν 5-14 (5)	3007	2872	11.12	1.96
ν_{18}	ν 18-21 (25) + ν 2 0-26 (23) + τ 3-18-19-22 (12) + ν 4-11 (12) + τ 7-2-3-17 (7)+ ν 5-13 (6)	2985	2851	21.47	2.10
ν_{19}	ν 18-21 (53) + τ 7-2-3-17 (7) + ν 18-19 (7) + ν 3-18 (7) + τ 3-18-19-22 (6) + ν 20-26 (5)	2975	2841	3.048	90.10
ν_{20}	ν 25-11 (81) + ν 22-29 (15)	2912	2781	139.65	126.87
ν_{21}	ν 25-11 (78) + ν 22-29 (15)	2905	2774	28.30	14.93
ν_{22}	δ 15-16-6 (23) + τ 3-18-19-22 (21) + δ 3-18-21 (12) + ν 18-19 (10) + ν 25-32 (10) + ν 22-32 (6) + δ 25-32-22 (6)	1539	1488	1.80	10.51
ν_{23}	δ 15-16-6 (99)	1537	1486	0.35	1.58
ν_{24}	δ 33-32-22 (100)	1528	1478	1.32	11.97
ν_{25}	δ 15-16-6 (88)	1522	1472	11.04	3.20
ν_{26}	τ 7-2-3-17 (17) + ν 5-6 (15) + δ 4-13-5 (13) + ν 5-13 (13) + δ 33-32-22 (8) + ν 1-6 (8) + δ 10-1-9 (5)	1517	1467	0.96	0.26
ν_{27}	δ 15-16-6 (98)	1517	1467	3.28	6.57
ν_{28}	δ 15-16-6 (98)	1514	1464	1.57	13.93
ν_{29}	δ 33-32-22 (63) + δ 4-13-5 (9) + τ 2-3-18-19 (8) + τ 7-2-3-17 (6) + ν 5-13 (6)	1511	1461	0.14	36.41
ν_{30}	δ 33-32-22 (100)	1506	1456	0.09	12.36
ν_{31}	δ 33-32-22 (100)	1496	1447	3.14	0.36
ν_{32}	τ 3-18-19-22 (47) + δ 22-32-25 (39) + τ 7-2-3-17 (8)	1453	1405	11.51	3.30
ν_{33}	τ 7-2-3-17 (37) + τ 3-18-19-22 (26) + δ 3-18-21 (13) + ν 18-19 (7) + ν 3-18 (7)	1423	1376	3.75	2.63
ν_{34}	τ 3-18-19-22 (37) + δ 3-18-21 (23) + ν 18-19 (7) + δ 4-13-5 (7) + τ 7-2-3-17 (7)	1411	1364	1.50	0.08
ν_{35}	δ 4-13-5 (42) + τ 3-18-19-22 (20) + ν 3-18 (9) + δ 3-18-21 (9) + ν 18-19 (7)	1403	1357	2.53	7.90
ν_{36}	δ 4-13-5 (61) + ν 5-6 (16) + ν 1-6 (9) + τ 7-2-3-17 (7)	1403	1357	0.05	3.80
ν_{37}	τ 3-18-19-22 (37) + δ 19-18-21 (22) + ν 18-19 (18) + τ 2-3-18-19 (18)	1394	1348	0.19	5.12
ν_{38}	τ 7-2-3-17 (55) + δ 33-32-22 (17) + τ 2-3-18-19 (16) + δ 4-13-5 (7)	1390	1344	0.38	4.07
ν_{39}	τ 3-18-19-22 (28) + δ 4-13-5 (21) + τ 2-3-18-19 (18) + δ 33-32-22 (12) + δ 19-18-21 (10) + ν 18-19 (8)	1384	1338	0.53	0.28
ν_{40}	τ 3-18-19-22 (47) + τ 7-2-3-17 (33) + δ 3-18-21 (14)	1376	1331	0.02	1.74
ν_{41}	δ 33-32-22 (80) + τ 3-18-19-22 (17)	1376	1331	28.31	2.93
ν_{42}	δ 33-32-22 (48) + τ 7-2-3-17 (24) + τ 2-3-18-19 (17) + δ 4-13-5 (6)	1351	1306	7.09	6.56
ν_{43}	τ 3-18-19-22 (31) + δ 33-32-22 (27) + δ 19-18-21 (26) + τ 2-3-18-19 (13)	1345	1301	2.00	5.31
ν_{44}	τ 7-2-3-17 (41) + τ 3-18-19-22 (33) + δ 4-13-5 (15) + δ 3-18-21 (6)	1332	1288	1.05	6.12
ν_{45}	δ 3-18-21 (49) + δ 25-32-22 (19) + δ 4-13-5 (16) + ν 18-19 (10) + τ 3-18-19-22 (5)	1320	1276	5.38	31.77
ν_{46}	τ 7-2-3-17 (46) + δ 4-13-5 (39)	1308	1265	3.40	19.92
ν_{47}	τ 7-2-3-17 (49) + τ 2-3-18-19 (27) + δ 33-32-22 (7)	1303	1260	3.50	6.79

ν_{48}	δ 4-13-5 (63) + τ 3-18-19-22 (30)	1301	1258	3.44	12.08
ν_{49}	δ 33-32-22 (92)	1247	1206	0.03	9.00
ν_{50}	τ 3-18-19-22 (48) + τ 7-2-3-17 (43) + δ 3-18-21 (7)	1245	1204	7.94	0.57
ν_{51}	δ 33-32-22 (77) + δ 4-13-5 (12) + τ 3-18-19-22 (8)	1218	1178	0.39	3.46
ν_{52}	τ 3-18-19-22 (70) + τ 7-2-3-17 (15) + ν 3-18 (7)	1190	1151	2.61	3.44
ν_{53}	δ 33-32-22 (70) + τ 3-18-19-22 (15) + δ 19-18-21 (6) + τ 2-3-18-19 (5)	1186	1147	0.84	4.59
ν_{54}	δ 33-32-22 (60) + τ 3-18-19-22 (20) + ν 25-32 (6)	1175	1136	18.80	3.59
ν_{55}	τ 3-18-19-22 (63) + ν 3-18 (16) + τ 7-2-3-17 (14)	1122	1085	0.22	4.98
ν_{56}	δ 33-32-22 (31) + ν 18-19 (27) + τ 3-18-19-22 (25)	1121	1084	2.33	5.04
ν_{57}	τ 7-2-3-17 (51) + δ 25-32-22 (13) + τ 3-18-19-22 (11) + ν 18-19 (9) + δ 3-18-21 (8)	1106	1070	8.15	0.25
ν_{58}	τ 7-2-3-17 (40) + τ 2-3-18-19 (23) + ν 5-6 (12) + δ 4-13-5 (10) + ν 1-6 (12)	1106	1070	0.00	0.76
ν_{59}	ν 18-19 (36) + δ 4-13-5 (22) + δ 33-32-22 (19) + τ 7-2-3-17 (10) + τ 3-18-19-22 (6)	1093	1057	0.14	0.28
ν_{60}	δ 25-32-22 (66) + ν 18-19 (13) + τ 7-2-3-17 (9)	1074	1039	1.80	21.85
ν_{61}	τ 2-3-18-19 (26) + δ 4-13-5 (25) + ν 18-19 (18) + δ 4-13-5 (17) + τ 7-2-3-17 (6)	1064	1029	0.00	3.63
ν_{62}	τ 7-2-3-17 (46) + τ 3-18-19-22 (11) + δ 4-13-5 (18) + ν 5-6 (6) + δ 25-32-22 (6)	1050	1015	0.18	7.68
ν_{63}	τ 3-18-19-22 (53) + τ 7-2-3-17 (37) + δ 25-32-22 (5)	1034	1000	6.21	0.12
ν_{64}	τ 3-18-19-22 (54) + τ 2-3-18-19 (23) + δ 19-18-21 (11) + δ 33-32-22 (9)	1005	972	1.35	1.30
ν_{65}	τ 7-2-3-17 (52) + ν 3-18 (29) + ν 18-19 (11)	977	945	0.05	0.85
ν_{66}	τ 7-2-3-17 (54) + τ 2-3-18-19 (17) + τ 3-18-19-22 (13) + δ 4-13-5 (7)	939	908	0.19	0.84
ν_{67}	τ 7-2-3-17 (45) + τ 3-18-19-22 (36) + δ 4-13-5 (8)	925	894	0.52	0.01
ν_{68}	τ 3-18-19-22 (49) + τ 7-2-3-17 (24) + δ 25-32-22 (11) + ν 18-19 (10)	911	881	1.09	3.96
ν_{69}	τ 7-2-3-17 (71) + τ 2-3-18-19 (14) + τ 3-18-19-22 (9)	908	878	2.47	0.45
ν_{70}	τ 7-2-3-17 (76) + δ 25-32-22 (7) + δ 4-13-5 (7)	905	875	2.17	4.68
ν_{71}	ν 18-19 (43) + ν 5-6 (26) + ν 1-6 (14)	863	835	5.43	9.41
ν_{72}	τ 3-18-19-22 (45) + ν 18-19 (26) + δ 25-32-22 (17)	840	812	32.95	2.30
ν_{73}	τ 3-18-19-22 (90) + δ 4-13-5 (5)	826	799	0.47	0.61
ν_{74}	τ 3-18-19-22 (52) + τ 7-2-3-17 (26) + ν 18-19 (12)	807	780	12.46	1.39
ν_{75}	τ 7-2-3-17 (97)	798	772	0.00	0.97
ν_{76}	τ 3-18-19-22 (39) + δ 25-32-22 (37) + ν 18-19 (13)	795	769	46.11	10.66
ν_{77}	τ 3-18-19-22 (68) + δ 3-18-21 (17) + τ 7-2-3-17 (6)	611	591	10.69	0.28
ν_{78}	τ 3-18-19-22 (85) + τ 7-2-3-17 (12)	527	510	16.32	2.16
ν_{79}	τ 3-18-19-22 (83) + ν 18-19 (7)	482	466	0.21	3.04
ν_{80}	τ 7-2-3-17 (55) + τ 3-18-19-22 (44)	469	454	6.88	0.25
ν_{81}	τ 3-18-19-22 (89) + δ 4-13-5 (8)	465	450	0.94	1.10
ν_{82}	τ 7-2-3-17 (84) + τ 3-18-19-22 (14)	440	425	0.05	2.11
ν_{83}	τ 3-18-19-22 (59) + τ 7-2-3-17 (37)	412	398	0.48	0.03
ν_{84}	τ 3-18-19-22 (59) + τ 7-2-3-17 (31) + ν 18-19 (9)	364	352	0.01	0.88
ν_{85}	τ 7-2-3-17 (80) + τ 3-18-19-22 (14) + δ 25-32-22 (6)	360	348	1.64	0.25
ν_{86}	τ 3-18-19-22 (88) + τ 7-2-3-17 (9)	304	294	0.73	0.04
ν_{87}	τ 3-18-19-22 (39) + τ 7-2-3-17 (32) + ν 3-18 (17)	266	257	0.19	3.67
ν_{88}	τ 3-18-19-22 (91) + τ 2-3-18-19 (7)	249	241	0.35	0.17
ν_{89}	τ 7-2-3-17 (92) + τ 2-3-18-19 (8)	227	220	0.02	0.02
ν_{90}	τ 2-3-18-19 (82) + τ 7-2-3-17 (16)	154	149	0.08	0.00
ν_{91}	τ 3-18-19-22 (59) + τ 7-2-3-17 (41)	148	143	0.56	0.03
ν_{92}	τ 3-18-19-22 (55) + τ 7-2-3-17 (44)	77	74	0.28	0.00
ν_{93}	τ 2-3-18-19 (98)	39	38	0.10	0.03

*Scaled with 0.955 above 1800 cm^{-1}, 0.967 under 1800 cm^{-1}. I_{IR} and A_R: Calculated infrared intensities (km/mole) and Raman activities (Å^4/amu). Freq: Frequency.

_____

[1] *J.R. Durig, A. Ganguly, A.M. El Defrawy, G.A. Guirgis, T.K. Gounev, W.A. Herrebout, B.J.Van Der Veken.* ''Conformational stability, r_0 structural parameters, barriers to internal rotation and vibrational assignment of cyclobutylamine'', Journal of Molecular Structure, 918 (2009) 64-76.

[2] Ö. *Alver, C. Parlak, M. Şeny.* ''FT-IR and NMR investigation of 1-Phenylpiperazine: A combined experimental and theoretical study'', Spectrochimica Acta A, 67 (2007) 793-801.

[3] *C. Parlak* ''Theoretical and experimental vibrational spectroscopic study of 4-(1-

Pyrrolidinyl)piperidine'' Journal of Molecular Structure, 966 (2010) 1–7.

[4] *Ö. Alver, C. Parlak* ''Vibrational spectroscopic investigation and conformational analysis of 1-pentylamine: A comparative density functional study'', Journal of Theoretical and Computational Chemistry, 9 (2010) 667-685.

[5] *Ö. Alver, C. Parlak* ''DFT, FT-Raman, FT-IR, liquid and solid state NMR studies of 2,6-dimethoxyphenylboronic acid'', Vibrational Spectroscopy, 54 (2010) 1-9.

[6] *J. Tomasi, in: B. Mennucci, R. Cammi.* (Eds.), Continuum Solvation Models in Chemical Physics: From Theory to Applications, John Wiley & Sons Ltd., England, 2007, pp. 6, 167.

[7] *L. Carballeira, I. Perez-Just.* ''Influence of calculation level and effect of methylation on axial/equatorial equilibria in piperidines'', Journal of Computational Chemistry, 19 (1998) 961-976.

[8] *D. Blackburne, A. R. Katritzky, Y. Takeuchi.* ''Conformation of piperidine and of derivatives with additional ring hetero atoms'', Accounts of Chemical Research, 8 (1975) 300-306.

[9] *P. J. Krueger, J. Jan.* ''Conformational equilibria in some cyclic imines: NH and CH stretching vibrations and the axial lone pair'', Canadian Journal of Chemistry, 48 (1970) 3236-3248.

[10] *R. W. Baldock, A. R. Katritzky.* Journal of the Chemical Society B (1968) 1470-1477.

[11] *G. Gill, D. M. Pawar, E. A. Noe.* ''Conformational Study of *cis*-1,4-Di-*tert*-butylcyclohexane by Dynamic NMR Spectroscopy and Computational Methods. Observation of Chair and Twist-Boat Conformations'', Journal of Organic Chemistry, 70 (2005) 10726-10731.

[12] *W. Lijinsky, G.M. Singer, M.D. Reuber.* ''The effect of 4-substitution on the carcinogenicity of nitrosopiperidine'', Carcinogenesis, 2 (1981) 1045-1048.

[13] *K. Natsuka, Y. Nishikawa, H. Nakamura.* ''Roles of Two Basic Nitrogen Atoms in 1-Substituted 4-(1, 2-Diphenylethyl)piperazine Derivatives in Production of Opioid Agonist and Antagonist Activities'', Chemical and Pharmaceutical Bulletin. 47 (1999) 1790-1793.

[14] *F. Berardi, C. Abate, S. Ferorelli, V. Uricchio, N.A. Colabufo, M. Niso, R. Perrone.* ''Exploring the importance of Piperazine N-Atoms for σ_2 Receptor Affinity and Activity in a Series of Analogs of 1-Cyclohexyl-4-[3-(5-methoxy-1,2,3,4-tetrahydronaphthalen-1-yl)propyl]piperazine (PB28)'', Journal of Medical Chemistry, 52 (2009) 7817-7828.

[15] *M.J. Frisch, G.W. Trucks, H.B. Schlegel, G.E. Scuseria, M.A. Robb, J.R. Cheeseman, G. Scalmani, V. Barone, B. Mennucci, G.A. Petersson, H. Nakatsuji, M. Caricato, X. Li, H.P. Hratchian, A.F. Izmaylov, J. Bloino, G. Zheng, J.L. Sonnenberg, M. Hada, M. Ehara, K. Toyota, R. Fukuda, J. Hasegawa, M. Ishida, T. Nakajima, Y. Honda, O. Kitao, H. Nakai, T. Vreven, J.A. Montgomery, Jr., J.E. Peralta, F. Ogliaro, M. Bearpark, J.J. Heyd, E. Brothers, K.N. Kudin, V.N. Staroverov, R. Kobayashi, J. Normand, K. Raghavachari, A. Rendell, J.C. Burant, S.S. Iyengar, J. Tomasi, M. Cossi, N. Rega, J.M. Millam, M. Klene, J.E. Knox, J.B. Cross, V. Bakken, C. Adamo, J. Jaramillo, R. Gomperts, R.E. Stratmann, O. Yazyev, A.J. Austin, R. Cammi, C. Pomelli, J.W. Ochterski, R.L. Martin, K. Morokuma, V.G. Zakrzewski, G.A. Voth, P. Salvador, J.J. Dannenberg, S. Dapprich, A.D. Daniels, Ö. Farkas, J.B. Foresman, J.V. Ortiz, J. Cioslowski, D.J. Fox.* Gaussian 09, Revision A.1, Gaussian Inc., Wallingford CT, 2009.

[16] *N.M. O'Boyle, A.L. Tenderholt, K.M. Langner.* J. ''cclib: A library for package-independent computational chemistry algorithms'' Comp. Chem. 29 (2008) 839-845.

[17] *J.M.L. Martin, C. Van Alsenoy.* GAR2PED, University of Antwerp, 1995.

THE INFLUENCE OF MOLTEN ZONE LENGTH ON COMPONENT AXIAL DISTRIBUTION IN InAs-GaAs INGOTS AT FLOATING-ZONE REFINING

S.M. BAGIROVA, Z.M. ZAKHRABEKOVA, V.K. KAZIMOVA, G.H. AJDAROV

Institute of Physics of Azerbaijan NA
AZ-1143,H.Javid ave.,33,Baku, Azerbaijan
Baku-143, E-mail: zangi@physics.ab.az, tel.:(+99412)4393218, Fax: (+99412)4395961

In Phan approximation the regulation possibility in wide limits for axial concentration component distribution in InAs-GaAs ingots by the way of the length change of molten zone at floating-zone refining of solid solution is shown. It is shown that mathematical modeling of component distribution in ingots defines the optimal technological parameters (molten zone length and initial ingot one, ingot initial composition) for growing of InAs-GaAs crystals with the given homogeneous and nonhomogeneous compositions.

The semiconductor solid solutions $(InAs)_{1-x}(GaAs)_x$ are the one of perspective functional materials for optoelectronic devices, in particular, IR-laser diodes [1]. The composite components of this system are totally solved in each other in any ratios both liquid and solid states [2]. The big difference in forbidden band widths of indium and gallium arsenide (0.41 eV in InAs and 1.52 eV in GaAs) opens the possibility of precision regulation for the value of this fundamental parameter in solid solutions of these crystals by the way of simple change of their composition.

The mathematical modeling of the influence of molten zone width on axial concentration component distribution in solid solution single crystals InAs-GaAs at floating-zone refining of initial ingot of this melt is carried out in the given work. The aim is the establishment of possibility of floating-zone refining method and optimal operational parameters for crystal growing InAs-GaAs with the given variable and constant compositions. The analogous tasks are solved in works [3-8] for crystal system silicon-germanium grown up by both conservative and non-conservative methods. The results of these works carried out in Phan approximation show the well agreement with corresponding experimental data.

The conceptual growing scheme of solid solution single crystals InAs-GaAs by vertical floating zone method is presented on fig.1. The previously prepared macro-homogeneous rod of solid solution (3) is put under single-crystal seed (1) of InAs-GaAs of corresponding composition [5]. The melting of rod initial part under the seed is carried out in the heater with temperature field shown from the left on the scheme. On the expire of the stabilization time the device shifting crucible down relatively heater switches on that leads to molten zone shift up along ingot. During whole cycle of ingot recrystallization, the molten zone length (Z) (2) is kept constant up to the formation of final band presented on scheme (c) of fig.1.

The one-dimensional task of axial component distribution in InAs-GaAs crystal grown up by vertical method of molten zone is solved in Phan approximation at carrying out of following standard conditions [9]: there is balance between liquid and solid phases on crystallization front defined by state diagram ; diffusion rates of InAs

and GaAs molecules in molten zone are enough high ones and supply the composition uniformity along whole zone volume; the component diffusion in solid phase is negligible small one; component segregation coefficients change with melt composition in correspondence with system phase state diagram; the evaporation and decomposition of composition components is absent in the melt; the crystallization front is plane one; the composition of initial polycrystalline ingot is macroscopically homogeneous one.
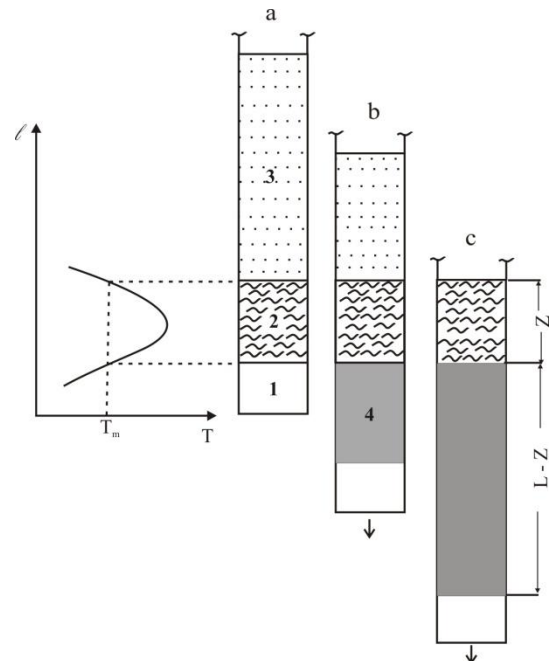

Fig.1. The conceptual scheme of solid solution InAs-GaAs growing by floating zone method. 1 is the seed, 2 is melt, 3 is macrohomogeneous ingot InAs-GaAs, 4 is recrystallized ingot; *a* is initial moment of melt crystallization, *b* is crystallization intermediate stage, *c* is formation moment of final zone. There is temperature field in the melt in left part of figure.

Let's introduce the following designations: V_m^0 and V_m are molten zone volumes in initial and current

moments; C_c, C_i, C_m are molecule (parts) concentrations of second component (GaAs) in the crystal, initial ingot and melt correspondingly; C_m^0 is second component concentration in molten zone in initial moment; C is total second component in melt; V_i is ingot volume InAs-GaAs melting in time unit; V_c is melt volume crystallizing in time unit; L, ℓ, and Z are lengths of initial ingot of recrystallized ingot part and molten zone correspondingly; $K = C_c/C_m$ is equilibrium coefficient of GaAs .

Taking into consideration the accepted designations, under condition of constancy of melt crystallization velocity, we have:

$$C_m = \frac{C}{V_m}; \qquad \frac{dC_m}{dt} = \frac{\dot{C}V_m - \dot{V}_m C}{V_m^2} ;$$

$$V_m = V_m^0 - (V_c - V_i)t \qquad (1)$$

Before the final molten zone by task condition we consider that Z and V_i and V_c don't depend on time. Then in ingot segment by length L-Z (see fig.1c) in floating-zone refining process we have the following relations:

$$V_m = V_m^0, \ \ C_m^0 = C_i \ \text{ and } \ \dot{C} = V_c C_m K + V_i C_m^0 \quad (2)$$

Substituting (2) into (1) and after transformation and integration we obtain:

$$\int_{C_m^0}^{C_m} \frac{dC_m}{C_m^0 - C_m K} = \frac{l}{Z} \qquad (3)$$

The equation (3) defines the crystal composition by its length on interval from $\ell = 0$ up to $\ell = L\text{-}Z$.

From formation moments of final molten zone by Z length the following relations are true:

$$V_m = V_m^0 - V_c t , \ \ \dot{V}_m = -V_c, \ \ \dot{C} = -V_c \, C_m K \quad (4)$$

Substituting (4) into (1) and integrating we have:

$$\int_{C_{mf}^0}^{C_m} \frac{dC_m}{C_{mf}^0 - C_m k} = \ln \frac{V_m^0}{V_m^0 - V_c t} \qquad (5)$$

Here C_{mf}^0 the second component concentration in final molten zone by length L and volume V_m^0. Designating the part of crystallized final zone $V_c t / V_m^0$ by symbol γ let's write the equation (5) in the following form:

$$\gamma = 1 - \exp\left[-\int_{C_m}^{C_{mf}^0} \frac{dC_m}{C_m K - C_m} \right] \qquad (6)$$

For integral solving in (3) and (6) it is necessary the knowledge of analytic dependence of second component segregation coefficient K on C_m. The dependence K on C_m calculated by phase state diagram of system InAs-GaAs is presented on fig.2 [1]. As it is seen from the figure, K changes complexly with melt composition in wide range from value ~20,5 up to 1 and doesn't described analytically. However, one can define the integral values in equations (3) and (6) by numerical method [2,5] using data of fig. 2. As every value of melt composition corresponds to conjugate value $C_c = C_m K$ then one can construct the dependence plot of component concentration distribution along whole length of recrystallized ingot.

The character curves of component concentration distributions in ingots InAs-GaAs calculated from equations (3) and (7) by numerical method for different values Z are presented on fig.3. In calculations the start composition of whole ingots corresponds to content of GaAs that is equal to 20 mol.%. As it is seen from this figure the operation parameter Z essentially influences on component redistribution at floating-zone refining of macro-homogeneous ingot InAs-GaAs. Moreover, the lengths of both non-homogeneous and homogeneous crystal parts by composition are defined by molten zone width. The curve family presented on fig.3 demonstrates the possibility of mathematical modeling for definition of optimal operation parameters for InAs-GaAs crystal growing with given homogeneous and nonhomogeneous compositions.
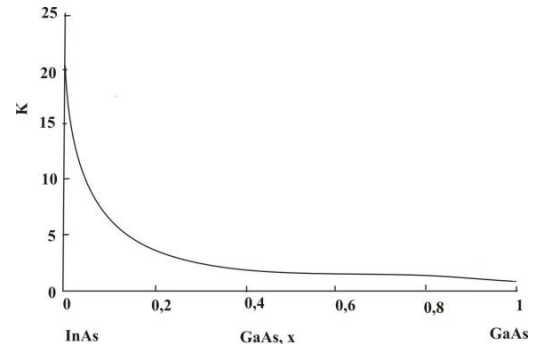

Fig.2. The dependence of InAs segregation coefficient (K) on $In_xGa_{1-x}As$ melt composition calculated by data of phase state diagram [2].

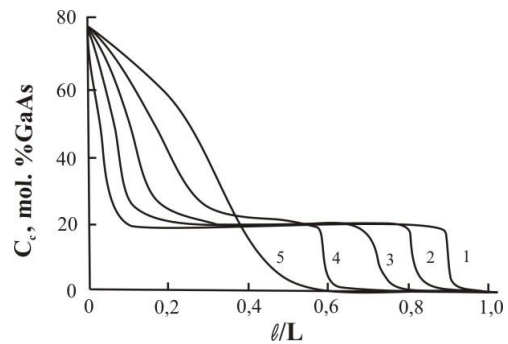*Fig.3.* The concentration profile GaAs in solid solution of crystals InAs-GaAs grown up by floating zone method from $In_{0.8}Ga_{0.2}As$ initial ingot. The molten zone length: (1) *Z=0,1L*; (2) *Z=0,2L*; (3) *Z=0,3L*; (4) *Z=0,5L*; (5) *Z=0,7L*; *L* is initial ingot length.

Summarizing the above mentioned data, one can state the following. The math modeling of component distribution in crystals InAs-GaAs at floating-zone refining carried out with taking into consideration the complex dependence of component segregation coefficient on melt composition, allows us to estimate the optimal technological parameters such as molten zone length and ingot start composition for obtaining of crystals with given concentration profile of components.

_____

[1] *N. Nakamura, Y. Hanaue, H. Kato, S. Yoda*, J. Crystal Growth. 258, 49 (2003).
[2] *V.S. Zemskov, V.B. Lazarev.* Tverdie rastvori v poluprovodnikovikh sistemakh. Moskva: Nauka, 1978. (in Russian)
[3] *G.Kh. Azhdarov, T. Kucukomeroglu, A. Varilci et. al.*, J. Crystal Growth. 226, 437 (2001).
[4] *Yonenaga*, J. Crystal Growth. 226, 47 (2001)
[5] *N.V. Abrosimov, S.N. Rossolenko, W Thieme. et. al.*, J. Crystal Growth. 174, 182 (1997).

[6] *P.G. Azhdarov, N.A. Agayev*, Neorganicheskie materiali. 35, 8, 763 (1999).
[7] *C. Marin, A.G. Ostrogorsky*, J. Crystal Growth. 211, 378 (2000).
[8] *K. Kadakura, Y.Takano*, J. Crystal Growth. 171, 56 (1997).
[9] *V.M. Glazov, V.S. Zemskov*, Phiziko-khimicheskie osnovi legirovaniya poluporovodnikov. Moskva: Nauka, 1967. (in Russian)

PHOTOGALVANIC EFFECTS IN CuGaSe$_2$ MONOCRYSTALS

I. ƘASUMOGLU, I.A. MAMEDOVA, G.G. GUSEYNOV, M.A. ALIYEV
Institute of Physics of Azerbaijan NAS
AZ-0143, H.Javid ave., 33, E-mail:igasimoglu@yahoo.com

The investigation of laser influence (0,63μm) and γ-radiation on short-circuit current in CuGaSe$_2$. The observable inversion of sort-circuit current dependent on wave length and also the current intensity change and widening to long-wave side is connected with carrier concentration increase after treatment by laser and γ-radiation.

INTRODUCTION

The interest to semiconductor compounds of A^{I}B^{III}C$^{VI}_2$ type which is triple analogues of binary semiconductors A^{I}B^{VI} is caused by perspective of their use in semiconductor instrument engineering in particular, the single crystals CuGaSe$_2$ are perspective ones for formation of photoelements, light-sensors for temperatures in visible region. The crystal forbidden band width is optimally close to one for sun element material (1,65 eV at 300 K).

The compounds A^{1}B^{III}C$^{VI}_2$ have the simmetry point group $\overrightarrow{42}\,m$, [1]. In these materials the possibility of radiation recombination is big one. The observable phenomenon of double refraction can be used in nonlinear optic elements [2]. The photoconduction [3], photo-e.m.f [4], influence of γ-radiation on electric properties of single crystals CuGaSe$_2$ [5] are studied by us for material perspective revealing for technical aims.

The investigated crystals are obtained by gas-transport method. The crystal iodine is used in the capacity of transporter. The sample resistance is 20 MΩ (at 300°K), the conduction is p-type.

The high-sensitive registering devices for measurements of weak and strong radiations are required in different fields of science and technology. That's why the essential interest for this aim presents the use of triple compounds including CuGaSe$_2$ the properties of which strongly change under influence of radiation different types.

In present work the investigation results of photocurrent spectral dependence after irradiation by laser and γ-rays (E=60R/sec., t=10min.) are given.

EXPERIMENTAL RESULTS AND DISCUSSION

The samples for experiment is chosen thus that the value and short-circuit current sign dependent on crystal polarization. This is the evidence of photogalvanic character I$_{sc}$. Such crystals are grown very complexly. The obtained crystals have the needle form with mirror surfaces.
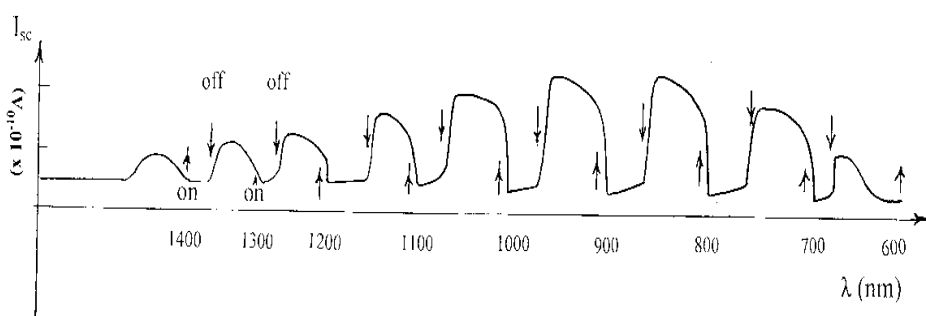

Fig. 1. Short –circuit spectral dependence of of CuGaSe$_2$ monocrystals at temperature 77 K (basic)
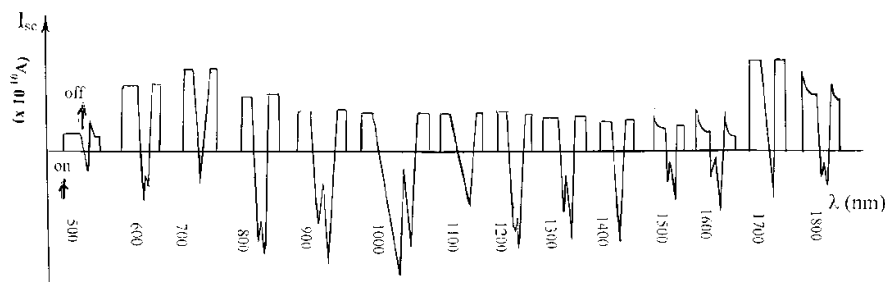

Fig. 2. Short –circuit spectral dependence of of CuGaSe$_2$ monocrystals after laser illumination (0,63μm, 10 min) at temperature 77К

The contacts from silver pasta are used in the capacity of electrodes. The average sizes of investigated crystals are 1x0,5x5mm. For measurement of photogalvanic effect the crystals are homogeneously lightened by polarized light in direction [001]. The experiments are carried out on comparison technique of short-circuit current spectra: before and after laser treatment (0,63 µm) and γ-radiation. The signals are measured by high-sensitive electrometric voltmeter B7-30.

The initial sample spectrum, in which short-circuit current values are positive ones is presented on fig.1. The unique current inversion dependent on wave length (fig.2) and also changing current intensity and conduction band widening in long-wave side are observed in crystal spectra radiated by laser (0,63 µm, t=10 min). The enhanced role of thermodynamic equilibrium leads to the fact that practically any nonequilibrium destroys the compensation thin mechanism and causes the current in mediums without center of symmetry [6]. The compounds $A^I B^{III} C^{VI}_2$ are non- centrosymmetrical crystals and that's why the possibility of photogalvanic effect observation in these objects appears. In single crystals of this group the photogalvanic effects (PhGE) are revealed by us in AgGaSe2 [7]. In the present work PhGE investigation results in single crystals CuGaSe2 are firstly given. It is clear that the currents of another nature are possible in thermodynamically nonequilibrium conditions. The photogalvanic effect: the constant current appearance in homogeneous crystals under lightening influence. The obtained photogalvanic effect in crystals without center of symmetry is phenomenologically described by equation.

$$I_i = \alpha_{ijk} E_j E_k^* + J_{ij} i [EE^*]_j \qquad (1)$$

$$J_i = \alpha_{ijk} E_j E_k^* \qquad (2)$$

$$J_i = \alpha_{ijk} \qquad (3)$$

Here J_i is photogalvanic current, E_j, E_k are vector components of light polarization, $i [EE^*]_j$ defines the circulation degree of light polarization, α_{ijk} and J_{ij} are tensors describing the linear and circular PhGE correspondingly. All information about PhGE is in photogalvanic tensor of third rank. At space inversion of current sign J_i changes and E_j, E_k values don't change. That's why tensor α_{ijk} can differ from zero only in mediums without center of symmetry. The short-circuit photo-current is observed I_{sc} [7]. The short-circuit photo-current I_{sc} consists of transversal and stationary components. If transversal short-circuit photo-current presents itself the pyro-current connected with weak pyroelectric heating because of photo-active light absorption, then stationary signal is specific one for polar crystals [8]. After treatment and light switching on, the photo-current strongly decreases, the sign changes and from opposite side approximates to zero. Such kinetic spectra are repeated for each wave length at which the spectrum form changes in the dependence on composition, i.e. on intensity of each light length. The

spectral distribution of stationary current I_{sc} in crystal is correlated with spectral distribution of photoconduction (PhC). The main maximum has the impurity nature. We propose that this takes place because of formation of new effect in the samples. The PhGE kinetics depends on temperature, intensity and spectral distribution of the light. Thus, PhGE kinetics depends on trap depth. This is clearly seen after γ-irradiation and we have the exhaust of these traps (fig.3).

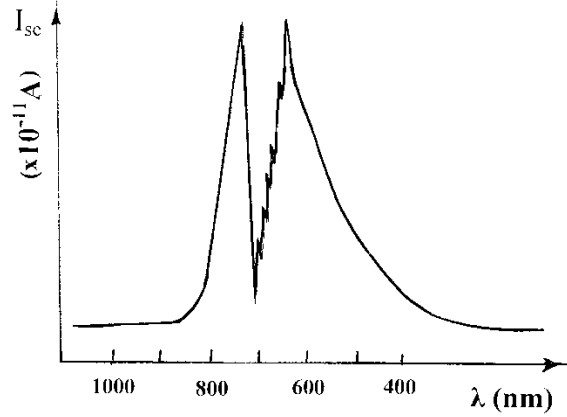*Fig. 3.* Short –circuit spectral dependence of CuGaSe2 monocrystals after γ-irradiation at temoerature77K (E=60 R/sec, t=10 min)

The experiment data evidence about the fact that the transfer by carrier can be carried out in the correspondence with PhGE model at transition impurity-zone because of local asymmetry of impurity center and at zone-zone transition can be carried out because of emission asymmetry on impurities and phonons [9]. The kinetic spectra of PhGE show that this effect in CuGaSe2 single crystals has the intrinsic and impurity natures. That's why the obtained physical parameters open the way for object use in applied electronics including for production of ionizing radiation detectors. By our opinion from PhGE spectrum one can define the center of location (energy position) of deep traps. And one can explain the effect revealing by deep acceptor levels which are near valent band. The crystal treatment leads to sensitivity widening in wide interval and leads to increase of carrier concentration in traps and center recharging. The center recharging caused by laser treatment and γ-radiation changes the spectral distribution of photogalvanic effect and reveals the essential growths of photoeffect and photogalvanic current in spectrum long-wave region [10].

CONCLUSION

All facts show that continuing the experiments we approach to the aim which is in production of photo-and gamma-galvanic radiation detectors with high physical parameters. If treatment is carried out by γ-radiation the sign and value of short-circuit current very strongly changes that we observe from carried experiments. This takes place when the dosage rate increases. Experiments show that treatment by radiation acts as improvement factor of sample sensitivity.

_____

[1]   J. Appl. Phys. 19 (1980) Suppl. 19-3 p III.

[2]   *A.I. Dirochka, G.S. Ivanova, L.N. Kurbatov, E.B. Sinitsin, F.R. Khorokhorin, E.I. Kholina*. FTP, 9, 1975, 1128. (in Russian)

[3]   *T.K. Kasumov, M.A. Aliyev, F.I. Mamedov*. Photoprovodimost v monokristallakh CuGaSe$_2$, VINITI, Dep. №90-83, 1983. (in Russian)

[4]   *I. Gasimoglu, I.A. Mamedova, G.S. Mekhtiyev*. Fizika, t. XIII, N4, s.130-131, 2007. (in Russian)

[5]   *I. Kasumoglu, T.G. Kerimova, I.A. Mamedova*. FTP, t.45, v.1, 2011, s.32-34. (in Russian)

[6]   *V.I. Beliniker, B.I. Sturman*. Uspekhi fizicheskikh nauk. 1980, t.130, v.3, s.426. (in Russian)

[7]   *T.K. Kasimov, F.I. Mamedov and I.K. Gasimov*, Negative Photoconductivity in AgGaSe$_2$ single crystals due to the Negative Photogolvanic effect, Phys.Stat.Sol. (a) 107, K49, 1988

[8]   *B.E. Baglikov, V.N. Kornetov, A.N. Ognev, B.N. Popov.* Pisma v JTF, t.37, v.1, s. 3-5, 1983. (in Russian)

[9]   *V.M. Fridkin*. Segnetoelektriki - poluprovodniki, M.1976, s.258. (in Russian)

[10] *T.M. Batirov, K.A. Verkhovskaya, A.A. Katarzin, Yu.N. Malovichkiy, V.I. Lisoivan, V.M. Fridkin*. FTP, 1981, s.1313-1315. (in Russian)

THE SELF-ORGANIZATION OF LOW-DIMENSIONAL STRUCTURES IN VOLUME CRYSTALS $A_2^V B_3^{VI}$<IMPURITY> AND THEIR MORPHOLOGY

S.SH. KAKHRAMANOV, F.K. ALESKEROV, S.A. NASIBOVA

SPU "Selen" of Azerbaijan NAS, Baku, Azerbaijan

The morphological formations formed in atom aggregation process in medium $Te^{(1)}$–$Te^{(1)}$ in $A^V_2 B^{VI}_3$<impurity> are studied. In this medium as in nano-container the self-organization process of nickel, zinc and selenium atoms in в $A^V_2 B^{VI}_3$ takes place.

The atom introduction at intercalation takes place mainly between quintets. The structures with quantum points (QP), from which the self-organization of quantum wires and fractal macro-stages is carried out as a result of migration processes, form as a result of atom aggregation.

The winning in thermo-electric efficiency in nano-structured material in the comparison with initial solid solution material is possible because of electron tunneling through barrier layers of QP having the dimensions less than 50nm. One can't achieve ZT value more than 1,1in system $A_2^V B_3^{VI}$<N_i> system because of QP big sizes (more than 30nm) in spite of theoretical forecasts (ZT>3).

Keywords: self-building, low-dimensional structures, porosity, self-organization, super saturation.
PACS: 05.65.+b, 52.77.Dq, 68.55. – a, 81.15.Cd, 81.16. – c

INTRODUCTION

The structural processes carrying out on interlayer surface (0001) of $A^V_2 B^{VI}_3$ crystals play the essential role at obtaining of lowered dimension systems: quantum points (QP) and quantum wires (QW), stage structures and superlattices. The atom direction migration along surface being the reason of self-organization of periodically wave-similar stage structures in crystals [1-2], is the important moment. Thus, by our data, [3] the ordered stages are revealed in doped layered systems in intercalation processes. The interlayer growth stages with nano-fragments on Van der Waals surface (0001) Bi_2Te_3 are studied by the method of atomic-force microscopy (AFM).

The analisys of the works carried out by us in this field shows that stage-layer qrowth of surface is observed on different type crystals (wolfram, Si, Bi_2Te_3 and etc) at different technologies (at epitaxy, intercalation) with the use of self-organization processes. At increased temperatures of crystal the processes of generation, movement and absorption of adsorbed atoms on the surface take place. These processes lead to fluctuations of stage form. The stage fluctuations on the surface have the Brownian motion characteristics:

- adatoms and vacancies are accidentally generated (or absorbed) by stage edges.

At crystal temperature increase one can expect the increase of fluctuation amplitude of surface stage segments because of increase of elementary break concentration that should lead to increase of effective width both single stages and macro-stages (that equivalently to the decrease of stage linear tension). At observation of surface structural processes the instability of regular atom stage system on crystal surface is observed. The transition of stage regular distribution in echelons of closely situated stages divided by terraces with decreased density of atom stages is the result of this instability. The revealing of strongly defined temperature sublimation intervals, in which the echelonment effect is observed, is unusual.

The chalcogenides Bi and Sb can be crystals in which the elastically tensed macro-stages appear. The formation of interlayer nano-fragment arrays in layered crystals grown up by directed crystallization is studied in [4]. In layers of $T_e^{(1)}$-$T_e^{(1)}$ Sb_2Te_3 and Bi_2Te_3 the structures having stage-layered character with nano-structured islands grown up on them are revealed. It will be shown that the echelonment phenomenon is typical for interlayer nano-objects and can reveal at floating-zone refining of solid solution on the base of Sb_2Te_3 [5].

It is established in [5] that the "radial" or "ring" structures form in addition to "directed" texture at vertical zone melting of solid solution p- $Bi_{0.5}Sb_{1.5}Te_3$. The formation of these textures can be connected with influence of ampoule walls and melt flows in crystallization region on appearance and development of material crystallization centers with strong anisotropy of velocity growth. The materials with "ring" texture have the essential bigger strength at splitting along growth direction than samples with "radial" one. The given fact is explained by the fact that the destruction of samples with "ring" texture is connected with the break of strong ion and covalent bonds and the destruction of samples with "radial" texture is connected with the break of weak Van-der-Waals bonds.

The studied surface interlayer nano-fragments in $A_2^{VI}B^{VI}_3$ systems can influence on their surface states. For example, the results of article [6] in which the theoretical investigations of electron structure of surface of compounds $A_2^V B^{VI}_3$, containing the topologically protected states. Here the ideal surfaces of Bi_2Te_3, Bi_2Se_3 and Sb_2Te_3 and surfaces with missing external chalcogen atom layer observing experimentally in the form of many-layered terraces are considered. It is shown that the existing divergence between theoretical level position and observed in photoemission experiments can be explained by the presence of states of "broken bond" type on terrace surfaces formed by semi-metal atoms [6].

The theoretical investigations of increase possibility of thermoelectric quality Z in volume nano-structured thermoelectric materials are carried out in [7]. The calculation and estimation of kinetic coefficients of nano-structured materials in supposition that the electron tunneling between nano-particles plays the main role in

the transfer are carried out. The limit case of phonon heat conduction absence through barrier layers is considered. The estimations for materials on Bi_2Te_3 base show that thermo-e.m.f. in nano-structured material can be enough high one and dimensionless thermoelectric quality (ZT) in spite on non-high electric conduction can achieve the values 3-4 at room temperature [7]. At calculations of kinetic coefficients [7] the limit case of vacuum gap between nano-particles when phonons can't tunnel through barrier layers, is considered. It is still unclear what presents itself the real gap between nano-particles in the investigated volume structures; one can expect that there is very thin oxide film. Thus, the above mentioned results demonstrating the possibility of thermoelectric quality Z increase due to the tunneling effect can consider as limit ones.

However, it is necessary to note that the minimal nano-particle sizes (10-20nm) are used in calculations. In real volume thermoelectrics after nano-particle hot pressing the structural element sizes can be essentially bigger (50 and even 100nm) [7]. It is obviously that at bigger sizes of structural elements the quality Z increases less essentially. Thus, the both considered factors show on the fact that the quality Z increase in real situation can be less than one in calculations.

In many works the details of nano-wire increase processes stay unnoticed. That's why the interest present the techniques allowing us to observe the nano-wire formation directly in processs of their increase. It's impossible to grow the silicon nano-wires of big length from drops of given size. The nano-wires on $A_2^V B_3^{VI}$ base with self-organizing nano-islands and quantum points are presented perspective ones for thermoelements (TE) .

Now in spite on many works dedicated to investigation of islands in Bi_2Te_3 there are many unsolved questions about of mechanism of growth and composition of islands and also the elastic strengths in them. The big interest to self-organization process on growth surface in elastic-stressed systems is connected with possibility of nano-object obtaining in interlayer space.

The task of interlayer nano-objects connected with self-organization effects on Van der Waals surface (0001) $A_2^V B_3^{VI}$ <impurity> leading to formation of interlayer stages, QP and QW is estimated on the base of above mentioned fact analysis.

EXPERIMENTAL RESULTS AND DISCUSSION

AFM method is very useful as it allows us to investigate the topography and profile diagrams of Van der Waals surface (0001) of monocrystalline samples. AFM images are obtained on scanning probe microscope (SPM) by Solver Next trend. The X-ray diffraction investigations of surface (0001) are carried out on diffractometer (XRD) by Philips Panalytical trend .

At surface relief investigation we apply the semicontact method which is the foundation for realization of other method series connected with use of cantilever resonance oscillations.

The formation stages of quantum points and quantum nano-wire on surface (0001) $A_2^V B_3^{vi}$

The inserted impurities are introduced not only in main matrix lattice of $A_2^V B_3^{VI}$, but they accumulate between telluride quintets forming the different nano-formations: so In exchanges Bi place in sublattice, and nickel being the weak acceptor, easily takes the space $Te^{(1)}$- $Te^{(1)}$ forming QP.

The ordered accumulation of impurity atoms between quintets $Te^{(1)}$- $Te^{(1)}$ which aggregating accumulate in the form of nano-clusters, takes place on Van der Waals surface of $A_2^V B_3^{VI}$ (0001). Then, the nano-clusters form the nano-islands playing the quantum point role as a result of coagulation at gradient annealing (<600K) (see fig.1a, b, c).
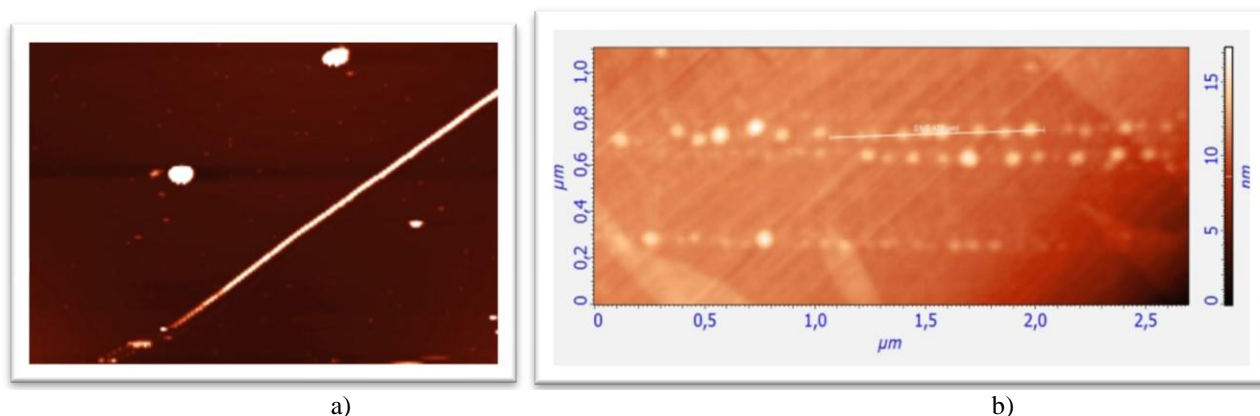

a)   b)

Fig.1. AFM-image in 2D- scale Bi_2Te_3<Zn> : a)nano-island chains, QW fragment formed from QP in Bi_2Te_3<Zn> system- b).

The exhaustion bands: the small islands decrease in the dimension and disappear, appear round aggregated nano-islands. Not only quantum points, nano-wires, but interlayer stage structures (fig.2) form as a result of surface diffusion and further aggregation. The profile diagram of nano-stage distribution has obviously fractal character (see fig.2 b).

Whereas the diffusion square increases, the clusters interact with linear defects (of screw dislocation types) and form the new nano-formations with plane tops (fig.3). Such relief structures are shown on the figure by horizontal hands, the single nano-island of conic form is shown on the right side by vertical hand. Such QP are character for zinc in Bi_2Te_3<Zn system.
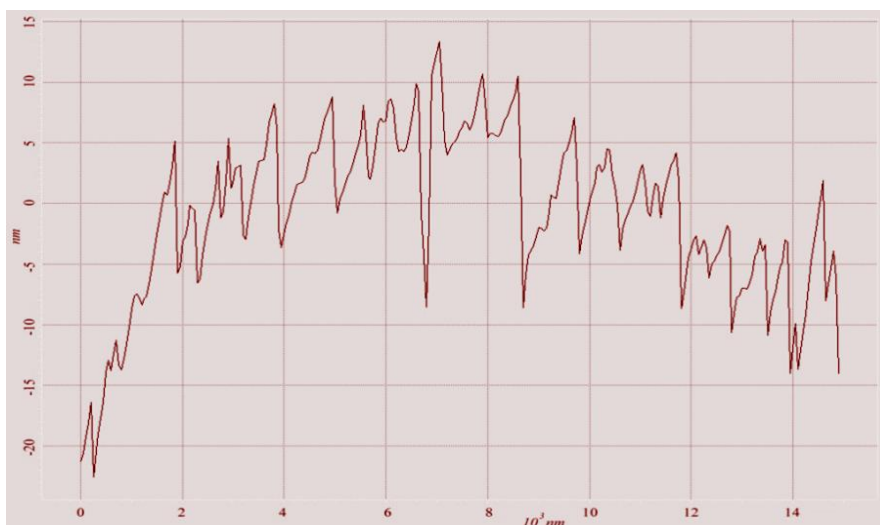
The interlayer quantum points (fig.4) play the important role in electron-phonon interaction in layered crystals of $A_2^V B_3^{VI}$ type. QP data in Bi_2Te_3<Ni 0.1% atm.> system have the surface density which is equal to $1,6\cdot10^{10}$ cm^{-2} (fig.4).
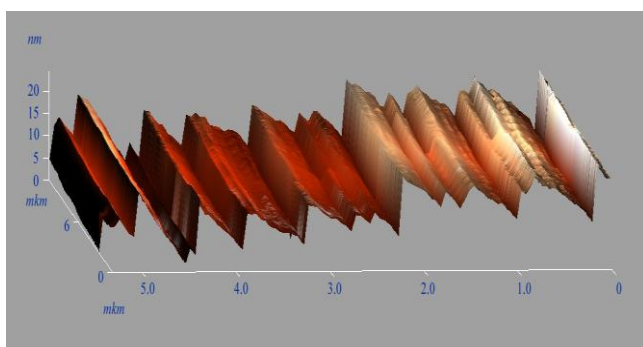
a
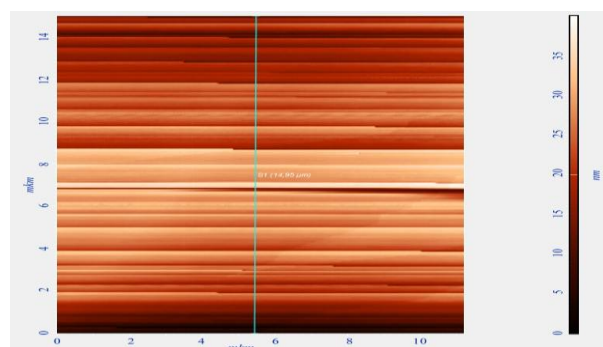
b

c

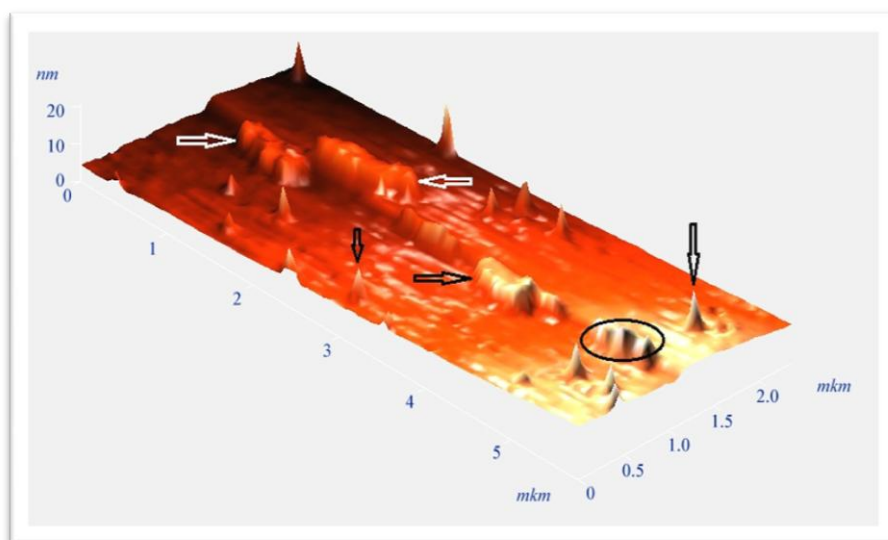*Fig.2.* Fractal character of nano-stage distribution in Bi_2Te_3<Se>.

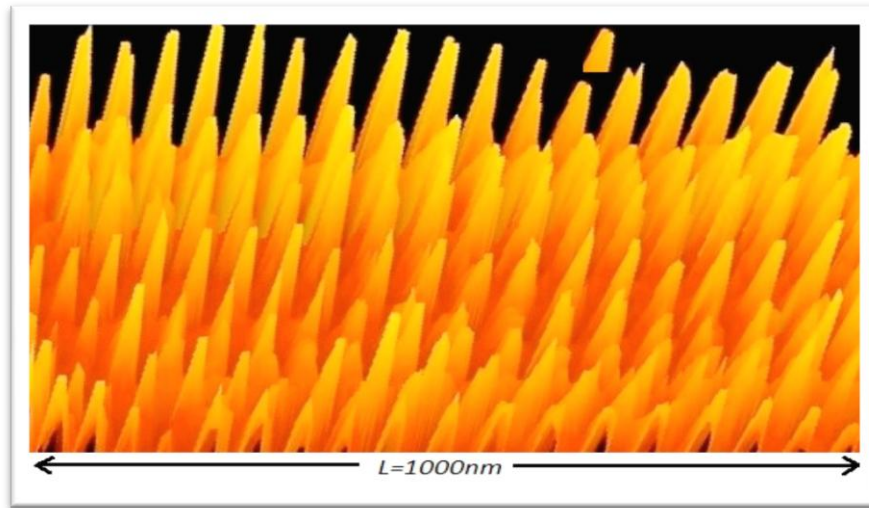*Fig.3.* The nano-relief of dislocation character in Bi_2Te_3<Zn>.

Fig.4. QP distribution in Bi$_2$Te$_3$<Ni> system.

The QP fragment having the dimension ≈ 40nm and the distance betweenQP is equal to ≈ 10nm, is shown in the insertion on the top of this figure .

The effect domination of space quantization should be observed in A$_2^{V}$B$_3^{VI}$ <Se, Ni> structures with such islands. The formation dynamics of nano-wires from nano-islands is presented on fig.5. The nano-wire fragments are given on the right in insertions of figures 5a,b. The formation of such nano-fragments is presented more obviously on fig.5c, such self-organization dynamics of QP construction in the sesries is observed from left to the right (on fig.5c).
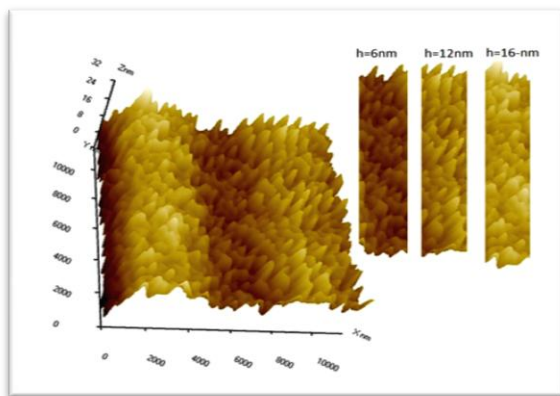
a
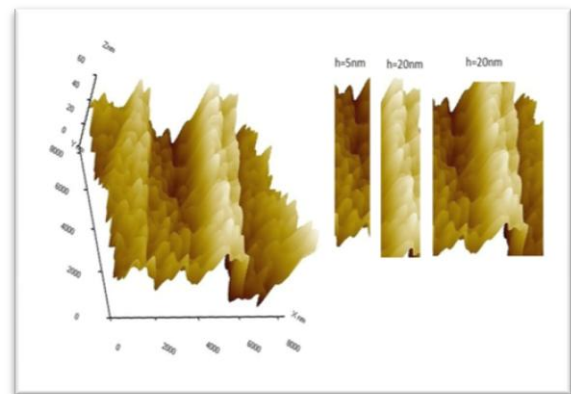
b

Fig.5.a,b QP aggregation dynamics
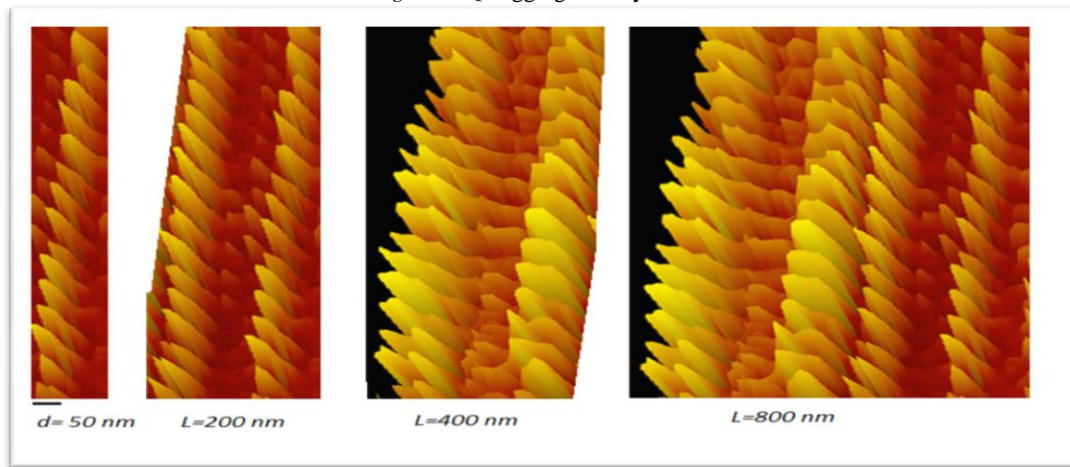
c

Fig.5.c QW self-organization.

As a result the nano-fragments with 40-50 nm form between $Te^{(1)}$- $Te^{(1}$

The given technology is essentially more cheep in the comparison with molecular epitaxy applied for sample preparation containing the quantum-dimensional structures. The new effect appearance such as charge carrier tunneling between nano-particles and also the additional phonon scattering on the boundary between QP or at breakage with further pressing and connected with it heat conduction decrease, is possible in nano-structured material. These effects should lead to increase of thermoelectric efficiency. The considered samples with high values of quality Z can be used for creation of effective thermoelectric transformers in spite of comparable low electric conduction (less ~600 om^{-1}·cm^{-1} and high thermo-e.m.f. α=260μV/K). Indeed, one easily can change the geometry of thermoelectric module branches in order to supply the required current flow in this thermoelement.

During Bi_2Te_3 crystal growth towards with impurities including into the layers the comfortable conditions for formation of both impurity nano-fragments and fractal formations round dislocation grids, vacancy rings, point defects and dislocation dipoles (and pair etch pits) are formed

The interlayer nano-fragments one should consider as fractals defining the interlayer space morphology and influencing on many properties including mechanical ones.

The non-uniform distribution both the fractal benches (light nano-formations in the middle) and hardly seen defect "fields" are seen from electron-microscopic images. Such character defects are in stoichiometric and doped by nickel crystals Bi_2Te_3<Ni> (fig.2.b). During growth process one can hardly to avoid the appearance of needless blocks growing preferentially from one crystal side. The morphology analysis of Bi_2Te_3 surface (0001) shows that nano-particles (in the form of nano-fractal formations) can form between layers $Te^{(1)}$- $Te^{(1)}$ with participation of impurities, dislocations and packing effects (see fig.3).

The two methods of atom introduction with small atom ion radiuses (Ni) are revealed. The nano-fragments form in interlayer space: during synthesis process with further crystal growing and intercalation as a result of gradient diffusion. The formation of double nano-islands probably can be connected with pair localization of dislocation pits (fig.3).

CONCLUSION

The atom migration in nano-container leads to QP formation with density N=1.6·10^{10}cm^{-2} and 50nm dimensions. The increase of thermoelectric efficiency (Z) up to 3,6.10^{-3}K^{-1} is possible because of decrease of heat conduction at phonon scattering on QP. For more strong revealing of these effects the geometric sizes of interlayer nano-structures should be <40nm. The self-organization processes take pkace in limited medium applicably to layered crystals Bi_2Te_3<Ni, Zn, Se> Sb_2Te_3<Se> . The interlayer surface diffusion and also the QP and QW formation is the determinative factor.

The spontaneous formation of ordered arrays of facets with QP is energetically profitable and taking into consideration the relaxation effect of surface eigen strengths the periodically faceted structures and quantum points in Bi_2Te_3 (Sb_2Te_3)<Ni, Se, Zn> are obtained.

_____

[1] *B. Poudel, Q. Hao, Y. Ma, Y. Lan,A. Minnich, B. Yu, X. Yan, D. Wang, A. Muto, D. Vashaee, X. Chen, J. Liu, M.S. Dresselhaus, G. Chen, Zh. Ren.* Science **320,**634 (2008).

[2] *L.P. Bulat, V.B. Osvensky, G.I. Pivovarov, A.A. Snarskii, E.V. Tatyanin, A.A.O. Tay.* Proc. VI/ Eur. Conf on Thermoelectrics/Paris (2008).P.I2 -1 .(in Russian)

[3] *L.P. Bulat, I.A. Drabkin, V.B. Osnovenskiy, Q.I. Pivovarov, A.A. Snarskiy, E.V. Tatyanin.* Dokl. XI Mejqos. Sem. "Termoelektriki i ix primeneniya". FTI im. A.F. Ioffe RAN, SPB.(2008) .S.39. (in Russian)

[4] *F.K. Aleskerov, S.Sh. Kaxramanov, E.M. Derun i dr.* Nekotorie osobennosti formirovaniya nanoobektov v mejsloevom prostranstvo kristallov tipa Bi_2 Te_3// Fizika, Azerbaycan. 2007/ TXIII. №4.S.41. (in Russian)

[5] *B.M. Qolchman, V.A. Kutasov, L.N. Lukyanova.* // Fizika tverdoqo tela, 2009, tom 51, vip.4,s. 706 - 708. (in Russian)

[6] *S.B. Eremeev, Yu.M. Koroteev, E.V. Chulkov* // Pisma v JETF, t.91, v.8, s.419-423. (in Russian)

[7] *L.P. Bulat, D.A. Psheniy*–Severin Vliyanie tunnelirovaniya na termoelektricheskuyu effektivnost obemnix nanostrukturirovannix materialov, // Fizika tverdoqo tela, 2010, tom 52, vip.3, s.452-458. (in Russian)

EVOLUTION OF THE MEDIUM RANGE ORDER IN TERNARY CHALCOGENIDE GLASSES REVEALED FROM XRD MEASUREMENTS

E. MAMMADOV

Institute of Physics, National Academy of Sciences,
33 H. Javid Ave., Baku, AZ 1143, Azerbaijan

XRD powder patterns of $Ge_xAs_ySe_{1-x-y}$ glasses are studied in view of first sharp diffraction peak (FSDP). The composition with the lowest average coordination number exhibits two broad peak pattern resembling that for amorphous selenium. With increasing number of Ge and As atoms the FSDP intensity increases and shifts to low angles. This behavior is interpreted in view of medium-range ordering as two- and three-dimensional structural units are formed. It is suggested that one of the two structural configurations breaks down when composition goes through the chemical threshold.

INTRODUCTION

Local structural order in ternary chalcogenide glasses is of current interest due to their practical usefulness in various important technological applications. A complete understanding of atomic arrangement in these materials is necessary since their electronic properties are strongly correlated to the local structure. Short range order in binary glasses often preserves the same structural units as a main building blocks as in crystalline counterparts. Thus in As_xSe_{1-x} and Ge_xSe_{1-x} glasses arsenic and germanium atoms form pyramidal and tetrahedral structures forming two and three-dimensional networks, respectively. These units are interconnected through selenium chains in compositions up to the stoichiometry when pyramids are stacked in layers and corner and edge-sharing tetrahedra form 3D structure, where As-Se and Ge-Se are primary bonds. In contrast to crystals, however, these structural units are randomly distributed over the network giving rise to distributions in bond angles and bond lengths. In ternary $Ge_xAs_ySe_{1-x-y}$ glasses this is rather complicated as compositional disorder is added into the structural disorder.

It is known that the structural order in amorphous solids may extend to second or third nearest neighbor that is a medium-range order. Investigation of their structural properties is hampered due to absence of long-range order when often no meaningful information can be obtained from experiments. X-ray diffraction patterns of binary and ternary chalcogenide glasses often exhibit broad multi-peak line shapes. The first sharp diffraction peak (FSDP) on the XRD patterns has been proved useful to study the medium-range ordering in these glasses [1-3]. The FSDP – related parameters such as the position, broadening, and intensity of the peak as well as estimation of quasi-periodicity of the local structure, d and its extension over linear dimension, L have been used to describe the medium-range structural correlations in these materials.

In this work we report on FSDP treatment of XRD powder patterns of $Ge_xAs_ySe_{1-x-y}$ glasses.

EXPERIMENTAL

The measurements have been performed on powdered samples of bulk glasses obtained by standard melt-quenching technique. These covalently bonded glasses often exhibit unique properties dependent not on chemical composition but average coordination number.

Compositions have been chosen differing by average coordination number with nearly similar concentrations of Ge and As atoms. Glass with the highest average coordination number and with composition corresponding to commercially available amorphous material transmitting infrared radiation (AMTIR-1), $Ge_{0.33}As_{0.12}Se_{0.55}$ has also been synthesized.

XRD powder patterns were obtained using Cu K_α – radiation ($\lambda = 1.5418$ Å) in the range of diffraction angles $10 \leq 2\theta \leq 90°$ with 0.05° step.

RESULTS

XRD powder patterns for compositions studied are shown in Fig.1. The pattern for composition with the lowest average coordination number exhibits two broad bands similar to those observed for a-Se [4]. As concentration of Ge and As increases FSDP of the XRD patterns shows up. The intensity of the FSDP gradually increases with increasing average coordination number of the glasses. The FSDP part of the diffraction patterns are also shown at an extended scale. The full width at half maximum (FWHM) decreases for $Ge_2As_2Se_7$ and increases with further increasing average coordination number.

DISCUSSION

The appearance of FSDP is often related to medium range ordering in amorphous solids. There are several models exploiting for explanation the FSDP. In a model proposed by Elliot [5, 6] the FSDP has been suggested as related to void distribution between structural units. The model has provided good results for binary glasses such as $GeSe_2$. In view of this model it is clear that one-dimensional chains in a-Se would not produce FSDP peak. Indeed XRD pattern of a-Se consists of two main peaks [4]. As Ge and As atoms are introduced, three-dimensional tetrahedral $GeSe_{4/2}$ and two-dimensional pyramidal $AsSe_{3/2}$ structural units are formed contributing to the appearance of the FSDP. The more units are formed the more probability for the medium-range ordering in the glassy matrix. This is clearly manifested in the increased FSDP intensity for $Ge_{0.15}As_{0.10}Se_{0.75}$ and $Ge_2As_2Se_7$ glasses. The sharpening of the FSDP is also indicative of higher degree of medium-range ordering in $Ge_2As_2Se_7$

comparing with $Ge_{0.15}As_{0.10}Se_{0.75}$. Although in the diffraction pattern of $Ge_{0.05}As_{0.10}Se_{0.85}$ glass a shoulder at the low angle side of the first main peak is observed its deconvolution is difficult. However, it is clear that the appearance of the FSDP is related to the formation of Ge-tetrahedra and As-pyramids. These structural units are randomly and homogeneously distributed over the glass network [7], being correlated at distances L found from the Scherrer's formula as $L = 0.9\lambda/\beta(2\theta_{FSDP})\cos(\theta_{FSDP})$. The correlation length L increases for $Ge_2As_2Se_7$ and decreases for $Ge_2As_2Se_5$ and $Ge_{0.33}As_{0.12}Se_{0.55}$. As the amount of tetrahedra and pyramids increases when going to $Ge_2As_2Se_7$ FSDP intensity also increases and the peak shifts to lower angles. According to Elliot's model however, as the cation-cation distance decreases and correspondingly the void volume around the molecules also decreases, the FSDP peak position should shift to higher angles. This was demonstrated to work well for stoichiometric binary glasses. However, for the ternary nonstoichiometric glasses one should consider correlations between different structural units contributing to the diffraction pattern. Although the mechanisms of the low angle shift are not clear similar behavior was observed in binary nonstoichiometric glasses as well [8]. Further, $Ge_2As_2Se_7$ is a stoichiometric pseudobinary composition for which only Ge-Se and As-Se bonds are expected and the whole glass network is constructed with tetrahedra and pyramids as the main building blocks. [75]As nuclear quadrupole resonance (NQR) and nuclear magnetic resonance (NMR) experiments showed no evidence of As-As homopolar bonds in this composition. [7, 9].

The FSDP intensity increases and becomes narrower for $Ge_2As_2Se_5$ and $Ge_{0.33}As_{0.12}Se_{0.55}$ glasses. Using the correlation length L and the relation for periodicity in distribution of structural units $d = \lambda/2\sin(\theta_{FSDP})$ we estimate the packing factor in the glasses as L/d [2]. As seen from Figure 2, the calculated packing factor and macroscopic density increase up to $Ge_2As_2Se_7$ as the structural units in the glass network become more crosslinked and the entire structure more closely packed. Both quantities decrease for the $Ge_2As_2Se_5$ though the average coordination number increases.

This indicates that at least one of the two main structural units responsible for the FSDP in substoichiometric compositions is no more dominant. As the density of the material decreases the amount of voids around remaining FSDP-producing structural units increases, leading to the increased intensity of the first sharp diffraction peak.

Magnetic resonance measurements have shown that clusterization effects increase in this composition. Arsenic atoms form more complex structural units with large amount of As-As homopolar bonds rather than regular pyramids. The As bonding structure becomes even more complicated in $Ge_{33}As_{12}Se_{55}$ leading to nanoscale phase separation.

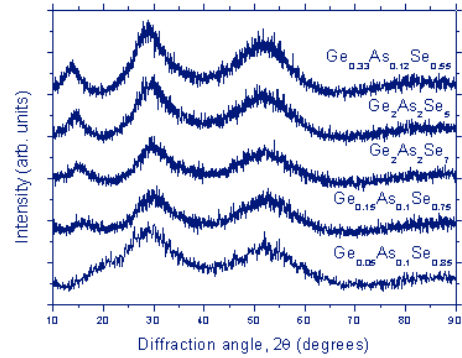*Fig. 1*. XRD powder patterns of $Ge_xAs_ySe_{1-x-y}$ glasses.

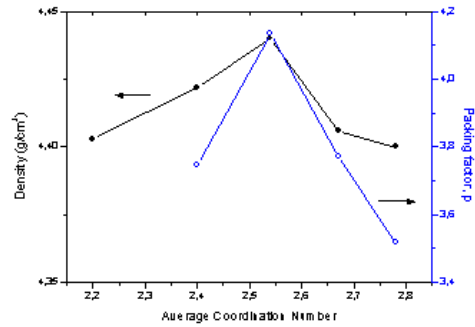*Fig 2*. FSDP-calculated packing factor and macroscopic density of $Ge_xAs_ySe_{1-x-y}$ glasses as a function of average coordination number.

SUMMARY

We have studied the XRD powder patterns of the $Ge_xAs_ySe_{1-x-y}$ glasses including stoichiometric and non-stoichiometric compositions. FSDP-related analysis based on cation-void distance mode, have revealed that medium-range correlations between the tetrahedral and pyramidal structural units formed by Ge and As atoms are responsible for the appearance of the FSDP. In the Se-deficient glasses it is more likely that As atoms change their bonding configuration forming more complex structural units rater than regular pyramids.

[1] *P.H. Gaskell*: J. Non-Cryst. Solids **351** (2005) 1003-1013
[2] *T.S. Kavetskyy, O.I. Shpotyuk, V.T. Boyko*: J. Phys. Chem. Solids **68** (2007) 712-715
[3] *O. P. Rachek*: J. Non-Cryst. Solids **352** (2006) 3781-3786
[4] *F. Ye and K. Lu:* Acta mater. **46**(1998),5965- 5971
[5] *S. R. Elliot:* Phys. Rev. Lett. **67** (1991) 711-714

[6] *S. R. Elliot:* J. Non-Cryst. Solids **182** (1995) 40-48
[7] *E. Mammadov and P. C. Taylor*: J. Non-Cryst. Solids **354** (2008) 2732
[8] *J. De Neufville, S. Moss, S. Ovshinsky:* J. Non-Cryst. Solids **13** (1974) 191-223
[9] *E. Mammadov, P. C. Taylor, D. Baker, D. Bobela, A. Reyes, P. Kuhns, and S. Mehdiyeva*: Mater. Res. Soc. Symp. Proc. **1160** (2009) 171-176.

PREPARATION, SOME PROPERTIES OF PORPHYRIN NANOTUBES, AND 2D STRUCTURAL MODELING OF HYBRID PORPHYRIN MONOLAYERS

S.H. ABDULLAYEVA , N.S. SAFAROV

Institute of Physics, Azerbaijan National Academy of Sciences
Javid prospekt, 33, AZ1148, Baku, Azerbaijan
* email: niyaz_safar @ physics.ab.az;
phone: (+99450)620 12 86 (mobile); fax : (+99412) 510 08 27

Porphyrin nanotubes have been obtained from tetrakis (4-sulfonatophenil) porphyrin (TTPS4) using ionic self-assembly, and UV-vis spectra have been recorded. pH titration of the Soret band has been performed at 420 nm. It has been shown that by decreasing pH from pH 7.7 to pH 1.0 the changes in UV-vis spectra characteristic for porphyrin aggregation (batochromic shift) take place. At pH 7.7 in TPPS4 spectra the peaks at 420 (Soret band) and at 555, 596 nm (Q bands) are observed. At pH 1.0 the peak of the Soret band shifts to 434, whereas Q bands shift to 589 and 644 nm, respectively. It has been found that Autodock Vina program allows creating realistic 2D structural models of porphyrin monolayers adsorbed on a graphene substrate. After the first layer is completely formed owing to π-π interactions and van der Waals forces between porphyrin and graphene the second and consequent layers begin to form due to porphyrin J- and H-aggregations.

INTRODUCTION

In recent years natural and synthetic macrocyclic compounds, porphyrins, and their analogues, and derivatives have attracted attention of researchers as a good alternative to carbon nanomaterials, carbon nanotubes and fullerenes. Due to unique properties including the ability to self-assembly, catalytic, antitumor, antiviral, optical and semiconductor properties porphyrins are increasingly used in chemistry, biology, medicine, optics and material science. On the basis of porphyrins new catalysts, sensors, drugs, artificial "blood", organic semiconductors, liquid crystals, organic photovoltaic cells for the accumulation of solar energy, materials for nonlinear optics have already been created. Very promising seems the use of porphyrins for "solar" hydrogen production, in molecular electronics, and as tools for targeted drug delivery.

Porphyrin is a macrocyclic bioorganic compound performing in living organisms a vital role in plant photosynthesis (chlorophyll), and the oxygen carrier in animals (hemoglobin), and as a part of vitamin B-12. In addition, porphyrins are essential part of the electron carrier proteins involved in the cell electron transport chain in animals and plants. Without this circuit it would be impossible to implement any respiratory function of living cells.

The ancestor of all porphyrin molecules is porphin (Fig.1). Many unique properties of porphyrins can be explained by the presence of large number of unpaired delocalized electrons (18 of 22 π-electrons are delocalized). Vast variety of porphyrins is achieved not only by substitution of different functional groups in different positions, but also by the presence of complexing metal atom in the center of the molecule. The dimensions of the macrocycle are such that, ions of almost all metals, especially transition metals, may be introduced into the center of the molecule forming metalloporphyrins. For example, the green pigment chlorophyll contains magnesium, vitamin B-12 contains cobalt and

heme, the component of hemoglobin, contains the iron ion.

For nanotechnology the most interesting feature of some porphyrins is their ability to self-assemble into various (depending on conditions) nanostructures such as rods, strips, tubes, layers, rings, etc. Excellent capability for self-assembly have a pairs of cationic and anionic porphyrins. Among these the most actively studied are listed in fig.2: meso-tetrakis (4-sulfonatophenyl) porphine (TTPS4) and meso - tetra (4-N-methyl-pyridyl) porphyrin (TMPyP). By ionic self-assembly in appropriate circumstances TPPS4 and TMPyP organize into the nanotube [1], the diameter and length of which depends on conditions used for a preparation. The inner diameter of porphyrin nanotubes ranges 1 - 50 nm [1, 2].
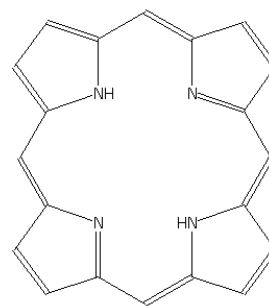

Fig.1. Porphin, the ancestor of all natural and synthetic porphyrins and phthalocyanines

In strongly acidic medium porphyrin nanotubes can also be prepared from one type of porphyrin. At pH 4 TPPS4 turns partially into diacid form due to protonation of two nitrogen atoms in the center of the molecule so that the following equilibrium exists in the media:

$$H2TPPS4^{4-} + 2H^+ \leftrightarrow H4TPPS4^{2-}$$

The diacid form of TPPS4 is capable to self-assembly into J-aggregates (edge-to-edge aggregation) and H-aggregates (face-to-face aggregation) [3]. At lower pH (pH 1-2) two additional protons are connected to the two negatively charged SO3-groups, hiding their negative charges. Thus, the TPPS4 molecule becomes zwitterion, and due to the spatial separation of positive and negative groups acquires a dipole moment. It is assumed that the

formation of these dipoles leads to the association of molecules into tubular or other type of nanostructure [3].

Unfortunately, the two powerful structure resolving methods, NMR and X-ray analysis, cannot be applied to determine the detailed and accurate spatial structure of the porphyrin nanotube due to the heterogeneity of so far obtained material. Therefore, several authors tried, to create a spatial model of porphyrin nanostructures on the basis of circumstantial evidence [3, 4].
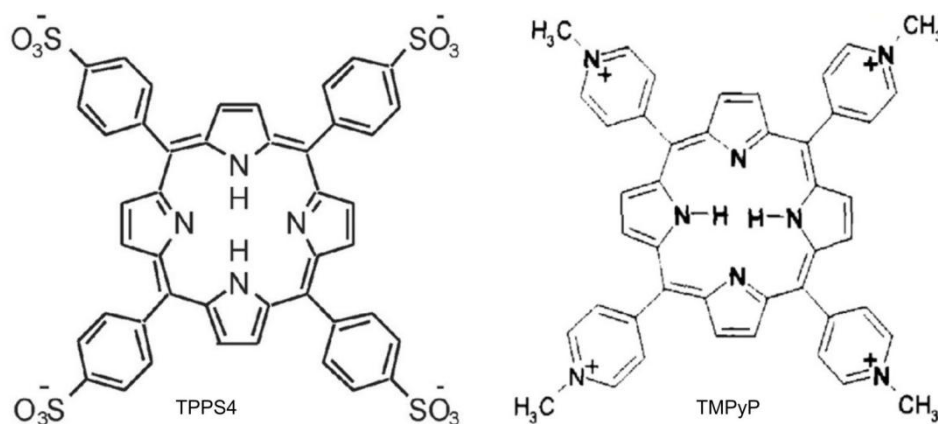
Fig. 2. Structural formulae of the porphyrins studied.

In this regard, the use of molecular modeling techniques can be justified and eventually will lead to understanding the mechanisms of self-assembly of porphyrin nanostructures [5]. In the present work we performed synthesis of TPPS4 nanotubes, investigated their spectroscopic and ionic properties, and then we had tried to create a simplified model of porphyrin layers onto graphene sheets aiming to prepare the basis for porphyrin nanotube model in the future. The results of the work will help to identify new research directions of porphyrin nanotubes and nanolayers and eventually find out their true spatial structure.

MATERIALS AND METHODS

The synthesis of porphyrins.

All reagents were of analytical grade from Merck (Germany) and were used without further purification except pyrrole, which was distilled just before the synthesis. Deionized water was of MilliQ grade (resistivity higher than 18 MΩ /cm). Synthesis of meso-tetraphenylporphyrin (TPP) was carried out essentially by a method of Adler et al. [6] with minor modifications consist in using activated carbon instead of fuller's clay for final TPP purification step. Activated carbon treatment of the TPP solution was performed by vigorous shaking of 1g of TPP and 100g of carbon in 1 L of 1,1,1-trichloroethane, and then filtered twice through a small (2.5 x 6 cm) glass column of activated carbon. After drying in a vacuum desiccator over calcium chloride, a blue-violet, crystalline powder of TPP was obtained and used for TPPS4 preparation.

Synthesis TPPS4 performed as follows. 20g of TPP was suspended in 500ml of concentrated sulfuric acid and

heated on a water bath at 90° C for 6 hours, then allowed to cool overnight. The next morning the resulting viscous mass was stirred gently, added to 1500 ml of water and allowed to cool to room temperature. The resulting porphyrin (green) was collected by filtering through sintered-glass funnel and washed with a small (400-500 ml) of acetone. Further, porphyrin and activated charcoal suspended in water (1500 ml) and neutralized with saturated sodium bicarbonate solution until turning the solution color from green to purple. The mixture was again filtered to remove coal, and unreacted TPP. The filtrate was dialyzed four times against 40 volumes of deionized water (3 hours for each dialysis procedure) using a Visking dialysis membrane. Then the dialysate was filtered through a paper filter and the filtrate was evaporated almost to dryness. Remaining water was removed by drying in a vacuum desiccator over potassium hydroxide.

TPPS4 was recrystallized from methanol-ethanol and dried at 100° C. The anhydrous product was obtained in a vacuum oven at 150° C during a day.

0.018 mM aqueous stock solution of TPPS4 was used for all subsequent experiments.

Spectroscopy.

The concentrations of the TPPS4 solutions were estimated using a molar extinction coefficient of 18,900 M^{-1} cm^{-1} at 515 nm [7].

The spectra of porphyrins and nanotubes were analyzed on a GENESIS 10s (Thermo Electron Corporation) spectrophotometer in quartz cuvettes with optical path length of 1 cm and deionized water was used as a blank sample. Processing of the results produced by

the blend with a spectrophotometer and computer program Vision Lite.

pH-measurements.

pH measurements and titration of porphyrin nanotubes were carried out using a HI208 Hanna Instruments) pH-meter. The titration was performed as follows. pH of the initial solution of TPPS4 in water adjusted to a 7.7 by adding 0.1 M KOH solution and a sample was taken for spectrophotometry. The pH was stepwise decreased by 0.5 units up to pH 1.0 by adding small amounts of concentrated HCl, each time selecting a sample for spectrophotometry. Samples with different pH values were kept overnight at 4°C in the dark, and the spectra were recorded on the following day. Titration data were plotted and analyzed using SigmaPlot (Jandel Corporation) program.

A function

$$f(y,x)= (a*k+b*x)/(k+x),$$

where 'a' and 'b' are adjustable parameters, k-dissociation constant, x – independent variable (concentration of protons), and y –dependent variable (absorbance) was used to build the best nonlinear curve fit and calculate pK_a.

Computational details.

All calculations were performed in double on Intel Core2 Duo CPU 2.60 GHz running Microsoft Windows XP Professional, version 2002, service pack 3 OS and Intel *(R)* Pentium *(R)* 4 CPU 2.66 GHz Sony Vaio laptop with the same Windows OS installed. In both cases the results were essentially identical. 3-D molecular structures of porphyrins in .pdb (protein data bank) format were generated using Hyperchem version 8.0.6 for Windows. The geometry of a molecule was optimized using density functional theory (DFT) employing Becke 88 exchange potential in combination with LYP (Lee, Yang, and Parr) correlation functional. *Ab initio* calculations were performed with core Hamiltonian option for molecular orbitals initial guess. Quantum Wise Atomistix Toolkit demo version.12.12.0 was used to optimize geometry of the input molecules. Ideal graphene rectangle sheet (117.3 x 71.9 Angstrom) .pdb file was exported from Nanotube Modeller, v.1.6.4 (JCrystalSoft). The height of the grid parallelepiped box (searching area) was 16 Angstrom.

Autodock Vina program [8] was used to dock a porphyrin molecule to the ideal graphene sheet. A greed box of dimensions 68 x 114 x 35 Angstrom with the center of the box placed at the center of the graphene sheet was applied. An exhaustiveness parameter was set to default (9). Resulting 9 porphyrin molecule outputs were analyzed and the position of porphyrin molecule having minimum energy was selected for the next simulation step.

A variety of programs such as Ascalaph Graphics modeling suite (Copyright (C) 2006-2009 Agile Molecule), PyMol (Open-Source 0.99rc6 executable build), RasTop v.2.2 (Copyright © Philippe Valadon 2000-2004) and other were used for viewing molecules and nanostructures.

RESULTS AND DISCUSSION

Ionic properties

The data on the basicity of the pyrrole nitrogen atoms at the center of the porphyrin molecule is important for assessing the degree of ionization in solutions of varying ionic strength. Pyrrole is a very weak base with a dissociation constant (pK_a) of about 4. Reported pKa values of the nitrogen atoms of a pyrrole ring of porphyrin derivatives vary in the range pK=2.9 -5.1 [8]. According to our calculations of the best curve fit (fig. 3b) gives pK_a = 4.23, which is close to the value reported by majority of other researchers (4.5) [3].
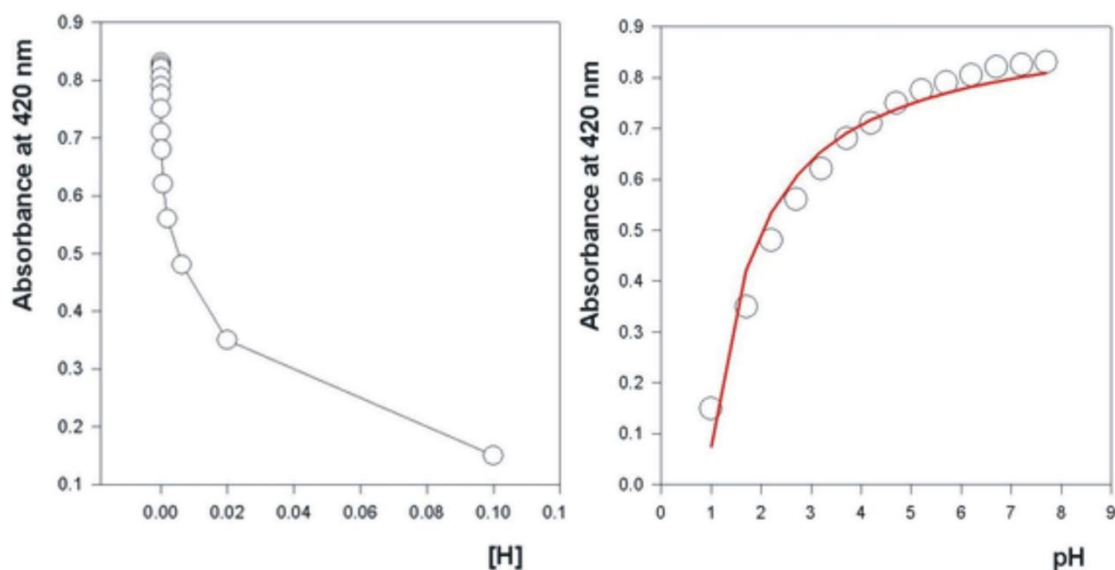

Fig. 3. The dependence of the optical density of TPPS4 on the pH at 420 nm.
a – [H] dependence in semilogarithmic coordinates; b – pH dependence, the red line indicates the best curve fit

The results of pH - titration of the Soret band at 420 nm are presented in fig3. We observed that the original purple color of porphyrin at pH 4 disappears and at a pH near 1-2 it becomes greenish. Such a change in color is explained by the aggregation of porphyrin molecules.

SPECTROSCOPY

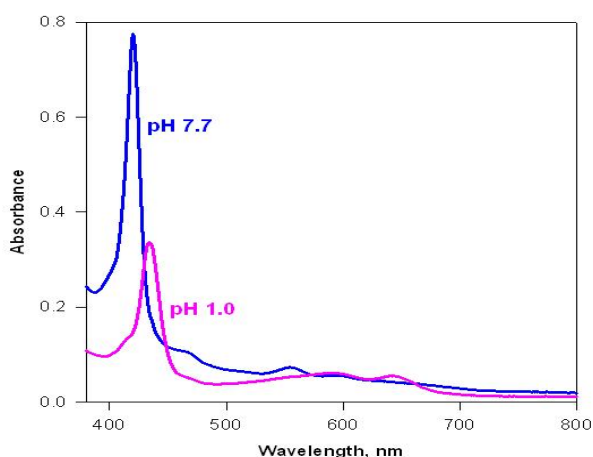Fig. 4 and fig. 5 show the spectra of TPPS4 at pH 7.7 and pH 1.0.

Fig. 4. UV-vis spectra of TPPS4 at two different pH values.

From the figures 4 and 5 it can be seen that at pH 7.7 TPPS4 has a maximum value of absorbance at 420 nm. This is so-called Soret band, characteristic of all porphyrins. Two minor peaks at longer wavelengths denoted as Q - lines have maxima at 555 and 595 nm. At pH 1.0 the following changes in the spectrum are evident. Maximum of the Soret band shifts to 434 nm and the Q-lines are shifted to longer wavelengths also and have maxima at 589 and 644 nm. The described changes in the spectra at different pH are characteristic for the formation of J-and H-aggregates, in particular nanotubules, from the monomeric porphyrins [3, 4]
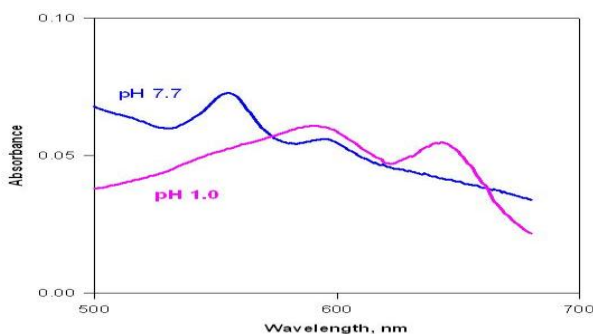
Fig. 5. UV-vis spectra of TPPS4 at two different pH values in the Q bands area.

Molecular Modeling

Emerging nanotechnology revolution demands new adequate methods to look inside intrinsic structure and properties of new nanoscale objects. Unfortunately, existing powerful methods of modern science are nor very

suitable for nanoscale objects, especially for bionanostructures [9]. In such a situation molecular mechanics (force field), molecular dynamics, and generally molecular modeling becomes popular to study molecular structures on a nanoscale level [10]. It is known that porphyrins bind to carbon nanostructures (graphene, carbon nanotubes, and fullerenes) by noncovalent interactions, see [11] for a review. To the best of our knowledge we are the first to adapt Autodock Vina [8] program for porphyrin – carbon hybrid nanostructure models constructing. Such programs are usually employed for molecular docking, finding the optimal spatial arrangement of the ligand (usually a low molecular therapeutic agent) in a protein receptor moiety and are widely used in pharmaceutical science for new drugs screening. Autodock Vina uses molecular structure files in .pdb format as input, and then by adding charge information to the residues it converts these files into .pdbqt format. Then the Vina module of the program docks a smaller molecule, 'ligand', to a big one, 'receptor', by finding the position and conformation which has the minimum binding energy. The resulting output 'ligand' file in .pdb format can be viewed together with 'receptor'. At this stage a researcher makes conclusions regarding binding a set of ligands to the macromolecule, choose the best ligand and its conformation, makes decision to continue with searching the better ligand, or select the best ligand from the set to perform additional *in vivo* or *in vitro* studies. Usually the computer simulations finish at this stage and a researcher presents obtained results for the next research or for a publication. In our simulations we docked porphyrin molecule, which served as a 'ligand' to the ideal graphene sheet, which served as a 'receptor'. To make a model of porphyrin monolayers, containing not a single but a large number of porphyrin molecules we have applied the following approach. When the first porphyrin molecule is successfully docked to a graphene sheet of certain size we continue simulations by adding second, third, fourth etc porphyrin molecules to the structure obtained at a previous step. To make the multistep studies possible the .pdb file containing structure information of graphene sheet and the file carrying bound porphyrin spatial information were combined in a single .pdb file using Ascalaph Graphics program's 'add' function. The combined hybrid molecular structure served as a 'receptor' for binding the next porphyrin molecule. At each stage porphyrin output file was combined with previous (graphene + porphyrin) output file and served as input for the next cycle (stage).

In this paper we present a model of porphyrin monolayers onto graphene substrate obtained by above described approach. We started with the simpler model, namely TPP layers on graphene monolayers. TPP has four uncharged meso-substituted phenyl moieties, which are often referred to as 'legs'. Using porphyrin with uncharged 'legs' allowed us to exclude electrostatic interactions between charged legs in case of cationic or anionic porphyrins that otherwise could interfere with the analyzing of the results obtained, and would make perform additional time consuming simulations.

The results of the first (TPP-graphene model) is represented in figures 6 and 7. In fig. 6a and 6b highly ordered porphyrin monolayers are clearly evident.

It is well known that porphyrins, like many other dyes form two kinds of aggregates, J –aggregates and H-aggregates. Depending on the chemical structure and environmental conditions, different types of aggregates [12], laterally stacked (tilted) (J-aggregates) and axially stacked (H-aggregates) where observed. In our simulations we were not able to observe J – or H-aggregates until all the graphene sheet was filled with a porphyrin monolayer. After there was no space to dock the whole porphyrin molecule onto the graphene sheet flatly, the tilted (J-aggregated) molecules

were observed (green colored molecules on figure 6c). The second and subsequent layers were begun to form after about 30 cycles of docking (Fig. 6d). Among latter J- and H-aggregates were observed. Figure 6d shows the side view of 3 TPP layers on the graphene sheet. The absence of J- or H-aggregation within the first monolayer seemed quite strange for TPP in its ground state has dihedral angles between meso-substituted 'legs' and the porphyrin core are of about 55-65° [13]. Nevertheless, flattening of the 'legs' have been observed previously in case of molecular flattening of TMPyP on the surface of chemically converted graphene [4]. The authors made the conclusion that
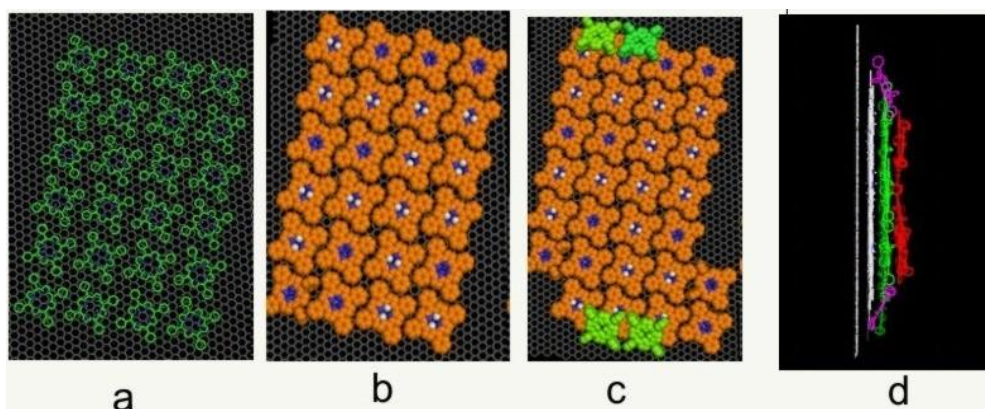
Fig. 6. Schematic representation of TPP arrangement on an ideal graphene sheet. a) – a fragment of TPP monolayer after 24 cycles of docking simulations; b) – space fill model of the above; c) – space fill model after 26 cycles of simulations, four tilted molecules are shown in green color; d) – side view of a stick model consisting of graphene sheet (grey), first porphyrin layer (white), second porphyrin layer (green), the beginning of third porphyrin layer formation (red). Intermediate, tilted, molecules are visible on the edges of the graphene sheet (magenta color).
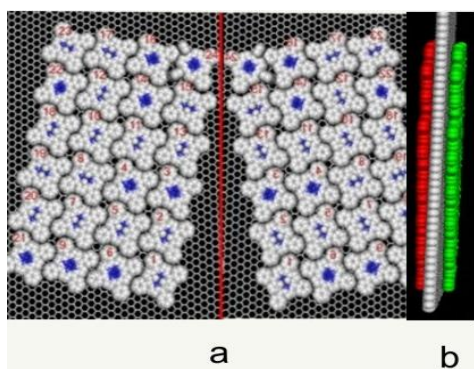

Fig. 7. a - a fragment of TPP double monolayers on a graphene sheet model showing their symmetry (a). b – side view of the graphene sheet sandwiched between two TPP monolayers. The numbering indicates the queue of porphyrin molecule binding. The red vertical line shows the mirror plane.

The model depicted on Figure 7 was obtained when we performed simulation of docking porphyrins simultaneously to the both side of graphene. In this experiment we used a graphene rectangle with he same dimensions as previously ((117.3 x 71.9 Angstrom) except that the height of the search area in Z-direction was enlarged to 24 Angstrom and the line dividing Z-dimension passed the grid parallelepiped just in two equal parts in order to make possible the both side of the graphene sheet accept a porphyrin molecule. During this experiment we have noticed that if there is a place to bind

each new porphyrin molecule does not bind randomly to the graphene, but binds just opposite the pervious on the other side of the graphene sheet. As a result, at each cycle we have a mirror symmetric picture of porphyrins bound to the opposite graphene sides. This is clearly visible from Figure 7a.

As it has already been mention before, TPP In its ground state has four phenyl rings each of which posse's dihedral angle (torsion). These four torsions are able to rotate out of the porphyrin plane by an angle of about 60° [13]. Remarkable feature of the Vina program is that its scoring function allows torsions rotate to adopt the most preferable conformation to fit the 'receptor binding site [8].

Fig. 8 illustrates the two conformation of TPP: a-dihedral angles before binding; 64.55°, 64.62°, 65.51°, and 65.89;

b- dihedral angles of TPP bound to graphene; 2.67°, 2.76°, 2.90°, and 2.71°.
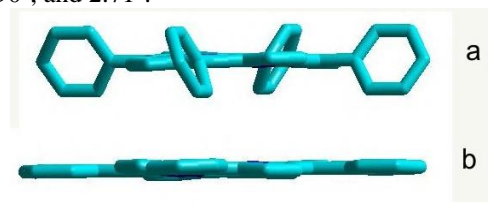

Fig. 8. Schematic representation of TPP. a) – a stick model of TPP molecule on its ground state; b) – a stick model of TPP molecule bound to the graphene sheet. Flattening of phenyl legs is clearly visible.

Table.

Statistics and binding energies of TPP to graphene, E (kcal/mol) ***

one side binding									
1st layer					2nd and other layers altogether				
Mean	SD	95% confidential interval	99% confidential interval	skewness	mean	SD	95% confidential interval	99% confidential interval	skewness
-30.64	3.21	1.20	1.20	1.61	-18.33	3.28	1.45	1.98	-1.44
two sides binding									
side a					Side b				
Mean	SD	95% confidential interval	99% confidential interval	skewness	mean	SD	95% confidential interval	99% confidential interval	skewness
31.99	1.87	0.88	1.20	2.48	32.64	2.27	1.09	1.49	3.05

** * It should be noted that binding energies are rather relative and depend on the scoring function of Vina-Autodock program, which optimization algorithm is stochastic [8].

The table represents some statistics and energies of TPP binding. It can bee seen from the table that in both cases the most affinity to graphene posses the first layer. The binding of the first layer in double – side - binding is even slightly greater. It was not possible discriminate the binding of the second and third layers in one-side-binding experiment. The binding in that case are rather random and statistically inauthentic.

CONCLUSIONS

In conclusion we would like to underscore some results obtained in the present paper.

1. Porphyrins are unique compounds with many remarkable features including, catalytic, antitumor, antiviral, and optical and semiconductor properties. The most intriguing property of porphyrins is their ability to self-assembly and their capability to form nanohybrids with a number of other nanomaterials: carbon nanotubes, graphene, fullerenes, nucleic acids, proteins, lipids, detergents and many others. Creating of monolayers of controlled shape and patterns may allow considerable impulse for the development bottom –up approach in nanotechnology.

2. We have prepared and studied some ionic and spectral characteristics of porphyrin nanotubes from TTPS4 and made a model of TPP monolayer onto ideal graphene sheet.

3. A docking program Autodock Vina has been used during modeling the monolayers. We have shown that a new porphyrin molecule binds to the already existing monolayer part not randomly, but preferably at the places where the previously docked molecules exist. This indicate that π-π interactions play main role in the binding

of a porphyrin molecule to graphene, but can be enhanced /modulated by van der Waals interactions between neighboring porphyrin molecules. Double sided binding of porphyrins to the both side of the graphene sheet also support this suggestion.

4. Our results are in very good agreement with work [14], in which authors using physical methods have shown the flattening of porphyrin molecules on a chemically modified graphene induced by π-π stacking cooperative interactions. Our simulations are also in a good consistency with the paper of W. Auwarter et al. [13] showed by scanning tunneling microscopy (STM) that porphyrins self-assemble into highly ordered domains. We also performed molecular modeling of TPP monolayers on Ag (111) and Au (111) and found that our data again do not differ significantly from the data obtained by physical methods (data re not shown).

5. As regards to sensing/biosensing properties of porphyrins, the part of our work suggests the possibility of binding two different enantiomers of chiral porphyrin on different graphene sides making sensitive sensors for discriminating two very similar molecules.

6. Consequently, we demonstrate inexpensive molecular modeling of hybrid porphyrin nanostructures, which are in a good agreement with most data available, allow predicting new material features and may serve as a useful approach for nanotechnology.

Acknowledgment

———————————————

[1] *Z. Wang, C.J.Medforth, J.A. Shellnutt.* J. Am. Chem. Soc, 126, pp. 15954-15955, 2004.

[2] *Takahiko Kojima, Ryosuke Harada, Tatsuaki Nakanishi, Kenji Kaneko, and Shunichi Fukuzumi*, Chem. Mater, 19 (1), pp. 51–58, 2006.

[3] *S.C.M. Gandini, E.L. Gelamo, R. Itri, and M. Tabak.* Biophys.J., vol.85. pp.1259-1268, 2003.

[4] *S.M.Vlaming, R.Fugilis, M.C.A. Stuart, J. Knoester, and P.H.M. van Loosdrecht.*, J.Phys.Chem.B vol.113, pp.2273-2283, 2009.

[5] *Deyu Lu et al.* Phys.Biol., Author Manuscript, vol.3, no.1 S40-S53, 2008.

[6] *A.D.Adler et al.*, J.Org.Chem., vol. 32 , no.2, pp.476-477, 1967.

[7] *G.H. Barnett, M.F. Hudson, and K.M.Smith.* J.Chem.Soc.Perkin Trans. I., 1401-1403, 1975.

[8] *O. Trott, A. J. Olson.* Journal of Comp. Chemistry, vol.31, pp. 455-461, 2010.

[9] *Deyu Lu, Alexey Aksimentiev, Army Y. Shih, Eduardo cruz-Chu, Peter L. Freddolino, Anton Arkhipov, and Klaus Schulten.* Phys. Biol.; vol. 3, 840, N 1, pp.540-543, 2008.

[10] *Helder M. Marques and Kenneth L. Brown.* Coord. Chem. Reviews. 225, pp.123-158, 2002.

[11] *David Britz and Andrei Khlobystov*.Chem. Soc. Rev., vol.35, pp 637—659, 2006.

[12] *Nakul C. Maiti, Shyamalava Mazumdar, and N. Periasamy.* J. Phys. Chem. B, 102 (9), pp 1528–1538, 1998.

[13] *W. Auwarter, A. eber-Bargioni, A. Riemann, and A. Schifrin*. J. Chem. Physics, 21; 124 (19), p. 194708, 2006.

[14] *Yuxu Xu, Lu Zhao, Hua Bai, Wenjing Hong, Chun Li, and Gaoquan Shi.* J.Am.Chem.Soc., vol.131, pp.13490-13497, 2009.

Received:19.04.12

CONTENTS